Gas bubble dynamics

Dominique Legendre

Institut de Mécanique des Fluides de Toulouse (IMFT)—Université de Toulouse, CNRS, INPT, UPS, 31400 Toulouse, France

Roberto Zenit

Center for Fluid Mechanics, School of Engineering, Brown University, Providence, Rhode Island 02912, USA

(published 17 April 2025)

The study of gas bubble dynamics in liquids is justified by the numerous applications and natural phenomena where this two-phase flow is encountered. Gas bubbles move as forces are applied to them; their dynamics are full of nuances that need to be addressed carefully. Since the mass of gas bubbles is practically negligible, in comparison to that of the surrounding liquid, their reaction to the fluid is controlled by the added mass acceleration and is thus impacted by all the forces arising from the fluid action. Furthermore, since their surface can be deformed by the same forces acting on them, their shape may change, leading to changes in their resistance to move and the drag force and therefore affecting their speed and their interaction with the surrounding flow, which is often turbulent. The liquid rheology, as well as its surfactant content, can also affect the bubble shape and motion. Understanding these issues, in addition to the effect of interactions with other bubbles, walls, and nonuniform flows, provides sufficient elements to model and predict bubble behavior through the solution of dynamic equations. In this review the key aspects of noncondensable gas bubble dynamics are covered. Classical references on the subject are surveyed, and an overview of the main findings in the past 20 years is provided. The review concludes with a scope and suggestions for future research directions, with special attention paid to the dynamics of bubbles in turbulence, in non-Newtonian fluid, and/or in the presence of electrolytes.

DOI: 10.1103/RevModPhys.97.025001

CONTENTS

I. Introduction 2
A. Motivation 2
B. Gas bubble dynamics 3
C. Previous reviews on the subject 4
II. What are Bubbles and How Are They Generated? 4
A. Conditions at a bubble surface 4
1. Mass conservation 5
2. Momentum conservation 5
B. Generation of bubbles 5
III. Rising Bubbles: Terminal Velocity, Deformation, and Interface Contamination 7
A. Dimensional analysis 8
B. Terminal velocity of a spherical bubble 9
1. Drag force 9
2. Terminal velocity 9
3. Scaling of the drag force at large Reynolds numbers 10
4. Drag and production of vorticity at the bubble surface 10
C. Bubble deformation and rupture 11
1. Ellipsoidal shape 12
2. Zigzagging bubbles 13
3. Spherical cap shape 14
4. Bubble rupture 15
D. Bubble surface contamination 16
IV. Bubble Interaction with Nonuniform and Unsteady Flows: Added Mass and the Lift Effect 18
A. The generalized Archimedes force and added mass effects 18
B. Shear-induced lift force 19
1. Lift effect at large Reynolds numbers: The tilting-stretching mechanism 21
2. Lift effect at small Reynolds numbers: The diffusing-matching mechanism 22
V. Bubble-Bubble and Bubble-Wall Interactions 22
A. Side-by-side interactions 22
B. In-line interactions 23
C. Bubble dynamics in contact with a wall 24
1. Criteria transition from sliding to bouncing regimes 24
2. Bubble deformation when sliding under a plane wall 25
3. Bubble bouncing under a horizontal wall 25
VI. Bubbles in Complex Fluids 26
A. An introduction to non-Newtonian liquids 26
1. Bubble shape for shear-dependent viscosity fluids 26
2. Bubble shape for viscoelastic fluids 27
B. Bubble velocity discontinuity and negative wake 28
C. Hydrodynamic interactions among bubbles in complex fluids 29
VII. Equation of Bubble Motion, Viscous Relaxation Time, Stokes Number, and History Force 30
A. Equation of bubble motion 30
B. Viscous relaxation time and Stokes number 31
C. History force 32

 © 2025 American Physical Society

VIII. Bubble Dynamics in Turbulence 32
A. Main mechanisms of interaction with turbulence 33
B. Small bubbles in turbulence 34
C. Large bubbles in turbulence 36
IX. Concluding Remarks on Open Questions 37
Acknowledgments 38
References 38

I. INTRODUCTION

The motion of bubbles in liquids is relevant in many natural, industrial, and everyday phenomena. Understanding how bubbles move is the key ingredient for developing new technologies, improving industrial processes, and coping with natural flow phenomena. We present a few examples of current importance to illustrate the need for this review.

A. Motivation

In this Introduction our aim is to delineate the subjects to be covered in this review. The examples illustrate what needs to be known if we want to study systems like these. We do not delve deeply into the details of these specific problems; we refer you to the cited publications in each case.

Prosperetti (2004) quoted a classical Greek proverb "*Homo bulla*," or "Man is a bubble," in reference to the frailty of human life. He then used this as a prompt to discuss bubble dynamics. The apparent infirmity of a bubble arises from its lack of mass. Despite this fact, the motion of a bubble carries a significant amount of inertia through its added mass, as discussed later in the review. Thus, even if bubbles are "fragile," they resist external flow effects thanks to the surface tension and are able to impose significant changes to the surrounding flow; therefore, their effect cannot be discarded or neglected. One example that displays this feature is the zigzagging motion of a rising bubble. It has been observed that when the size of an air bubble rising in a low-viscosity liquid surpasses a certain critical size, its shape is no longer spherical and its motion is no longer rectilinear. The first scientist to make this observation was Leonardo da Vinci (Roberts, 1981), as shown in Fig. 1(a). Prosperetti (2004) coined the term *Leonardo's paradox* to describe this unexpected behavior: the bubble moves sideways even though buoyancy points upward only. We discuss this in Sec. III.C.2.

Small bubbles have been used for a long time as tracers to visualize flows. An example of the streaklines in the near-wall region of a turbulent boundary layer is shown in Fig. 1(b), which is from Smith *et al.* (2012). This visualization technique, conceived in the 1950s (Clayton and Massey, 1967), uses the hydrogen bubbles produced at the cathode of a water electrolysis process. The production of hydrogen has become significant due to the need to replace fossil fuels. One of the methods to produce hydrogen on an industrial scale is electrolysis (Chandran, Bakshi, and Chatterjee, 2015), as shown in Fig. 1(c). The main obstacle in increasing production results from the need for a better understanding of the process of bubble formation and detachment (Angulo *et al.*, 2020).

Lohse (2018) provided a view of the importance of bubbles in modern technologies and natural phenomena extending from inkjet printing, ultrasound contrast agents, drag reduction, and surface cleaning to snapping shrimp and sonoluminescence. One of the subjects discussed by Lohse was bubble-induced drag reduction; see Fig. 1(d). Owing to its large economic implications and possible consequences for the naval shipping industry (Kawabuchi *et al.*, 2011), this subject is often cited to justify the study of bubble dynamics. Additionally, in nature some animals are believed to benefit from the same principle to reduce their drag during swimming. For example, Davenport *et al.* (2011) argued that penguins trap bubbles in their plumage to increase their speed when leaving the water, as illustrated in Fig. 1(e). The review of Ceccio (2010) provided a good starting point for understanding bubble drag reduction. Some researchers attribute the reduction of drag mainly to the presence of large bubbles (Murai, 2014; Verschoof *et al.*, 2016); however, small bubbles can also lead to a reduction in drag (Xu, Maxey, and Karniadakis, 2002; Pang and Zhang, 2018; Song *et al.*, 2018; García-Magariño *et al.*, 2023). Among the effects that have been identified as relevant for this problem are the interaction of bubbles with turbulence, bubble-bubble interactions, and bubble-wall interactions. Some of these issues are introduced in this review.

The dynamics at the bubble scale play an important role in chemical and biochemical reactors (Schlüter *et al.*, 2021). A widely referenced bubble-based engineering application is the so-called bubble column reactor (Kantarci, Borak, and Ulgen, 2005), which is shown in Fig. 1(f). These devices are used in the chemical, biochemical, and petroleum industries to provide high rates of mass and heat transfer while being compact and low maintenance. Such bubble reactors can be used to improve microalgae harvesting (Demir-Yilmaz *et al.*, 2023). These microorganisms can convert light energy into biomass using water and inorganic nutrients. However, using bubbles could also be inefficient since algae cells are in general hydrophilic, which results in poor bubble-cell interactions, thus requiring bubble functionalization. Flotation is a process that uses such bubble systems to collect solid particles in suspension using rising bubbles (Huang, Legendre, and Guiraud, 2011; Saththasivam, Loganathan, and Sarp, 2016; Federle *et al.*, 2024), in applications as varied as wastewater treatment, metallurgy, and bioreactors; see Fig. 1(g). In this case bubbles of a certain size ascend in a fluid at a certain terminal speed, interacting with other bubbles and containing walls. Another important aspect of bubbly columns is the large mixing rates that are induced by rising bubbles (Risso, 2018). As they move, agitation is induced and large-scale buoyancy-driven instabilities can appear. The properties of bubble-induced agitation are different from classical shear-induced turbulence. An understanding of mixing and large-scale motion can be achieved only if the local dynamics of individual bubbles and bubble-bubble interactions are known and understood. In many biological applications, small traces of bioproteins may cause a non-Newtonian behavior in the surrounding liquid. When the surrounding fluid is non-Newtonian, the nature of the bubbly flow changes drastically (Zenit and Feng, 2018), as shown in Fig. 1(h). Some of the issues that arise when one considers such fluids are discussed in Sec. VI.

Owing to the large gas-liquid surface area available in a bubbly liquid, these flows are often effective for mass transfer processes. Bubble columns are used to provide oxygen to cell

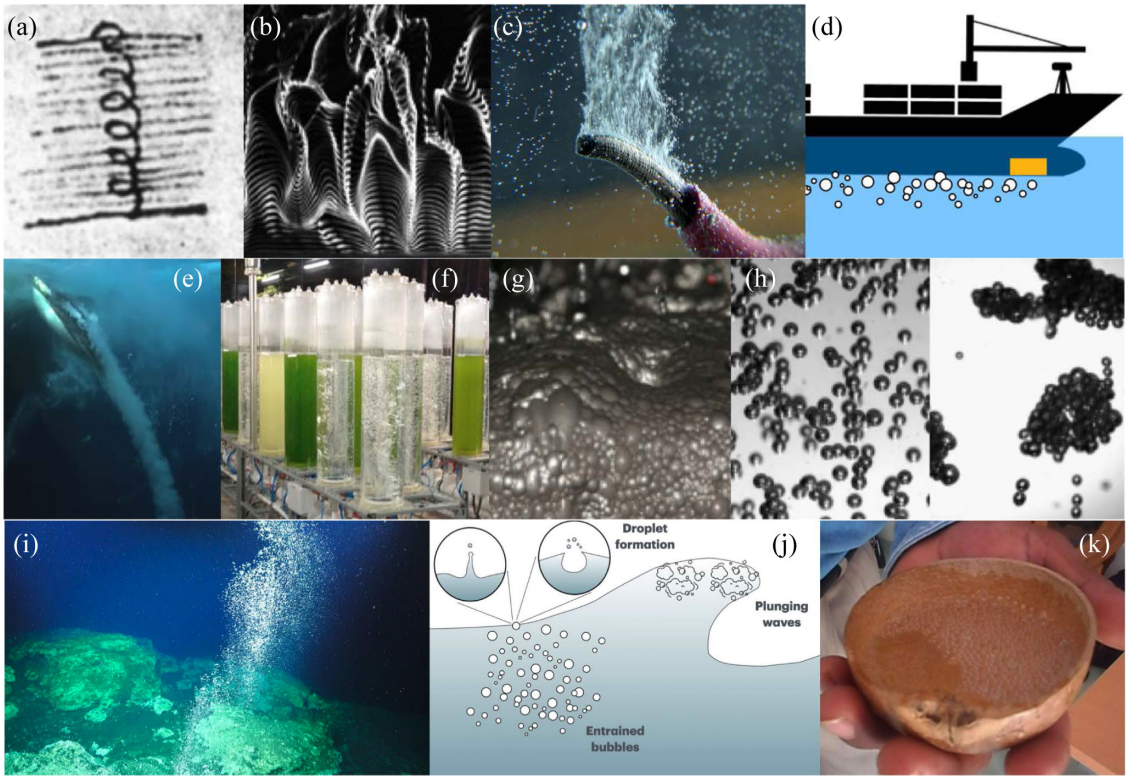

FIG. 1. (a) Zigzagging bubble drawing from Leonardo da Vinci (circa 1510). From Prosperetti, 2004. (b) Hydrogen bubble visualization of the streak pattern in the near-wall region of a turbulent boundary layer. From Smith *et al.*, 2012. (c) Hydrogen bubble plume formation from an electrode during water hydrolysis. From C. A. Heckler. (d) Bubble drag reduction for commercial ships. (e) Bubble drag reduction in swimming penguins. From Davenport *et al.*, 2011. (f) Bubble column bioreactors used to harvest algae. From Universidad EAFIT. (g) Surface of a flotation tank showing copper sulfide particles floated by bubbles. From Geomartin. (h) Comparison of a bubbly flow. Left image: Newtonian. Right image: non-Newtonian. Adapted from Vélez-Cordero and Zenit, 2011. (i) CO_2 bubbles in ocean seeps. From Schmidt Ocean Institute/ROV SuBastian. (j) Sea spray generation from bubbles bursting at the surface, which create films and jet drops. Adapted from Veron, 2015. (k) The alcohol content in mezcal is determined using traditional techniques, which involve the lifetime of surface bubbles. From Rage *et al.*, 2020.

cultures (Henzler and Kauling, 1993). In such cases oxygen bubbles injected at the bottom of a column would gradually diffuse into the liquid as they rise, thereby reducing their size. A similar process with environmental importance is the formation of CO_2 and methane bubbles released from the seabed to the surface (Leifer and Patro, 2002; Wang *et al.*, 2016), as seen in Fig. 1(i). The fraction of CH_4 that reaches the surface depends upon the release depth, the bubble size, the dissolved gas concentrations, the temperature, the surface-active substances, and the bulk fluid turbulence in the upwelling flow. Carbon dioxide sources also result in the acidification of the ocean waters, which in turn affects biodiversity (Teixidó *et al.*, 2018). A direct consequence of climate change is the development of lakes across the tundra in the Arctic. As the permafrost thaws, it releases carbon dioxide and methane gas, generating intense bubbly flows that rise to the surface (Lecher *et al.*, 2017).

When bubbles reach a free surface, they can briefly remain floating but eventually burst. The generation of ocean spray aerosols, which plays a crucial role in radiative and cloud processes, is the result of the bubble bursting process (Veron, 2015). When the bubble bursts, the jets and films shatter into fragments, creating small droplets. This process is depicted in Fig. 1(j). The time that a bubble remains at the surface depends on the properties of the fluid, as well as the level of surfactant content (Atasi *et al.*, 2020). Curiously, this process is used by traditional mezcal manufacturers in Mexico to determine the ethanol content of their distilled spirits (Rage *et al.*, 2020), as shown in Fig. 1(k).

In this review we provide a general description of bubble dynamics: how bubbles move in response to forces. The key issues discussed here are a direct consequence of the challenges posed by the aforementioned applications and natural phenomena. Among them are bubble terminal velocity, surface deformation, bubble interaction with flow, bubble-bubble and bubble-wall interactions, the effects of liquid rheology, and turbulence. Our review does not attempt to cover all possible aspects of bubble dynamics. The literature in the subject is vast and varied, making an exhaustive review impractical. Instead, we have selected the physical mechanisms that we consider the most relevant for entering the field of bubble dynamics. We end our review with a set of general equations of motion for bubbles and conclude with some general remarks and ideas for future directions.

B. Gas bubble dynamics

In this review we focus on the case of noncondensable gas bubbles, for which the size remains practically constant.

In some cases mass transfer occurs across the bubble surface but no phase change is considered. In this context we use the term *bubble dynamics* to refer to the motion of bubbles when they are subjected to external forces induced by the surrounding fluid. Note that this term is often used to study the process of bubble size evolution when bubbles are subjected to changes in pressure or temperature in the surrounding liquid (Brennen, 2014). This growth rate or collapse of bubbles is of particular importance for vapor bubbles (Prosperetti, 2017). We do not discuss those issues here.

For a bubble of mass $m_b = \rho_b \vartheta_b$ (ϑ_b and ρ_b are the bubble volume and gas density, respectively) moving at a velocity $\mathbf{u}_b$ in a fluid of density ρ and viscosity μ, as depicted in Fig. 2(a), a Lagrangian equation of motion can be written as

$$m_b \frac{d\mathbf{u}_b}{dt} = m_b \mathbf{g} + \int_S \mathbf{T} \cdot \mathbf{n}_b dS, \tag{1}$$

where $\mathbf{T}$ is the fluid stress tensor, S is the bubble surface, $\mathbf{n}_b$ is the normal vector on the bubble surface, and $\mathbf{g}$ is the gravitational acceleration. The bubble size is characterized by the bubble diameter $d_b = 2R$, where R is the bubble radius. The bubble dynamics are discussed in the laboratory frame of reference $\mathcal{R}$ or in the reference frame $\mathcal{R}_b$ moving with the bubble, as illustrated in Fig. 2. According to Eq. (1), if m_b is small, changes in the stress field around the bubble [the right-hand-side of Eq. (1)], would result in large values of $d\mathbf{u}_b/dt$. In other words, bubbles would respond drastically to small changes in the forces upon them. However, we emphasize that the amount of mass to be accelerated by the bubble is imposed by one of these forces, the added mass force contribution $-C_M m_f d\mathbf{u}_b/dt$, where C_M is the so-called added mass coefficient and $m_f = \rho \vartheta_b$ is the displaced mass of fluid caused by the presence of the bubble; see Sec. IV.A.

C. Previous reviews on the subject

There are numerous studies that address the dynamics of bubbles. The most cited source for the subject is the book by Clift, Grace, and Weber (1978), which has been reprinted numerous times. This book remains an invaluable source of information, particularly for experimental results conducted up to the end of the 1970s. Another important source of experimental data is the paper by Maxworthy *et al.* (1996), who conducted a vast set of experiments on rising bubbles in a wide range of parameters that remain relevant to many modern investigations. The review by Magnaudet and Eames (2000) is the most recent paper to cover some aspects of bubble dynamics, but it focuses mostly on spherical bubbles at large Reynolds numbers. However, that article is now more than 20 years old. Takagi and Matsumoto (2011) wrote a comprehensive review on the effect of surfactants on single bubble motion and bubbly flows. Zenit and Rodríguez-Rodríguez (2018) discussed different issues regarding bubbly drinks, with an emphasis on carbon dioxide bubbles exsolving from supersaturated liquids.

The objective of this review is to summarize recent findings on the dynamics of gas bubbles. We pay special attention to the presentation of results and to the description of the physical mechanisms involved, thereby making the review accessible to students and junior scientists.

II. WHAT ARE BUBBLES AND HOW ARE THEY GENERATED?

In this review we define a bubble as a discrete gas volume of density ρ_b and viscosity μ_b surrounded by a liquid with density ρ and viscosity μ. Since the gas and liquid are immiscible, the strength of the interface tension is characterized by a surface tension σ; see Fig. 2. Although the gas could be the vapor of the surrounding fluid, for which mass transfer across the interface could occur, we consider here only the case in which the gas is noncondensable in the liquid. Note that in some cases mass transfer may occur if the bubble gas dissolves into the surrounding liquid or if gas is already dissolved in the liquid.

A. Conditions at a bubble surface

We first turn our attention to the conditions at the bubble surface. The surface plays a significant role in the dynamics

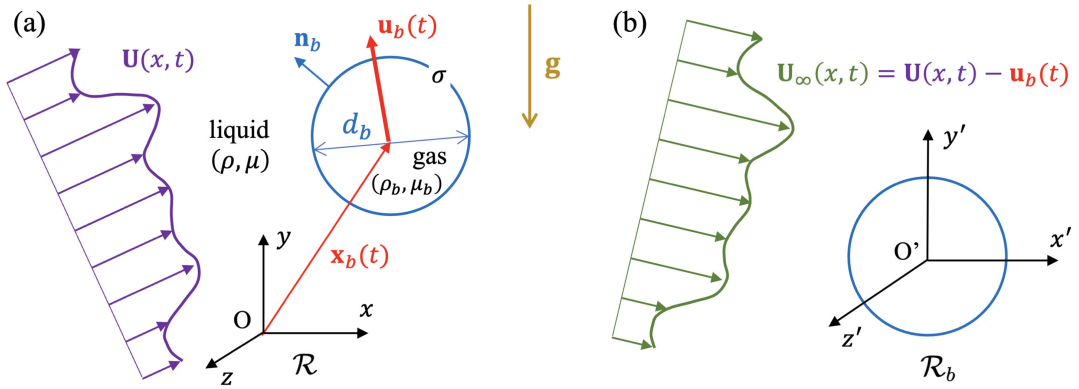

FIG. 2. Bubble dynamics: problem statement and frames of reference. (a) A bubble shown in the laboratory frame of reference $\mathcal{R}$. A bubble of diameter $d_b = 2R$, density ρ_b, and viscosity μ_b moves at a velocity $\mathbf{u}_b$ in a liquid of density ρ, viscosity μ, surface tension σ, and velocity field $\mathbf{U}$ that is in general nonuniform and unsteady. The gravitational field is represented by $\mathbf{g}$. (b) The same problem viewed in the reference frame $\mathcal{R}_b$ of the moving bubble. The velocity field here is $\mathbf{U}_\infty = \mathbf{U} - \mathbf{u}_b$.

because it acts as the boundary between the bubble and the fluid motion around it. Conservation of mass and momentum across the surface are used to identify the sets of conditions that must be considered at the surface.

1. Mass conservation

A balance of mass across the interface can be written as

$$\rho_b(\mathbf{u}_g - \mathbf{v}) \cdot \mathbf{n}_b = \rho(\mathbf{u} - \mathbf{v}) \cdot \mathbf{n}_b, \tag{2}$$

where $\mathbf{v}$ is the velocity of the interface, $\mathbf{u}_g$ is the gas velocity inside the bubble, $\mathbf{u}$ is the liquid velocity outside the bubble, and $\mathbf{n}_b$ is the normal vector pointing outward on the bubble surface. This general relation is derived by assuming that the interface has no mass and that there may be a phase change process (for example, boiling or condensation) or transfer of dissolved gases at the bubble surface. Following some manipulation, Eq. (2) can be rewritten as

$$\mathbf{u} \cdot \mathbf{n}_b = \frac{\rho_b}{\rho}\mathbf{u}_g \cdot \mathbf{n}_b + \left(1 - \frac{\rho_b}{\rho}\right)\mathbf{v} \cdot \mathbf{n}_b. \tag{3}$$

Equation (3) illustrates that a discontinuity (or jump) exists in the normal velocity across the bubble interface.

In the absence of mass transfer, $\rho_b(\mathbf{u}_g - \mathbf{v}) \cdot \mathbf{n}_b = \rho(\mathbf{u} - \mathbf{v}) \cdot \mathbf{n}_b = 0$, or when $\rho_b/\rho \ll 1$ (a valid condition for most bubbles), the liquid velocity satisfies the condition of impermeability at the interface,

$$\mathbf{u} \cdot \mathbf{n}_b = \mathbf{v} \cdot \mathbf{n}_b. \tag{4}$$

However, the continuity with the gas velocities at the interface

$$\mathbf{u} \cdot \mathbf{n}_b = \mathbf{u}_g \cdot \mathbf{n}_b \tag{5}$$

is satisfied only in the absence of mass transfer across the interface. When we also consider the tangential velocity continuity at the bubble surface $\mathbf{u} \cdot \mathbf{t}_b = \mathbf{u}_g \cdot \mathbf{t}_b$, the gas and liquid velocities are equal at the bubble surface,

$$\mathbf{u} = \mathbf{u}_g. \tag{6}$$

As later discussed, this condition combined with a low viscosity in the gas induces a motion inside the bubble driven by the external liquid flow. As the domain formed by the bubble is closed, an internal toroidal recirculation develops.

2. Momentum conservation

Similarly, the conservation of momentum across a fluid interface can be used to complete the jump conditions at the bubble surface. When mass transfer across the interface is neglected, the normal component of the momentum conservation equation leads to

$$P_g - \mathbf{n}_b \cdot \boldsymbol{\Sigma}_g \cdot \mathbf{n}_b = 2H\sigma + P - \mathbf{n}_b \cdot \boldsymbol{\Sigma} \cdot \mathbf{n}_b, \tag{7}$$

where P and P_g are the pressures in the liquid and gas phases, respectively. $\boldsymbol{\Sigma}$ and $\boldsymbol{\Sigma}_g$ are the deviatoric viscous stress tensors for the liquid and gas phases, respectively. $H = 1/R_c$ is the local mean curvature of the interface, with R_c the mean radius of curvature. The surface tension of the interface is represented by σ. If the normal viscous stresses of both phases are neglected, it is possible to establish a condition for the pressure jump across the interface,

$$\Delta P = \frac{2\sigma}{R_c}. \tag{8}$$

For a spherical bubble of radius $R = R_c$, the pressure jump $\Delta P = P_g - P$ is constant across the interface. This relation is often referred to as the Young-Laplace equation.

As later discussed, the spherical shape of a bubble is the consequence of the surface tension that tends to minimize the surface area. However, when a bubble rises in a liquid (due to buoyancy or other forces), the forces induced by the motion can result in deformation of the bubble shape. In such a case, the resulting shape is determined by the balance among pressure, viscous, and surface tension forces at the interface. The relative importance of pressure and viscous forces at the interface for a bubble (neglecting viscous and inertial effects of the gas phase) compared to surface tension forces can be assessed by values of the Bond number (Bo), the Weber number (We), and the capillary number (Ca) [defined in Eqs. (20), (22), and (24), respectively]. A spherical shape is maintained as long as the surface tension stress σ/d_b can resist the dynamic pressure (We < 1), the hydrostatic pressure (Bo < 1), and the normal viscous stress (Ca < 1).

Considering now the tangential component of the momentum conservation at the interface, we can write

$$\mathbf{n}_b \cdot \boldsymbol{\Sigma}_g \cdot (\mathbf{I} - \mathbf{n}_b\mathbf{n}_b) = \boldsymbol{\nabla}_I\sigma + \mathbf{n}_b \cdot \boldsymbol{\Sigma} \cdot (\mathbf{I} - \mathbf{n}_b\mathbf{n}_b). \tag{9}$$

When the interface is surfactant-free and at a uniform temperature, σ is constant; therefore $\boldsymbol{\nabla}_I\sigma = 0$. Under such conditions and considering that $\mu_g \ll \mu$, Eq. (9) reduces to

$$\mathbf{n}_b \cdot \boldsymbol{\Sigma} \cdot (\mathbf{I} - \mathbf{n}_b\mathbf{n}_b) = 0, \tag{10}$$

which indicates that the liquid is subjected to a zero shear stress condition at the bubble surface. In other words, the bubble surface has a perfect slip condition. The presence of surfactants on the interface induces a gradient of surface tension $\boldsymbol{\nabla}_I\sigma \neq 0$ that significantly modifies the surface mobility and, consequently, the bubble dynamics. This is the so-called Marangoni effect, which is discussed in Sec. III.D.

B. Generation of bubbles

Bubbles can be produced as a result of complex breakup events such as those observed during breaking waves (Ruth *et al.*, 2022) (see Sec. III.C.4) or under well controlled conditions, as first discussed here. A bubble can be formed by injecting gas into a liquid or by mass diffusion from dissolved gas within the liquid; see Fig. 3. If mass transfer effects are not considered, then the bubble will grow by

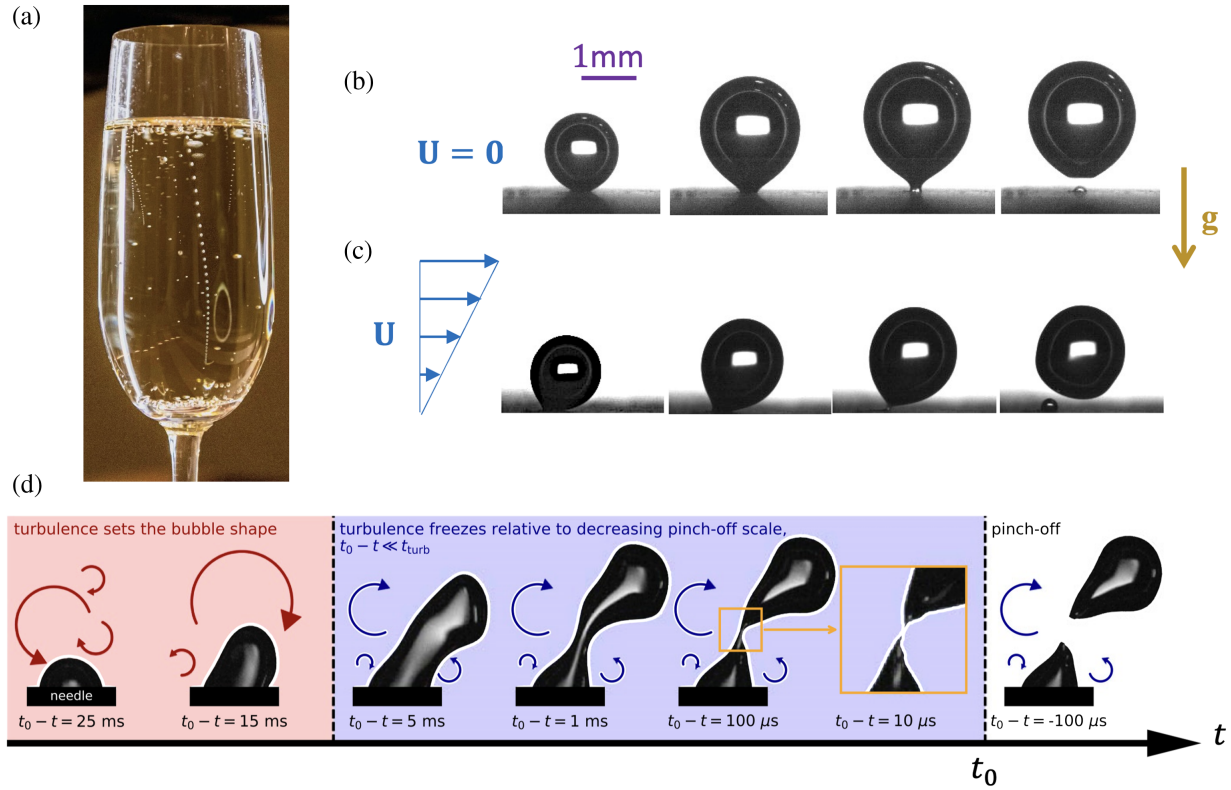

FIG. 3. Bubble generation on a wall in a vertical gravity field **g**. (a) In carbonated drinks bubbles are formed at nucleation sites, surface roughness or faults that allow the dissolved gas to grow into bubbles. From Atasi *et al.*, 2023. (b) From a capillary in a fluid at rest. (c) In a shear flow, which induces the bubble deformation along the flow and creates a vertical lift force in favor of the bubble detachment. Courtesy of C. Colin and J. Sebilleau. (d) By pinch-off in a turbulent shear flow in conditions where the turbulence shapes the bubble but has no significant impact on the pinch-off event, which occurs much faster (< 10 ms) than the turbulence timescale (here from 15 to 70 ms). From Ruth *et al.*, 2019.

forcing gas into the liquid using a capillary, a hole, or a flexible membrane. Consider first the case in which the liquid is stagnant and the gas flows slowly (i.e., neglecting inertial effects in both phases). A bubble can be formed at the tip of a capillary, connected to an external gas container at a pressure P_c. At first, the bubble will grow if P_c is larger than P_b. The pressure inside the bubble is

$$P_b = P_\infty + \frac{4\sigma}{D_c}, \tag{11}$$

where P_∞ is the pressure of the liquid around the bubble and D_c is the diameter of the capillary. As the bubble grows, its diameter will become larger than that of the capillary, D_c. At that point the pressure inside the bubble will be larger than that at equilibrium conditions. Hence, for the bubble to grow steadily, P_c must change dynamically. In practice, P_c is always larger than P_b (the overpressure condition). This is why most devices that generate bubbles do so under non-equilibrium conditions, leading to jetting and the production of bubbles with different diameters. This issue was discussed in depth by Oguz and Prosperetti (1993).

Assuming that the steady growth condition can be met, the bubble will remain attached to the tube by capillary forces, represented by $C\sigma$, where C is the wet perimeter of the capillary or hole. Attached to the capillary, the bubble will continue to grow until its buoyancy $\rho g \vartheta_b$ matches the capillary force. For a capillary with an inner diameter D_c, the detachment bubble diameter, often referred to as the Fritz diameter (Fritz, 1935), would be

$$d_b = k\left(\frac{D_c\sigma}{\rho g}\right)^{1/3}, \tag{12}$$

where $k = \sqrt[3]{6}$, for the case of a circular tube. The value of k changes for other geometries. If the bubble is formed at a hole rather than a thin-walled capillary tube, the wet perimeter depends on the details of the geometry of the hole (Simmons, Sprittles, and Shikhmurzaev, 2015). Similarly, if the bubble is formed at a flexible membrane, the size of the wet perimeter will depend on the pressure P_c. Since there are many techniques for producing bubbles by injecting pressurized gas through holes and tubes, numerous empirical correlations exist. While these correlations are useful, they often lack a strong physical basis. Kulkarni and Joshi (2005) addressed these correlations. The effects of the wall inclination and the type of substrate when bubbles nucleate on a wall were discussed by Lebon, Sebilleau, and Colin (2018).

In addition to buoyancy and inertial effects, as previously described, a bubble may detach from the surface of a capillary or a hole if a flow is imposed onto it while it is growing; see Figs. 3(c) and 3(d). The flow induces a drag force on the

bubble surface that can help dislodge the bubble at a size smaller than that predicted by Eq. (12). Force balance models have been developed that allow for predictions of the detachment size as a function of the gas flow rate and the liquid flow shear rate. An important aspect of this approach is the modeling of the contact line at the bubble foot (Duhar and Colin, 2006).

In many practical applications, gas bubbles can form in a liquid via gas diffusion. When gas is dissolved in the liquid, it may come out of solution, depending on the saturation level and the pressure; see Fig. 3(a). By neglecting advective transport, the bubble growth can be modeled using the Epstein-Plesset equation (Epstein and Plesset, 1950), which balances the mass flux from the fluid to the bubble by diffusion,

$$\dot{R} = \frac{(C_S - C_\infty)D}{\rho}\left(\frac{1}{R} + \frac{1}{\sqrt{\pi D t}}\right), \tag{13}$$

where the overdot indicates a time derivative, D is the mass diffusion coefficient, and C_S and C_∞ are the dissolved gas concentration at the surface and far from the bubble, respectively. The bubble size is proportional to $\sqrt{t}$ for long times, assuming that $C_S - C_\infty$ remains constant. Bubbles are formed by this mechanism when the fluid pressure is reduced. In such a case, the gas in the supersaturated fluid comes out of solution spontaneously. Bubbles are formed at nucleation sites such as small surface imperfections, crevices on the container, or small particles in the fluid. These bubbles grow until their buoyant force is large enough to dislodge them from their nucleation sites, according to Eq. (12). After the bubble detaches due to buoyancy, its size can evolve, but the convective mass transfer effect must be taken into account (Legendre and Zevenhoven, 2017; Moreno Soto *et al.*, 2019).

III. RISING BUBBLES: TERMINAL VELOCITY, DEFORMATION, AND INTERFACE CONTAMINATION

We begin our discussion by addressing the most basic question in bubble dynamics: What determines the terminal speed of an air bubble rising in water? Figure 4(a) shows the results from numerous experimental measurements aimed at answering this question. Once the bubble forms at the bottom of a container, its lower density will result in a buoyant force that will push the bubble upward. The buoyancy force, which arises from Archimedes's principle, is given by

$$\mathbf{F}_A = -\rho \vartheta_b \mathbf{g}. \tag{14}$$

The buoyancy force accelerates the bubble from rest and the bubble experiences a resistance from the fluid, the drag force $\mathbf{F}_D$, in the opposite direction of its velocity $\mathbf{u}_b$. When the drag force balances the buoyant force, the bubble no longer accelerates and reaches a constant speed, known as the terminal speed or velocity u_∞,

$$u_\infty = \mathbf{u}_b \cdot \mathbf{e}_y, \tag{15}$$

where $\mathbf{e}_y$ is the vertical coordinate along the gravity with $\mathbf{g} = -g\mathbf{e}_y$; see Fig. 2. In the case of unsteady rising motion

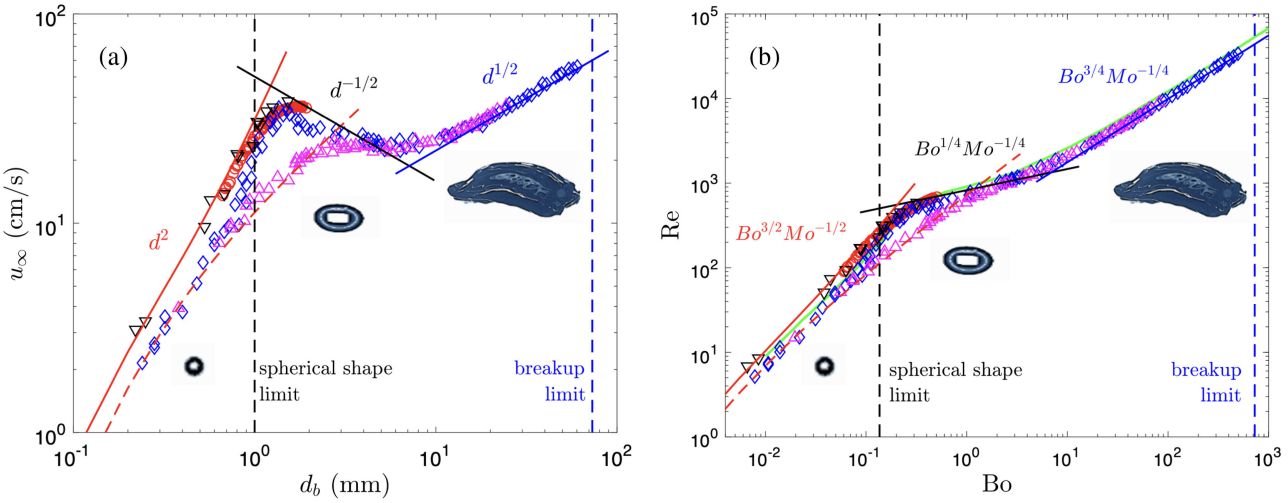

FIG. 4. (a) Terminal velocity u_∞ of an air bubble in water at room temperature as a function of its equivalent diameter d_b, defined in Eq. (16). The markers show experimental data from the literature: blue diamond, filtered water at 18–21 °C (Haberman and Morton, 1956); magenta triangle, tap water at 21 °C (Haberman and Morton, 1956); black down triangle, deionized water (20 °C) with particle concentration less than 18 parts/ml (Huang, Legendre, and Guiraud, 2011); and red circle, ultrapurified water at 19.6 °C with less than 10 ppb organic particles (Duineveld, 1995). The solid lines show the prediction for the terminal speed of a spherical bubble, and the corresponding trends u_∞ with d_b are reported as follows: red line, use of the drag force [Eq. (30)] for a clean spherical bubble; black line, Eq. (46) for an ellipsoidal bubble with We = 3.5; and blue line, Eq. (50) for a spherical cap bubble. The red dashed line shows the prediction for the terminal speed of a solid sphere (Schiller and Naumann, 1933) used to describe contaminated bubbles. The vertical dashed black line at $d_b = 1$ mm shows the condition for which We ≈ 1 when the bubble shape deviates from the spherical; see Sec. III.C. The vertical dashed blue line at $d_b = 73$ mm shows the condition for which Bo ≈ 730 and We ≈ 370, when bubble breakup is expected; see Sec. III.C.4. (b) The same plot in dimensionless terms: the (Bo, Re) phase diagram. The green line reports the iso-Morton curve Mo = 10^{-11} corresponding to water from the Clift-Grace-Weber diagram (Clift, Grace, and Weber, 1978).

because of a spiraling or zigzagging path (see Sec. III.C.2), u_∞ is then the mean value of the vertical rise speed. In a turbulent environment, the mean terminal rising velocity is noted as $\overline{u_\infty}$ and is compared to the corresponding terminal velocity u_∞ in the absence of turbulence in Sec. VIII.

In general, we neglect the effect of viscosity and the density of the gas inside the bubble here because $\mu_g/\mu \ll 1$ and $\rho_g/\rho \ll 1$. Note that although we consider the case of water for obvious reasons, once we express the results in dimensionless terms, the discussion is valid for any gas bubble in any viscous fluid.

The first observation from the data shown in Fig. 4(a) is that the bubble terminal velocity changes in a nonmonotonic way with the bubble diameter d_b. Initially, for diameters smaller than 0.5 mm, the bubble terminal speed increases with bubble size. For bubbles between 0.5 and 1.5 mm, the velocity continues to increase, but data show large dispersion. For a diameter of approximately 1.5 mm, the bubble velocity appears to decrease or remain roughly constant, with increasing bubble size until it reaches approximately 10 mm. For bubbles with sizes larger than this, the speed increases monotonically with size but at a different rate than small bubbles. As later detailed, these different behaviors are the consequence of bubble deformation and surface contamination by the presence of surfactants in the liquid. We first consider the bubble rising velocity in dimensionless terms. Then we introduce the drag force F_D, which is the main force that determines the value of the terminal rise velocity. Note that d_b generally represents the bubble equivalent diameter, which is defined as

$$d_b = \left(\frac{6\vartheta_b}{\pi}\right)^{1/3}, \tag{16}$$

where ϑ_b is the bubble volume.

A. Dimensional analysis

In most cases of practical interest, the density and viscosity of the gas are much smaller than those of the liquid ($\rho_b/\rho \ll 1$ and $\mu_b/\mu \ll 1$); therefore, their effect on bubble motion can be neglected. We can consider *a priori* the following fundamental variables that control the bubble rising velocity u_∞ in a fluid at rest: a characteristic size d_b, liquid with the density and viscosity ρ and μ, gravity g, and surface tension σ such that

$$u_\infty = f(d_b, \rho, \mu, g, \sigma). \tag{17}$$

According to the Π-Vaschy-Buckingham theorem, the dimensionless bubble speed depends only on two nondimensional groups. In the well-known Clift-Grace-Weber diagram (Clift, Grace, and Weber, 1978), the normalized bubble rising velocity is reported using the Reynolds number Re and plotted as a function of the bubble Bond number (Bo) [also often called the Eötvös number (Eo)] for fixed values of the Morton number (Mo),

$$\mathrm{Re} = \mathcal{F}(\mathrm{Bo}, \mathrm{Mo}), \tag{18}$$

that are defined as

$$\mathrm{Re} = \frac{\rho d_b u_\infty}{\mu}, \tag{19}$$

$$\mathrm{Bo} = \frac{\rho g d_b^2}{\sigma}, \tag{20}$$

$$\mathrm{Mo} = \frac{g\mu^4}{\rho\sigma^3}. \tag{21}$$

The Reynolds number (Re) classically compares inertial to viscous effects. The Bond number is a comparison of the bubble diameter to the capillary length scale $\ell_c = \sqrt{\sigma/\rho g}$. The Morton number has a unique value for a given liquid-gas combination; it is obtained by combining inertia, viscous, surface tension, and gravity effects to eliminate d_b and u_∞.

The experimental data reported in Fig. 4(a) for air bubbles in water correspond to a unique value of the Morton number, $\mathrm{Mo} \approx 2 \times 10^{-11}$. In Fig. 4(b), the same data are presented in terms of (Bo, Re). We also show a comparison with the iso-Morton curve $\mathrm{Mo} = 10^{-11}$ extracted from the Clift-Grace-Weber diagram (Clift, Grace, and Weber, 1978). For each liquid-gas combination, a relationship $\mathrm{Re} = \mathcal{F}(\mathrm{Bo}, \mathrm{Mo})$ exists.

There are other dimensionless numbers that can be formed using these variables. They are used in the literature depending on the regime at which bubbles move and the physical terms they compare. Some often-used numbers are

$$\mathrm{We} = \frac{d_b u_\infty^2 \rho}{\sigma} = \frac{\sqrt{\mathrm{Mo}}\mathrm{Re}^2}{\sqrt{\mathrm{Bo}}} \quad \text{(Weber number)}, \tag{22}$$

$$\mathrm{Oh} = \frac{\mu}{\sqrt{\rho\sigma d_b}} = \frac{\sqrt{\mathrm{We}}}{\mathrm{Re}} \quad \text{(Ohnesorge number)}, \tag{23}$$

$$\mathrm{Ca} = \frac{\mu u_\infty}{\sigma} = \frac{\mathrm{We}}{\mathrm{Re}} \quad \text{(capillary number)}, \tag{24}$$

$$\mathrm{Ga} = \frac{g d_b^3 \rho^2}{\mu^2} = \frac{\mathrm{Mo}\mathrm{Re}^6}{\mathrm{We}^3} \quad \text{(Galilei number)}, \tag{25}$$

$$\mathrm{Fr} = \frac{u_\infty}{\sqrt{g d_b}} = \frac{\mathrm{We}^{3/2}}{\mathrm{Re}^2\mathrm{Mo}^{1/2}} \quad \text{(Froude number)}. \tag{26}$$

The Weber number (We) compares the inertial and surface tension forces. In contrast, the capillary number (Ca) compares the viscous forces to the surface tension forces. Bubbles with small values of Bo, We, and Ca would be spherical due to the dominance of surface tension forces. In many practical applications, the Ohnesorge number (Oh) is used to identify the conditions at which a droplet or bubble can fragment, either by viscous stresses or inertial forces. The Galilei number (Ga) (often also called Archimedes number) is the square of the Reynolds number using $\sqrt{g d_b}$ as the characteristic speed instead of u_∞; this quantity is used in many studies of bubble dynamics when the bubble terminal velocity is unknown to begin with (Tripathi, Sahu, and Govindarajan, 2015).

Note that when the fluid is not at rest, the terminal velocity u_∞ in the definitions of the aforementioned dimensionless numbers should be replaced by the norm of the relative velocity $U_\infty = \|\mathbf{U}_\infty\| = \|\mathbf{U} - \mathbf{u}_b\|$, as defined in Fig. 2.

B. Terminal velocity of a spherical bubble

1. Drag force

Keeping in mind that for bubbles in liquids $\mu_g/\mu \ll 1$, it is reasonable to assume that the external fluid is free to slip at the bubble surface as illustrated in Fig. 6(a). This slip condition resembles the one that results from the potential flow around objects. Hence, a naive interpretation would conclude that the drag force around the bubble is zero considering the d'Alembert paradox. However, the viscous fluid is displaced by the moving bubble, resulting in deformation and thus viscous dissipation. The drag force $\mathbf{F}_D$ experienced by the bubble can therefore be inferred from the total viscous dissipation in the liquid considering (Levich, 1962; Batchelor, 1967)

$$\mathbf{F}_D \cdot \mathbf{u}_b = -\int_\vartheta 2\mu \mathbf{S}:\mathbf{S} d\vartheta, \tag{27}$$

where ϑ is the liquid volume and $\mathbf{S}$ is the strain-rate tensor. Note that Eq. (27) is valid for any flow regime, i.e., any Re.

We first consider the solution from creeping flow Re $\ll 1$ of a bubble moving at velocity $\mathbf{u}_b$ in a fluid at rest $\mathbf{U} = 0$. In that case the velocity field decays from the bubble center as $u_b R/r$ and the rate of deformation evolves as $u_b R/r^2$, where r is the radial distance from the bubble center and $R = d_b/2$ is the bubble radius, used here for convenience. Therefore, $\mu\mathbf{S}:\mathbf{S} \sim \mu u_b^2 R^2/r^4$ and, from the integral in Eq. (27), $F_D \propto \mu R u_b$ (linearly with viscosity, bubble size, and speed), which has the same scaling as the Stokes drag force of a solid sphere in the same condition, $\mathbf{F}_D = -6\pi\mu R\mathbf{u}_b$ (Stokes, 1851). For the case of a bubble, from the exact flow field obtained by Hadamard (1911) and Rybczynski (1911), the drag force and the drag coefficient C_D when considering its classical definition, $C_D = 2F_D/\pi R^2 \rho u_b^2$, are

$$\mathbf{F}_D = -4\pi\mu R\mathbf{u}_b, \qquad C_D = \frac{16}{\mathrm{Re}}. \tag{28}$$

As expected, the drag force on a bubble is smaller than that of a solid sphere because of the slip boundary condition at the bubble surface, which reduces the friction on the interface. However, the difference is not so large; the prefactor is 4π instead of 6π. This can be explained by the fact that in both cases a similar amount of liquid displacement occurs. This motion contributes to the integral in Eq. (27) in a similar manner, as the momentum associated with the bubble motion is diffused over a domain around the moving bubble of size R/Re, which is much larger than the bubble or particle size.

In the limit of a large bubble Reynolds number (Re $\gg 1$), the vorticity generated at the bubble surface is finite and of order $O(u_b/R)$ (discussed later). More importantly, vorticity remains confined to a layer of thickness $R/\mathrm{Re}^{1/2}$, $R/\mathrm{Re}^{1/4}$, and $R/\mathrm{Re}^{1/6}$ at the bubble surface, the near wake, and the far wake, respectively (Moore, 1963). Consequently, these regions of vorticity decrease in size with increasing Re and the potential flow can then be considered a good approximation for calculating the drag force using Eq. (27). The velocity field obtained from potential flow decays as $u_b R^3/r^3$. Therefore, the deformation rate evolves as $u_b R^3/r^4$ and thus $\mu\mathbf{S}:\mathbf{S} \sim \mu u_b^2 R^6/r^8$. From Eq. (27), the drag force scales as $F_D \sim \mu R u_b$, which has the same scaling as a Stokes drag force but differs from the drag of a solid sphere at large Reynolds numbers. This point is discussed later. The exact calculation, considering the potential flow solution around a bubble, was first conducted by Levich (1962) and results in

$$\mathbf{F}_D = -12\pi\mu R\mathbf{u}_b, \qquad C_D = \frac{48}{\mathrm{Re}}. \tag{29}$$

We can now discuss the evolution of the drag force, and correspondingly the drag coefficient, from small to large Re for a spherical bubble. Different analytical expressions have been derived to extend the Stokes solution (Hadamard, 1911; Rybczynski, 1911) to a Reynolds number of order unity (Acrivos and Taylor, 1962) and to extend the Levich solution (Levich, 1962) to a Reynolds number of order 50 (Moore, 1963). It is not possible to find an analytical expression for intermediate values of Re, but an accurate fit was obtained using direct numerical simulations, i.e., by solving the entire Navier-Stokes equations, by Mei and Klausner (1992). In its general form when the liquid is moving at velocity $\mathbf{U}$, the expression is

$$\mathbf{F}_D = 4\pi\mu R\mathcal{K}(\mathrm{Re})(\mathbf{U} - \mathbf{u}_b), \qquad C_D = \frac{16}{\mathrm{Re}}\mathcal{K}(\mathrm{Re}), \tag{30}$$

where $\mathcal{K}(\mathrm{Re})$ connects the small Re to the large Re drag force evolution,

$$\mathcal{K}(\mathrm{Re}) = \frac{16 + 3.315\mathrm{Re}^{1/2} + 3\mathrm{Re}}{16 + 3.315\mathrm{Re}^{1/2} + \mathrm{Re}}. \tag{31}$$

All of these expressions are shown in Table I and plotted in Fig. 5. As indicated in Eq. (30), the relevant characteristic velocity to consider is $\mathbf{U} - \mathbf{u}_b$, so the Reynolds number is now written as

$$\mathrm{Re} = \frac{d_b\|\mathbf{U} - \mathbf{u}_b\|\rho}{\mu}. \tag{32}$$

2. Terminal velocity

Since the drag and buoyancy forces are known from Eqs. (30) and (14), respectively, an explicit expression for the terminal speed u_∞ of a spherical bubble can be obtained considering a steady balance, leading to

$$u_\infty = \frac{1}{12\mathcal{K}(\mathrm{Re})}\frac{\rho g d_b^2}{\mu}, \tag{33}$$

where the prefactor $(12\mathcal{K}(\mathrm{Re}))^{-1}$ varies from $1/12$ to $1/36$ from small to large Re. Equation (33) shows that u_∞ is

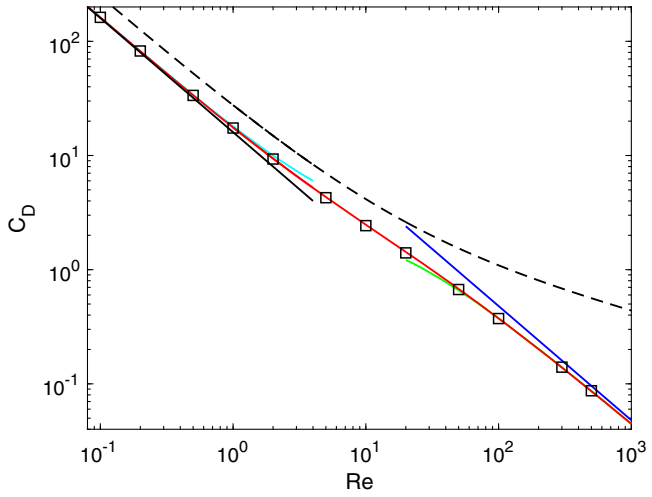

FIG. 5. Drag coefficient C_D as a function of Re for a spherical bubble. The squares represent direct numerical simulations from Legendre and Magnaudet (1998). The solid lines show the relations for a clean bubble; see Table I for each line symbol. The red line shows the prediction from Eq. (31). The dashed line is the prediction for a solid sphere used to describe a contaminated bubble; see also Table I.

proportional to d_b^2, which is in accordance with the trend shown by the data in Fig. 4(a) for diameter smaller than 1 mm.

3. Scaling of the drag force at large Reynolds numbers

For a spherical bubble moving at large Re, the drag coefficient is inversely proportional to the Reynolds number, as indicated by Eq. (29). This behavior at large Reynolds numbers differs from the drag force experienced by a solid sphere moving at the same speed, u_S. If the flow is dominated by inertial effects, we expect $F_D \propto \rho R^2 u_S^2$, which would result in a constant drag coefficient. The drag coefficient of a solid sphere is $C_D \approx 0.45$ for $\mathrm{Re} > 800$, while the drag is found to be $F_D \propto \mu R u_b$ for a spherical bubble resulting in $C_D = 48/\mathrm{Re}$. This significant difference can be explained by the flow separation and the induced recirculation that develops in the wake of a solid sphere when Re increases. The flow around a spherical bubble instead resembles that predicted by potential flow without any recirculation (Dandy and Leal, 1986; Blanco and Magnaudet, 1995). At large Reynolds number, the drag force is given mainly by the pressure distribution on the surface and can be estimated from the pressure evolution as $F_{D,P} \approx \Delta P S$, where ΔP is the characteristic pressure variation between the top and bottom parts of the sphere [$\theta = 0$ and $\theta = \pi$, respectively, according to Fig. 6(a)] and $S = 4\pi R^2$ is the sphere surface. In both cases the pressure on the top of the surface (bottom of the surface) is given by the dynamic pressure $\rho u_b^2/2$ ($\rho u_S^2/2$). In the case of a bubble, the pressure distribution on the surface is close to being upstream-downstream symmetrical, as in the case of potential flow, with some deviation resulting from viscous effects located in a boundary layer of thickness $\sim d_b/\mathrm{Re}^{1/2}$, so $\Delta P = O(\mu u_b/d_b)$ and $F_{D,P} \sim \mu R u_b$. In contrast, for a solid sphere, the dynamic pressure is not recovered downstream, because of the flow separation and the resulting recirculation in the wake, so $\Delta P = O(\rho u_S^2)$ and $F_{D,P} \sim \rho R^2 u_S^2$, leading to a constant value of the drag coefficient. To support this discussion, a comparison of pressure distribution between a spherical bubble and a solid sphere was given by Magnaudet, Rivero, and Fabre (1995).

4. Drag and production of vorticity at the bubble surface

According to Legendre (2007), the magnitude of the drag force on a bubble can be written in terms of the maximum of the surface vorticity as

$$F_D = 4\pi\mu R^2 \omega_I^{\max}. \tag{34}$$

For an axisymmetric flow for a spherical bubble, the surface vorticity is directed along the azimuthal direction and can be expressed as a function of the surface velocity u_I as

$$\omega_I = \frac{1}{R}\frac{\partial u_I}{\partial \theta} + \frac{u_I}{R}, \tag{35}$$

where u_I is the tangential fluid velocity at the bubble surface in the reference frame moving with the bubble and the fluid velocity far from the bubble is $\mathbf{U}_\infty = \mathbf{U} - \mathbf{u}_b$. Since the gas viscosity inside the bubble has a negligible effect and considering a clean surface, the liquid experiences a zero shear stress at the bubble surface $(1/R)(\partial U_I/\partial\theta) - u_I/R = 0$. Therefore, the interfacial vorticity is then

$$\omega_I = 2\frac{u_I}{R}. \tag{36}$$

TABLE I. Drag force $\mathbf{F}_D$ and drag coefficient C_D for a spherical bubble over a wide range of Reynolds numbers. The expressions are given for the general configuration of a bubble moving at velocity $\mathbf{u}_b$ in a fluid of local velocity $\mathbf{U}$. The drag force is then directed along the relative velocity $\mathbf{U}_\infty = \mathbf{U} - \mathbf{u}_b$, as defined in Fig. 2. The function $\mathcal{K}(\mathrm{Re})$ is given by Eq. (31).

Range	Drag force $\mathbf{F}_D$	Drag coefficient C_D	Method and source
$\mathrm{Re} \ll 1$ (black line)	$4\pi\mu d_b \mathbf{U}_\infty$	$16/\mathrm{Re}$	Analytical solution (Hadamard, 1911; Rybczynski, 1911)
$\mathrm{Re} \leq 1$ (cyan line)	$4\pi(1 + \mathrm{Re}/8)\mu d_b \mathbf{U}_\infty$	$16/\mathrm{Re} + 2$	Analytical solution (Acrivos and Taylor, 1962)
All Re (red line)	$4\pi\mathcal{K}(\mathrm{Re})\mu d_b \mathbf{U}_\infty$	$(16/\mathrm{Re})\mathcal{K}(\mathrm{Re})$	Numerical data fit (Mei and Adrian, 1992)
$\mathrm{Re} \geq 50$ (green line)	$12\pi(1 - 2.211/\sqrt{\mathrm{Re}})\mu d_b \mathbf{U}_\infty$	$(48/\mathrm{Re})(1 - 2.211/\sqrt{\mathrm{Re}})$	Analytical solution (Moore, 1963)
$\mathrm{Re} \gg 1$ (blue rule)	$12\pi\mu d_b \mathbf{U}_\infty$	$48/\mathrm{Re}$	Analytical solution (Levich, 1962)
$\mathrm{Re} \leq 800$ (dashed black line) contaminated bubble	$6\pi(1 + 0.15\mathrm{Re}^{0.687})\mu d_b \mathbf{U}_\infty$	$(24/\mathrm{Re})(1 + 0.15\mathrm{Re}^{0.687})$	Empirical fit (Schiller and Naumann, 1933)

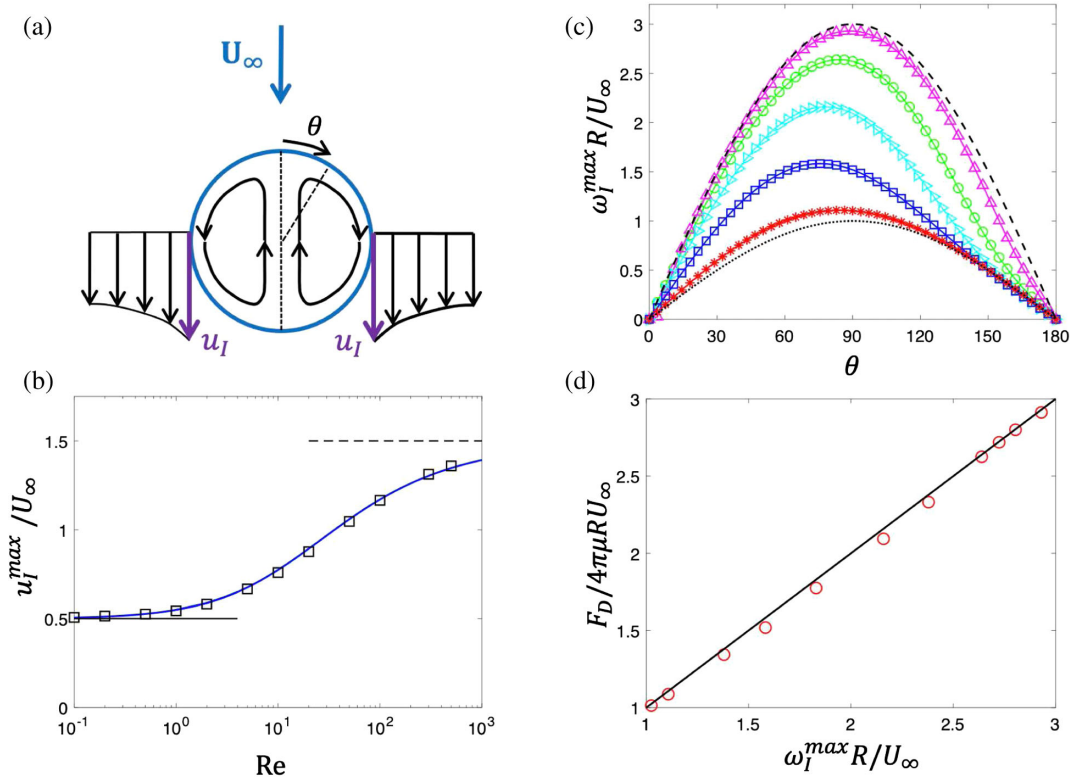

FIG. 6. (a) Schematic of the flow around and inside a bubble shown in the frame of reference $\mathcal{R}_b$ (see Fig. 2) moving with the bubble. (b) Normalized maximum interfacial velocity $u_I^{\max}$ as a function of Re. Blue line, Eq. (37); black line, $u_I^{\max} = 1/2U_\infty$, Stokes solution from Hadamard (1911) and Rybczynski (1911); dashed black line, $u_I^{\max} = 3/2U_\infty$, a potential flow solution; and squares, a direct numerical solution from Legendre (2007). (c) Surface distribution of vorticity obtained from a direct numerical simulation from Legendre (2007). Red asterisks, Re = 1; blue squares, Re = 10; cyan right triangles, Re = 50; green circles, Re = 300; magenta triangles, Re = 5000; dotted black line, Stokes flow; and dashed black line, potential flow. (d) The normalized drag force $F_D/4\pi\mu RU_\infty$ as a function of the normalized maximum surface vorticity $\omega_I^{\max}R/U_\infty$. Symbols are from the numerical results shown in (c). The black line is the parity line.

Figure 6(c) shows the surface vorticity distribution for different Reynolds numbers varying from 0.1 to 5000 calculated from direct numerical simulations (Legendre, 2007). These results show that ω_I varies continuously from the Stokes solution $[U_\infty \sin(\theta)/R$ from Hadamard (1911) and Rybczynski (1911)] to the potential flow solution $(3U_\infty \sin(\theta)/R]$, which was obtained from the potential flow on a sphere surface $u_I = 1.5U_\infty \sin(\theta)$ in Eq. (36). Figure 6(c) shows that, owing to the absence of any recirculation in the wake, for Re = 1000 the solution is close to the one imposed by the potential flow. This result differs drastically from the classical picture of the flow around a solid sphere where a recirculation develops at large Re, thus increasing the drag force. From Fig. 6(c) the maximum vorticity $\omega_I^{\max}$ is measured, and the evolution of the normalized drag force $F_D/4\pi\mu RU_\infty$ is reported in Fig. 6(d) as a function of the normalized maximum interfacial vorticity $\omega_I^{\max}R/U_\infty$ to demonstrate Eq. (34). This reveals that the drag force is directly proportional to how much vorticity is produced at the bubble surface. As discussed later, the surface vorticity is relevant to understanding many aspects of the bubble dynamics considered in this review.

Finally, comparing Eqs. (34) and (30), the maximum vorticity at the bubble surface varies as

$$\omega_I^{\max} = \frac{U_\infty}{R}\mathcal{K}(\mathrm{Re}), \tag{37}$$

with $\mathcal{K}(\mathrm{Re})$ as given in Eq. (30). Figure 6(b) shows how the maximum value of $u_I^{\max} = \omega_I^{\max}R/2$ evolves with Re, calculated from direct numerical simulations (Legendre, 2007). This evolution is well fitted with Eq. (37). Note that the relation between the maximum surface vorticity and the drag force is also observed for ellipsoidal bubbles with an axisymmetric wake, as discussed by Legendre (2007).

C. Bubble deformation and rupture

The shape of a gas bubble is determined by a balance among surface tension forces, hydrostatic pressure, viscous, and inertial forces that grow in magnitude depending on the flow condition, flow regime, and bubble size. Figure 7 shows some examples of different shapes that bubbles can adopt. Bubble deformation has been extensively described in the literature (Clift, Grace, and Weber, 1978; Maxworthy *et al.*, 1996), and we report here the main findings for bubbles rising at their terminal velocity u_∞ in a liquid at rest.

The spherical shape is a consequence of the dominance of surface tension, which acts to minimize the surface area.

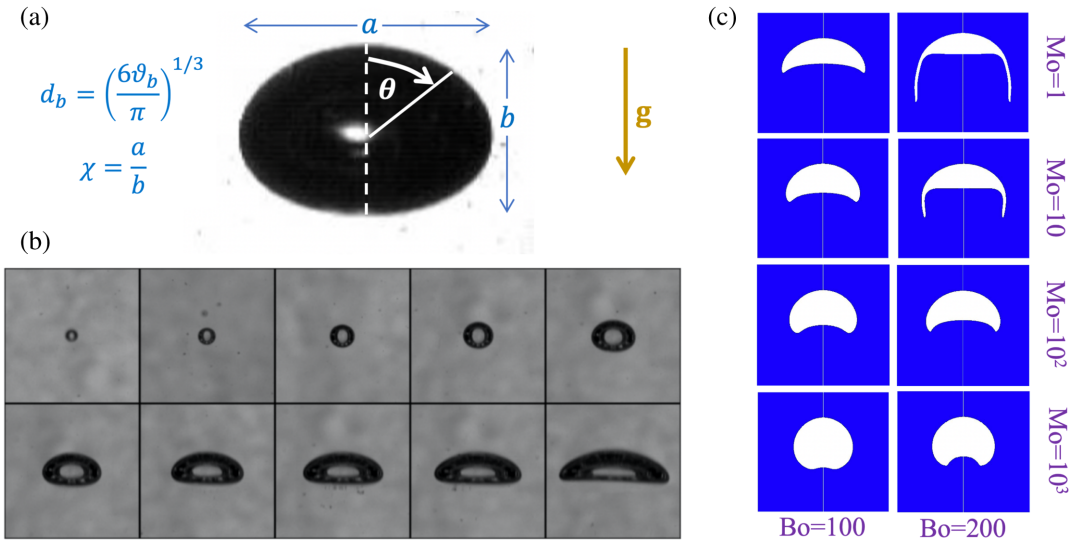

FIG. 7. (a) Definition of the bubble equivalent diameter d_b and aspect ratio $\chi = a/b$. (b) Evolution of the bubble shape with increasing equivalent bubble diameter d_b in a 90% glycerin-water solution. d_b ranges from 2.5 to 10 mm [$O(10^{-2}) < Re < O(10^2)$, $Mo \sim O(10^{-3})$]. From Ravisankar, 2021. (c) Bubble shapes obtained from numerical simulations for $Bo \geq 100$ and a Morton number ranging from 1 to 10^3 showing spherical cap, dimpled, and skirt bubbles. In all cases the images show a side view of the bubbles. From Legendre, 2022.

When a bubble rises in a liquid, its shape then results from the normal stress balance at its interface. As discussed, the effect of the inertia and normal viscous stress from the gas phase can be neglected in the momentum balance [Eq. (7)], resulting in

$$P_g = 2H\sigma + P - \mathbf{n}_b \cdot \boldsymbol{\Sigma} \cdot \mathbf{n}_b, \tag{38}$$

where P_g is the pressure inside the bubble. Because both gas inertia and viscosity effects are negligible inside the bubble, P_g is considered constant and uniform in the following discussion.

From Eq. (38) we argue that the bubble will depart from a spherical shape when the magnitude of either the pressure or the viscous stress becomes of order σ/d_b. The contributions to bubble deformation [the second and third terms on the right-hand side of Eq. (38)] include pressure changes due to a hydrostatic head $\rho g d_b$, the dynamic pressure ρu_b^2, and the viscous stresses $\mu u_b/d_b$. Comparing these effects to σ/d_b, we can form three dimensionless groups, Bo, We, and Ca, defined by Eqs. (20), (22) and (24), respectively. Hence, we can expect a deviation from a spherical bubble shape when at least one of the following conditions is met:

$$\mathrm{Bo} > 1, \quad \mathrm{We} > 1, \quad \mathrm{Ca} > 1. \tag{39}$$

Note that when inertial effects are negligible ($Re \to 0$), the shape of a rising bubble is spherical regardless of the values of Bo, We, and Ca. In this case the viscous and gravitational contributions are balanced across the bubble surface, as shown by Taylor and Acrivos (1964).

When inertia is present ($Re > 1$), the conditions in Eq. (39) can be used to determine the critical diameter at which a bubble is expected to deform while rising in a liquid. The condition $Bo > 1$ implies that the bubble diameter is larger than the capillary length, $\ell_c = \sqrt{\sigma/\rho g}$. For an air bubble in water, this implies that the bubble should have a diameter (volume) d_b (ϑ_b) larger than 2.7 mm (1.4 mm^3). The condition $Ca > 1$ for air-water properties implies that the bubble velocity would have to be larger than $\sigma/\mu = 72$ m/s, which is well beyond what is observed experimentally under standard gravitational conditions; see Fig. 4. Therefore, viscous-induced deformation is expected to be negligible for water but may be relevant for more viscous fluids. For $We > 1$, we can consider the terminal velocity $u_\infty = \rho g d_b^2/36\mu$ inferred from Eq. (33) in the $Re \gg 1$ regime since the viscous effects are small. Therefore, for a bubble to deform due to inertial effects, $d_b \geq (36^2\sigma\nu^2/g^2\rho)^{1/5}$. For air-water properties, $u_\infty = 27$ cm/s and $d_b > 1$ mm ($\vartheta_b > 0.52$ mm^3). This limit is shown in Fig. 4, which coincides with the transition when the bubble velocity departs from the d_b^2 dependence. This indicates that when the bubble shape is no longer spherical, its terminal speed is affected by the deformation.

When bubbles are deformed, their characteristic size can be defined based on their volume ϑ_b, which is independent of the deformation. The equivalent bubble diameter d_b is defined in Eq. (16). Bubble deformation is usually characterized by the bubble aspect ratio χ, which is defined as

$$\chi = \frac{a}{b}, \tag{40}$$

where a and b are the larger and smaller dimensions of the bubble, respectively, as depicted in Fig. 7. Note that in some studies, the bubble deformation is described using the inverse of χ, namely, $E = b/a$, resulting in values smaller than 1 (Aoyama *et al.*, 2017).

1. Ellipsoidal shape

Based on the previous discussion, we expect that, for a gas bubble in a liquid, the effect of dynamic pressure will first

induce a change of the bubble shape. If Re is large, we can assume that the potential flow prediction correctly models the flow around the bubble. From such a solution, the pressure distribution can be used to write the normal stress balance [Eq. (38)] as

$$P_g = 2H\sigma + P_o - \tfrac{9}{8}\rho u_\infty^2 \sin\theta, \tag{41}$$

where θ is the azimuthal angle measured to be zero at the bubble top. For $\theta = 0$ we have $P_g = P_o + 2H_{\text{top}}\sigma$, which fixes the reference pressure. For other values of θ, moving along the bubble surface, we have

$$H = H_{\text{top}} + \frac{9}{16}\frac{\rho u_\infty^2}{\sigma}\sin\theta. \tag{42}$$

Since the surface tension remains the same, the radii of curvature of the bubble surface is observed to increase. Therefore, at $\theta = 0$ or π, the bubble curvature is minimum H_{top}, but at $\theta = \pm\pi/2$ at the bubble equator, $H_{\text{equator}} - H_{\text{top}} = (9/16)(\rho u_\infty^2/\sigma)$. We see that the relative change in shape, when normalized by the bubble diameter, is controlled by We. As a result, the bubble becomes flattened along the rising direction, taking on a shape similar to an ellipsoid with the small axis parallel to the direction of its ascent. This change in shape increases the bubble's drag force. The bubble velocity then decreases, as shown in the velocity evolution in Fig. 4, for bubble diameters ranging from 1 mm to 1 cm.

The bubble deformation and the induced change in drag force were first studied by Taylor and Acrivos (1964) for small Reynolds numbers and by Moore (1965) for large Reynolds numbers. For small bubble deformations, the bubble aspect ratio and drag coefficient include We corrections in both large and small Re limits. Hence, the Weber number is the relevant nondimensional number for deformation effects when inertia is present. Note that in some studies the bubble deformation is characterized using Bo (Aoyama *et al.*, 2017). When considering a bubble velocity scale of $u_\infty \propto \sqrt{g d_b}$, We and Bo become equivalent.

For Re $\ll 1$ Taylor and Acrivos (1964) reported that

$$\chi = 1 + \frac{5}{32}\text{We}, \qquad C_D = \frac{16}{\text{Re}}\left[1 + \frac{\text{Re}}{8} + \frac{\text{We}}{12}\right]. \tag{43}$$

In the limit We $\to 0$ ($\chi \to 1$), the analytical expression by Taylor and Acrivos for spherical bubbles is recovered; see Table I. For the opposite limit of a large Reynolds number (Re $\gg 1$), Moore (1965) obtained

$$\chi = 1 + \frac{9}{64}\text{We}, \qquad C_D = \frac{48G(\chi)}{\text{Re}}\left[1 + \frac{H(\chi)}{\text{Re}^{1/2}}\right], \tag{44}$$

where $G(\chi)$ and $H(\chi)$ are implicit functions of χ that were employed by Moore (1965). In the limit We $\to 0$ ($\chi \to 1$), the functions tend to $G(\chi) \to 1$ and $H(\chi) \to -2.21$. In such a case, the Moore analytical expression for spherical bubbles is recovered; see Table I.

Based on these findings, many experiments to determine the bubble shape have been performed for different fluids and bubble sizes. Legendre, Zenit, and Velez-Cordero (2012) used these studies to develop a correlation describing bubble deformation over a wide range of Morton numbers applicable in conditions ranging from water [Mo $= \text{O}(10^{-11})$] to water-glycerin solutions [Mo $= \text{O}(1)$],

$$\chi = \frac{1}{1 - (9/64)\text{We}(1 + 0.2\text{Mo}^{1/10})^{-1}}. \tag{45}$$

For small to moderate deformation, the surface tension and dynamic pressure effects balance at the surface, resulting in a shape for which We is approximately constant (Maxworthy *et al.*, 1996). A constant Weber number indicates that the terminal velocity is now decreasing with the diameter, as described by

$$u_\infty \propto \left(\frac{\sigma}{\rho d_b}\right)^{1/2}. \tag{46}$$

This trend is shown in Fig. 4, which appears to agree with experimental observations for bubble diameters between 1 and 10 mm. In Fig. 4 Eq. (46) is plotted with the prefactor 1.87 corresponding to a Weber number We ≈ 3.5. For diameters larger than 10 mm, the bubble velocity increases again, which corresponds to the next behavior regime (the spherical cap regime), which is described later.

2. Zigzagging bubbles

A significant behavior appears during the rise of such ellipsoidal bubbles. After a critical diameter $d_b \approx 1.8$ mm ($\vartheta_b \approx 0.94$ mm^3) for an air bubble in water, the trajectory ceases to be rectilinear and instead follows zigzagging or spiraling paths (Saffman, 1956; Hartunian and Sears, 1957; Aybers and Tapucu, 1969; Lunde, 1997; de Vries, Biesheuvel, and van Wijngaarden, 2002). Leonardo da Vinci observed and documented this behavior in the first scientific reference of the phenomenon (Roberts, 1981). These noteworthy images, which are shown in Fig. 1(a), were discovered by Professor Andrea Prosperetti (Prosperetti, 2004), who coined the term *Leonardo's Paradox*. Magnaudet and Eames (2000) gave a summary of the many experimental studies and attempts to understand the nature of the instability, which was not fully understood when their review was written.

It is now clear that the path instability originates from the instability of the wake behind the bubble. The conditions for the appearance of the wake instability remained unclear because most of the experimental evidence was for air bubbles in water, which is subject to surface contamination. The publication of experimental measurements for ultrapurified water (Duineveld, 1995), along with the development of numerical techniques capable of reproducing the structure of the wake behind bubbles (Blanco and Magnaudet, 1995), reignited interest in the subject. When the bubble shape exceeds a critical aspect ratio, its wake transitions from being axisymmetric to displaying a double threaded with counterrotating streamwise vorticity, as shown in Fig. 8 (Lunde, 1997; de Vries, Biesheuvel, and van Wijngaarden, 2002; Zenit and Magnaudet, 2009). In a series of papers, Mougin and Magnaudet (2001, 2006, 2007), Tchoufag,

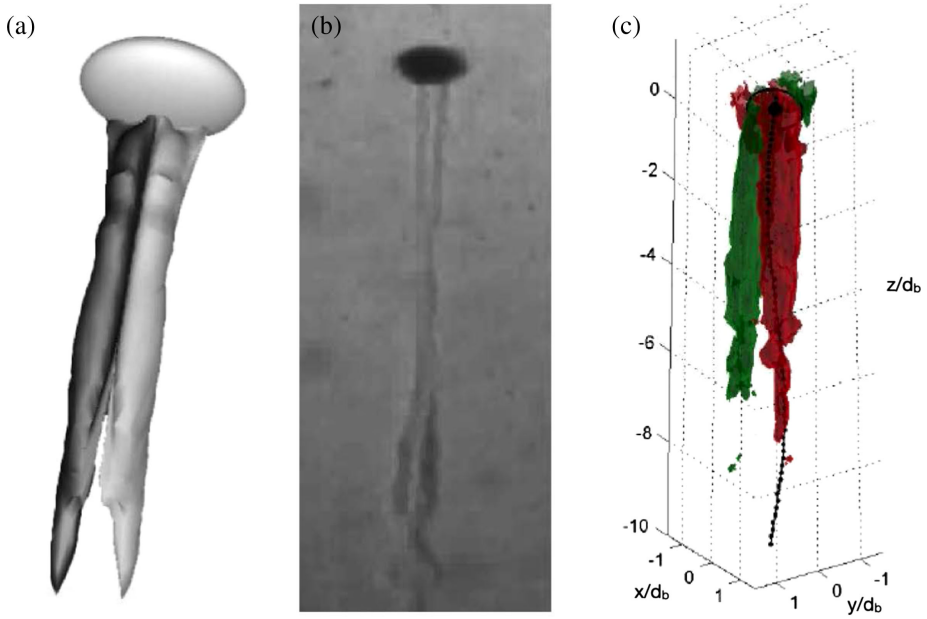

FIG. 8. The wake behind zigzagging bubbles. (a) Numerical result for a fixed-shape ellipsoidal bubble from Mougin and Magnaudet (2001). (b) Schlieren images of the wake behind a 2 mm diameter air bubble in zigzagging motion in purified water. From de Vries, Biesheuvel, and van Wijngaarden, 2002. (c) Reconstruction of the wake behind a zigzagging bubble rising in silicone oil. From Zenit and Magnaudet, 2009.

Magnaudet, and Fabre (2013, 2014), Cano-Lozano, Martínez-Bazán *et al.* (2016), and Cano-Lozano, Tchoufag *et al.* (2016), using direct numerical simulations and linear stability analysis, developed a detailed picture of the nature of this instability. In their most recent paper, Bonnefis, Fabre, and Magnaudet (2023) demonstrated that path instability always arises from the destabilization of a nonaxisymmetric mode. As the bubble size increases, this primary instability, tied to a fixed bubble shape, remains unchanged for Morton numbers larger than 10^{-7}, which are associated with weak, time-dependent changes in bubble shape. They also found that time-dependent bubble deformation does not play a causal role in the first stages of the path instability for low-Mo liquids.

3. Spherical cap shape

When the bubble volume increases, the shape evolves into a spherical cap shape (see Fig. 7) and the bubble trajectory regains a rectilinear rising path. The shape is now governed by the balance between the fluid inertia and the hydrostatic pressure balance at the interface, $\rho u_\infty^2 \propto \rho g d_b$, resulting in

$$u_\infty \propto \sqrt{g d_b}. \tag{47}$$

This dependence of u_∞ with d_b is shown in Fig. 4 for $d_b > 10$ mm, which is again in good agreement with experiments. By balancing the buoyancy force $\rho g(\pi/6)d_b^3$ with the drag force $C_D(1/8)\pi d_b^2 \rho u_\infty^2$, we can write

$$\mathrm{Fr}^2 = \frac{u_\infty^2}{g d_b} = \frac{4}{3}\frac{1}{C_D}. \tag{48}$$

Combining Eqs. (47) and (48) results in a constant Froude number and a constant drag coefficient. Note that for a solid object a regime of the constant drag coefficient, sometimes called the Newton regime, is also observed, but its origin is completely different, as detailed in Sec. III.B.3.

When we consider the potential flow approximation at the front of a spherical cap bubble, the pressure distribution $(9/8)\rho u_b^2 \sin^2\theta$ is balanced by the variation in the liquid's hydrostatic pressure $\rho g a(1-\cos\theta)$, where a is the radius of the spherical cap and θ is the angle measured from the stagnation point. The limit of $\theta \to 0$ gives an expression for the terminal velocity obtained by Davies and Taylor (1950) and Joseph (2003),

$$u_\infty = \tfrac{2}{3}\sqrt{g a}. \tag{49}$$

Equation (49) is expected to hold for $\mathrm{Re} \gg 1$, $\mathrm{We} \gg 1$, and $\mathrm{Bo} \gg 1$ because the flow is assumed to be potential at the bubble front and the surface tension effect is considered to be negligible compared to both inertia and gravity. For a spherical cap bubble, the front curvature radius a can be related to the bubble diameter as $a = c(\mathrm{Re})d_b$ according to Clift, Grace, and Weber (1978). In fact, $c(\mathrm{Re})$ depends on the angle θ_c made by the cap that itself depends on the Reynolds number. In the limit of large Reynolds numbers, the cap angle reaches a constant value of $\theta_c \approx 50°$. Correspondingly, $c(\mathrm{Re}) = 1.14$. Therefore, the velocity can be simply related to the bubble diameter as

$$u_\infty = 0.707\sqrt{g d_b}. \tag{50}$$

Equation (50) indicates that the bubble rising velocity is again increasing with the bubble size and scales with the characteristic velocity $\sqrt{g d_b}$, which is in agreement with the trend

observed in Fig. 4 for $d_b > 10$ mm ($\vartheta_b > 524$ mm^3). As a consequence of the balance between inertia and gravity, the spherical cap bubble motion is characterized by a constant Froude number of 0.707 and a constant drag coefficient of $C_D = 8/3$.

At large Bo and for sufficiently viscous fluid, a peculiar bubble shape is observed: a thin film of gas, commonly referred to as a skirt, forms and extends downward from the rim of the spherical cap, as shown in Fig. 7. Experiments (Guthrie and Bradshaw, 1969) have indicated that the thickness of the skirt film is around 50 μm. Direct numerical simulations have been useful for investigating the flow structure, the skirt thickness and length, and the corresponding terminal velocity for such bubbles (Legendre, 2022). The rising velocity of spherical, skirt, and spherical cap bubbles can be fitted by

$$u_\infty = \sqrt{g d_b}\left[\frac{1}{(0.707)^2} + \frac{12}{\mathrm{Re}}\right]^{-1/2} \tag{51}$$

as long as the Bond number is larger than 100. In the limit of small Reynolds numbers, the Stokes terminal velocity is recovered ($u_\infty = \rho g d_b^2/12\mu$), while in the limit of large Reynolds numbers, the expression for the terminal velocity of a spherical cap is recovered [given by Eq. (50)]. Equation (51) corresponds to a drag coefficient $C_D = 8/3 + 16/\mathrm{Re}$, where the two limits, the spherical bubble and the spherical cap bubble, are readily identified.

4. Bubble rupture

When exposed to a strong shear or to an intense turbulent environment bubbles can deform under conditions favorable for breakup, as depicted in Fig. 9. Different approaches have been proposed to describe and model bubble breakup and a significant body of literature has addressed this topic over the past decades (Hinze, 1955; Risso and Fabre, 1998; Ravelet, Colin, and Risso, 2011; Vejrazka, Zednikova, and Stanovsky, 2018; Ruth *et al.*, 2022). For detailed reviews on the subject, see Risso (2000) and Ni (2024).

To understand the conditions for bubble rupture, we can first consider the previously introduced nondimensional numbers to describe bubble deformation [Eq. (39)], namely, the Bond, capillary, and Weber numbers. When a bubble is continuously submitted to an external forcing that increases its deformation, rupture may occur when it reaches a maximum deformation. A rupture criterion based on limit values for Bo, Ca, and We can then be proposed. In particular, considering rising bubbles in stagnant liquids the critical Weber number We_C was related to the critical Bond number Bo_C by Risso (2000),

$$\mathrm{We}_C = 0.51\mathrm{Bo}_C, \qquad \mathrm{Bo}_C = 730(1 + \mathrm{Mo}^{1/4})^{1.66}, \tag{52}$$

where Mo is the Morton number. For an air bubble in water, $\mathrm{Bo}_C \approx 730$ and $\mathrm{We}_C \approx 370$ corresponding to a maximum bubble equivalent diameter $d_b \approx 7.3$ cm ($\vartheta_b \approx 203$ cm^3), shown in Fig. 4(a) as a vertical dashed blue line. In other words, a bubble larger than this critical size will fragment as it rises. The stability of the upper surface of a large gas bubble rising steadily through liquid under gravity was analyzed by Batchelor (1987).

This list of relevant dimensionless parameters for deformation and then breakup can be extended for turbulent flows. According to the Hinze-Kolmogorov theory (Hinze, 1955), the size of turbulent eddies that will induce large bubble deformation are those comparable to bubble size. The bubble deformation is thus induced by the dynamic pressure difference between two points separated by a bubble diameter, which can be expressed as the difference in the velocity fluctuations u' as $\delta u^2(d_b, x, t) = \|u'(x + d_b, t) - u'(x, t)\|^2$, as depicted in Fig. 9(c). From a Lagrangian point of view, we can consider $\rho\overline{\delta u^2(d_b)}$ as the average turbulent pressure along

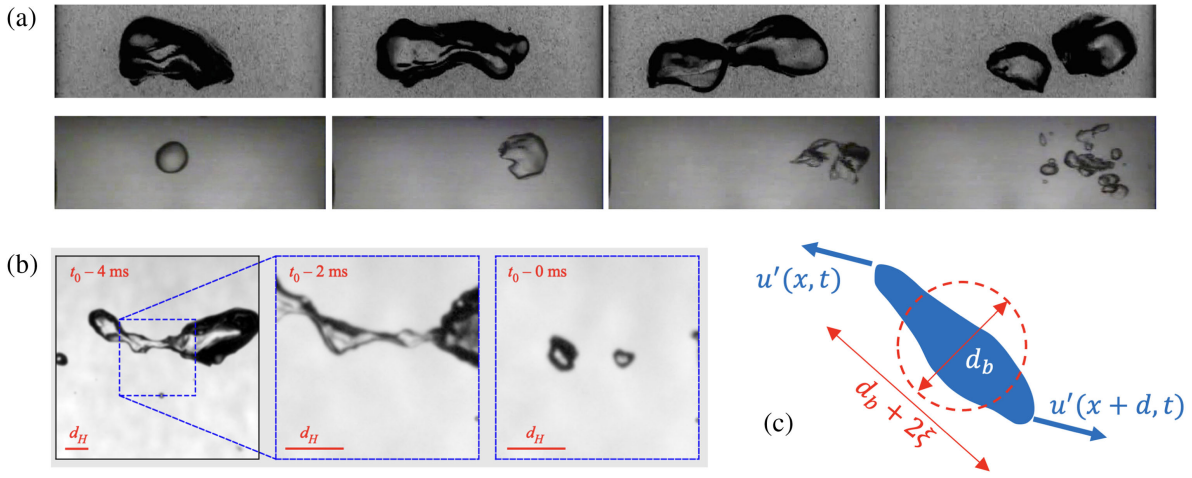

FIG. 9. Evolution of bubble shape up to rupture in a turbulent flow. (a) Shape evolution supporting the two approaches discussed in the text for the bubble rupture scenario. From Risso and Fabre, 1998. Top row: the bubble is continuously deformed up to breakup into two daughter bubbles. Second row: the bubble is subject to turbulent fluctuations and finally breaks into multiple daughter bubbles. (b) Formation of a gas ligament prior to rupture resulting in the formation of small bubbles, with d_H the Hinze scale. From Ruth *et al.*, 2022. (c) Schematic of the scenario of bubble deformation in a turbulent field. Adapted from Lalanne, Masbernat, and Risso, 2019.

the bubble motion. We can therefore define a turbulent Weber number We_t as

$$\mathrm{We}_t = \frac{\rho \overline{\delta u^2(d_b)} d_b}{\sigma}. \tag{53}$$

Assuming that turbulence is isotropic at the bubble scale and that the bubble diameter is within the inertial turbulent subrange, $\overline{\delta u^2(d_b)}$ can be expressed in terms of the dissipation rate ϵ. In this case $\overline{(\delta u)^2} \approx 2(\epsilon d)^{2/3}$, allowing us to rewrite the turbulent Weber number as

$$\mathrm{We}_t = \frac{2\rho \epsilon^{2/3} d_b^{5/3}}{\sigma}. \tag{54}$$

The bubble is thus expected to break if We_t exceeds a critical Weber number We_{tC} corresponding to a bubble size larger than the Hinze scale,

$$d_H = \mathrm{We}_{tC}^{3/5} \left(\frac{\sigma}{2\rho\epsilon^{2/3}}\right)^{3/5}. \tag{55}$$

Experimental and numerical investigations indicate that $\mathrm{We}_{tC} = \mathrm{O}(1)$ (Vejrazka, Zednikova, and Stanovsky, 2018; Ruth *et al.*, 2022). For bubbles with initial sizes much larger than d_H, the size distribution of bubbles smaller than d_H after breakup follows $N(d_b) \propto d_b^{-3/2}$ with the formation of extremely small bubbles, as shown in Fig. 9(b), resulting from the capillary instability of ligaments formed when the bubble elongates (Ruth *et al.*, 2022).

Additionally, to complete our assessment of rupture, the bubble can be considered as an oscillator. This concept originated by considering a resonance mechanism between the bubble deformation and the turbulent fluctuations (Sevik and Park, 1973). Balancing the second mode of oscillation $\omega_2 = 2\pi f_2 = \sqrt{96\sigma/\rho d_b^3}$ with the turbulence frequency at the bubble scale $\approx 2\sqrt{\overline{\delta u^2(d_b)}}/d$, the turbulent Weber number We_t defined in Eq. (53) is recovered. The criterion for breakup is $\mathrm{We}_t \approx 6/\pi^2 = \mathrm{O}(1)$, which is consistent with experimental observations. This concept can be extended by considering a linear oscillator (see Sec. V.C.3, where such a dynamical system is considered for modeling bubble rebound) where the mass of the oscillator is the added mass of the liquid, the stiffness is the surface tension, the dissipation arises from the liquid viscosity, and the external forcing is imposed by the instantaneous local turbulent fluctuations (Lalanne, Masbernat, and Risso, 2019; Ni, 2024). A bubble oscillator equation can then be written to describe the amplitude of bubble oscillation $\xi(t)$ [as depicted in Fig. 9(c)] as

$$\frac{d^2\xi}{dt^2} + 2D_2\frac{d\xi}{dt} + \omega_2^2\xi = K\frac{\delta u^2(d_b,t)}{d}, \tag{56}$$

where ω_2 is close to the eigenfrequency $\sqrt{96\sigma/\rho d^3}$ and D_2 is related to the damping rate $80\nu/d_b^2$ of mode 2 of the deformation of the bubble (Risso and Fabre, 1998; Riviére, Abahri, and Perrard, 2024). The oscillation period and the characteristic time of damping are then $2\pi/\omega_2$ and $1/D_2$, respectively. The equation for the normalized deformation $\xi^* = \xi/d$ with the normalized time $t^* = t\omega_2$ indicates that the turbulent forcing is controlled by the turbulent Weber number [Eq. (53)],

$$\frac{d^2\xi^*}{dt^{*2}} + 2\frac{D_2}{\omega_2}\frac{d\xi^*}{dt^*} + \xi^* = K\frac{\mathrm{We}_t}{\mathrm{We}_2}, \tag{57}$$

where $\mathrm{We}_2 = \rho\omega_2^2 d_b^3/\sigma$ is a characteristic Weber number of the free bubble mode 2 oscillation. A critical deformation $\xi_C^* = 2.5K/\mathrm{We}_2$ is used for the breakup criteria (Lalanne, Masbernat, and Risso, 2019), while Riviére and Perrard (2024) considered $\xi_C^* = 0.37$.

D. Bubble surface contamination

The effect of surfactants on the rise of a spherical bubble is illustrated through the experiments with a rising bubble in water conducted with different types and amounts of surfactant (Takagi, Ogasawara, and Matsumoto, 2008) that are shown in Fig. 10(b) for ultrapurified water, tap water, water with three concentrations of pentanol (21, 63, and 168 ppm), and water with 2 ppm of Triton X-100. The bubbles are shown at the same time after entering the window of observation. As shown in the figure, the distance traveled during a given time varies significantly depending on the type of surfactant and also their concentration. The strongest effect is observed for Triton X-100, which has a long molecule chain. The distance traveled is 2.5 times less than the distance traveled by the bubble in a purified system. The corresponding velocity is thus 2.5 smaller, revealing a larger drag force for a bubble in a highly contaminated situation.

If one considers a liquid with a surfactant, as the bubble rises, these molecules accumulate at the bubble surface. The evolution of the surfactant concentration at the bubble interface Γ_I is modeled by the surface advection-diffusion equation (Levich, 1962; Stone, 1990; Cuenot, Magnaudet, and Spennato, 1997),

$$\frac{\partial \Gamma_I}{\partial t} = -\boldsymbol{\nabla}_I.(u_I\Gamma_I) + D_\Gamma \boldsymbol{\nabla}_I^2\Gamma_I + S_\Gamma, \tag{58}$$

where $\boldsymbol{\nabla}_I$ is the surface gradient operator, D_Γ is the surface diffusion coefficient, u_I is the surface velocity, and $S_\Gamma = k_a C_I(\Gamma_\infty - \Gamma_I) - k_d\Gamma_I$ is the flux of surfactants from the liquid phase to the interface, with C_I the surfactant concentration in the liquid in contact with the interface, Γ_∞ the saturation value of Γ, and k_a and k_d the coefficients of the adsorption and desorption kinetics, respectively. The two first terms on the right-hand side of Eq. (58), namely, the interface advection and diffusion, control the surfactant distribution at the interface. The relative importance of convective to diffusive transport of surfactants is characterized by an interfacial Péclet number $\mathrm{Pe}_I = d_b u_b/D_\Gamma$. Usually, $\mathrm{Pe}_I \gg 1$, so surfactants accumulate at the rear of the bubble, transported by the interfacial velocity to form a cap, as illustrated in Fig. 10(a).

In fact, four typical situations can be expected depending on the values of the different parameters governing the problem

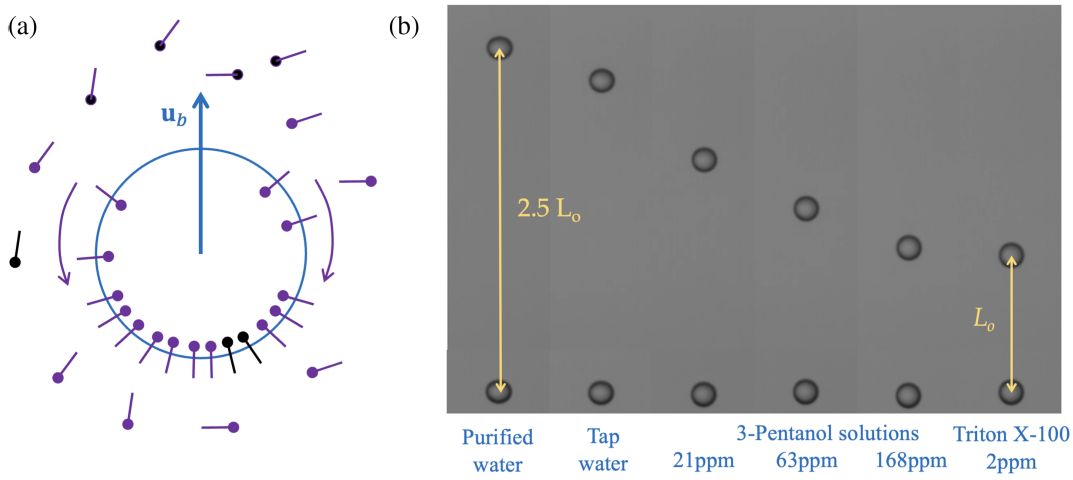

FIG. 10. (a) Schematic illustration of bubble interface contaminated by surfactants that accumulate in the rear part of the bubble. (b) An air bubble with $d_b = 0.9$ mm rising in water with different surfactants. The images are shown at the same time after the bubble appears in the observation window. From left to right: ultrapurified water, tap water, three solutions of pentanol, and Triton X-100. Adapted from Takagi *et al.*, 2009.

(Cuenot, Magnaudet, and Spennato, 1997): (i) the unretarded velocity profile (no effect of surfactant on the slip velocity at the bubble surface), (ii) the uniformly retarded profile (the slip velocity at the bubble surface is uniformly reduced), (iii) the stagnant-cap model (the front part of the bubble is not impacted by the surfactant, while the rear part of the bubble is immobilized because of surfactant accumulation), and (iv) the completely stagnant model (the interface is entirely saturated in surfactant, resulting in the nonslip condition).

The stagnant-cap case occurs for cases involving a large interfacial Péclet number Pe_I and small values of $\alpha_\Gamma = k_a C_\infty d/U_b$ and $\alpha_\Gamma/\mathrm{La} = k_d d/U_b$, where $\mathrm{La} = k_a C_\infty/k_d$ is the Langmuir number and C_∞ is the bulk concentration of the surfactant. Under these conditions and at equilibrium, Eq. (58) simplifies to $\boldsymbol{\nabla}_I \cdot (u_I \Gamma_I) \approx 0$. Combined with a zero flux boundary condition at the stagnation points, we have $u_I \Gamma_I \approx 0$. On the "clean part" of the surface, this condition is satisfied because $\Gamma_I \approx 0$; thus, the external fluid can slip on the surface. Conversely, on the contaminated part, the condition $u_I \Gamma_I \approx 0$ can be satisfied only if $u_I = 0$, which results in a no-slip condition.

The motion of the liquid at the bubble interface is also related to the viscous shear condition given by Eq. (9), where the effect of the gas has been neglected,

$$\mathbf{n}_b \cdot \boldsymbol{\Sigma} \cdot (\mathbf{I} - \mathbf{n}_b \mathbf{n}_b) = \boldsymbol{\nabla}_I \sigma. \tag{59}$$

In Eq. (59) the surface tension σ depends on the local surfactant concentration Γ_I. $\sigma(\Gamma_I)$ is usually determined by considering the Langmuir adsorption isotherm (Levich, 1962),

$$\sigma(\Gamma_I) = \max\left\{\sigma_\infty, \sigma_0\left[1 + \frac{\Re T \Gamma_\infty}{\sigma_0} \ln\left(1 - \frac{\Gamma_I}{\Gamma_\infty}\right)\right]\right\}, \tag{60}$$

where $\Re$ is the ideal gas constant, T is the absolute temperature, and σ_∞ is the surface tension value that corresponds to the maximum concentration of surfactants Γ_∞ at the interface (Olgac and Muradoglu, 2013). The dynamic surface tension measurements of various air-liquid interfaces with nonionic surfactants (Triton X-100 or $C_{12}E_6$) have values ranging from $\sigma_\infty/\sigma_0 \approx 0.2$ to $\sigma_\infty/\sigma_0 \approx 0.6$, for different surfactant concentrations (Giribabu and Ghosh, 2007; Li and Gupta, 2019).

From Eqs. (35), (59), and (60), we can show that the bubble surface vorticity has an additional source when the interface is contaminated (Atasi *et al.*, 2023),

$$\omega_I = 2\frac{u_I}{R_c} + \frac{\mathcal{R}T\Gamma_\infty}{\mu(\Gamma_\infty - \Gamma)} \boldsymbol{\nabla}_I \Gamma_I, \tag{61}$$

where R_c is the local bubble radius of curvature. The presence of a concentration gradient $\boldsymbol{\nabla}_I \Gamma_I$ at the interface increases the interface vorticity. As discussed in Sec. III.B.4, increasing vorticity at the interface increases the drag force, and thus the terminal velocity is reduced.

This reduction in bubble speed is observed in Fig. 4, where the experimental terminal velocity of a spherical bubble is smaller than the clean bubble prediction given by Eq. (33). When the concentration of surfactant in the liquid is sufficiently high, the bubble surface mobility is reduced, resulting in the slower rising velocity shown in Fig. 10. The lower curve (dashed red line) in Fig. 4 was obtained by solving

$$6\pi\mu R(1 + 0.15\mathrm{Re}^{0.687})\mathbf{u}_b = \frac{4\pi R^3}{3}\rho\mathbf{g}, \tag{62}$$

where the term on the left-hand side is the drag force of a solid sphere (Schiller and Naumann, 1933). This reveals that the lower part of the data reported in Fig. 4 shows a highly contaminated bubble whose interface is immobilized by the presence of surfactants. In such a situation, the bubble behaves like a sphere with a no-slip surface, and the function $\mathcal{K}(\mathrm{Re})$ to consider in the drag force equation (30) is then

$$\mathcal{K}(\mathrm{Re}) = \tfrac{3}{2}(1 + 0.15\mathrm{Re}^{0.687}) \tag{63}$$

instead of Eq. (31), which is used for a clean bubble. Note that the presence of surfactant on the bubble surface also affects the bubble path instability discussed in Sec. III.C.2 (Zhang, McLaughlin, and Finch, 2001; Tagawa, Takagi, and Matsumoto, 2014; Pesci *et al.*, 2018).

IV. BUBBLE INTERACTION WITH NONUNIFORM AND UNSTEADY FLOWS: ADDED MASS AND THE LIFT EFFECT

We now consider a gas bubble moving in a more general situation consisting of an unsteady nonuniform flow noted as $\mathbf{U}(\mathbf{x}, t)$, instead of a stagnant fluid, as schematically shown in Fig. 11.

A. The generalized Archimedes force and added mass effects

We first consider a control volume ϑ_L in the liquid with surface S_L and normal vector $\mathbf{n}_L$ directed out of ϑ_L [see Fig. 11(b)] to calculate the force $\mathbf{F}_{L\,\mathrm{to}\,L}$ applied by the external liquid on this volume of fluid ϑ_L corresponding to the last term in the trajectory equation (1),

$$\mathbf{F}_{L\,\mathrm{to}\,L} = \int_{S_L} \mathbf{T}\cdot\mathbf{n}_L dS = \int_{\vartheta_L} \mathrm{div}(\mathbf{T}) d\vartheta. \tag{64}$$

Since the velocity and pressure fields of the fluid are defined inside ϑ_L, the integral in Eq. (64) can be transformed into a volume integral. The velocity field $\mathbf{U}(\mathbf{x}, t)$ satisfies the Navier-Stokes equations such that $\mathrm{div}(\mathbf{T}) = \rho(-\mathbf{g} + \partial\mathbf{U}/\partial t + \mathbf{U}\cdot\boldsymbol{\nabla}\mathbf{U})$, so the force can be written as

$$\mathbf{F}_{L\,\mathrm{to}\,L} = \int_{\vartheta_L} \rho\left(-\mathbf{g} + \frac{\partial\mathbf{U}}{\partial t} + \mathbf{U}\cdot\boldsymbol{\nabla}\mathbf{U}\right) d\vartheta. \tag{65}$$

Using a Taylor series expansion of the first two terms with respect to the position of center of the control volume $\mathbf{x}_L$ and retaining only the first term leads to

$$\mathbf{F}_{L\,\mathrm{to}\,L} = -\rho\vartheta_L\mathbf{g} + \rho\vartheta_L\left(\frac{\partial\mathbf{U}}{\partial t} + \mathbf{U}\cdot\boldsymbol{\nabla}\mathbf{U}\right)_{\mathbf{x}_L}. \tag{66}$$

The first term in Eq. (66) is the Archimedes force that results from the hydrostatic pressure in the fluid. The two other terms in Eq. (66) give an extended interpretation of this force for the case when the flow is unsteady and nonuniform, as discussed by Batchelor (1967). The second term results from the time acceleration of the fluid, while the last one is induced by the convective fluid acceleration. Typically, this contribution can be observed in a convergent (divergent) flow induced, for example, by the reduction (increase) of the container cross section; see Fig. 11(c). For example, considering that the velocity component U_x increases (decreases) in the flow direction denoted by e_x, a term of the form $U_x\partial U_x/\partial x$ expresses the acceleration (deceleration) of the fluid particles. In summary, three types of acceleration can act on the liquid volume ϑ_L: gravity and the temporal and convective accelerations of the flow.

Consider now an object, such as a bubble of constant volume $\vartheta_b = \vartheta_L$, in the same location ($\mathbf{x}_b = \mathbf{x}_L$) as ϑ_L and moving at velocity $\mathbf{u}_b$; see Fig. 11(a). This object experiences the same forces, but a correction is needed because the object

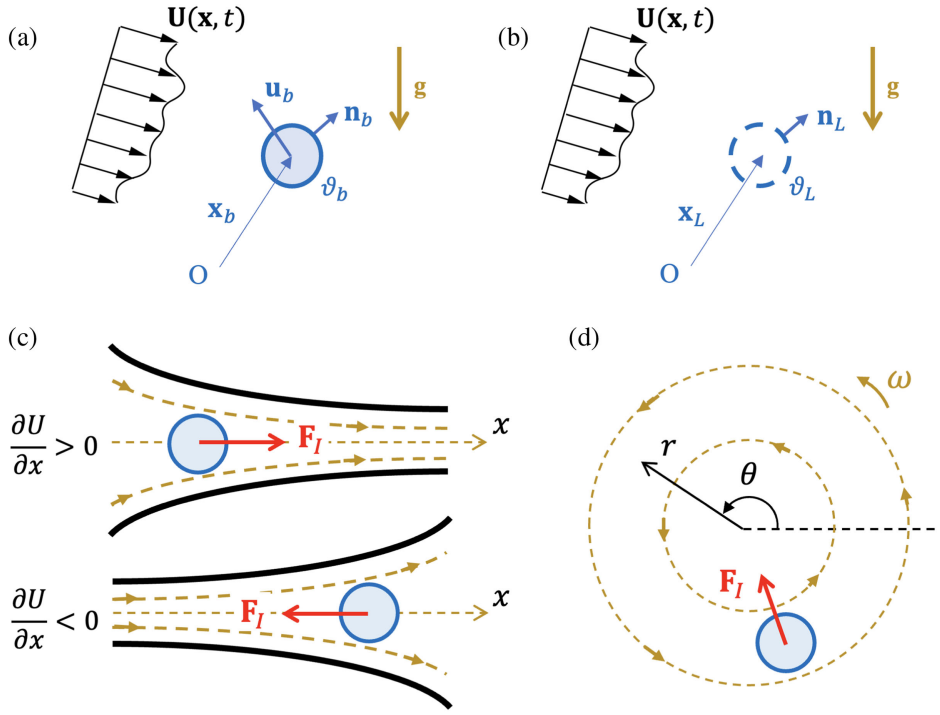

FIG. 11. (a) A bubble of volume ϑ_b moving in an unsteady nonuniform flow denoted by $\mathbf{U}(\mathbf{x}, t)$. (b) Definition of a volume of fluid having the same volume as the bubble $\vartheta_L = \vartheta_b$ located at the position $\mathbf{x}_L = \mathbf{x}_b$ in the same flow field. (c) Inertial force $\mathbf{F}_I$ applied to a bubble in a convergent channel $\partial U/\partial x > 0$ and in a divergent channel $\partial U/\partial x < 0$ flow along the x direction. (d) Inertial force $\mathbf{F}_I$ applied to a bubble in a solid rotation flow $\mathbf{U} = \omega r\mathbf{e}_\theta$.

surface is now impermeable, which modifies the fluid displacement around the bubble. According to Auton, Hunt, and Prud'Homme (1988) [see also Magnaudet and Eames (2000) for a detailed discussion], the correction is simply the multiplication of the last two terms in Eq. (66) by $(1+C_M)$, where C_M is the added mass coefficient, which is $C_M = 1/2$ for a spherical shape. When the bubble deforms or interacts with other bubbles and/or a wall, C_M increases (van Wijngaarden, 1976). Subtracting the buoyancy force $\rho \mathbf{g} \vartheta_b$, the resulting force then is written as

$$\mathbf{F}_I = \rho \vartheta_b (1+C_M) \left(\frac{\partial \mathbf{U}}{\partial t} + \mathbf{U} \cdot \boldsymbol{\nabla} \mathbf{U} \right)_{\mathbf{x}_b} - C_M \rho \vartheta_b \frac{d\mathbf{u}_b}{dt}. \quad (67)$$

As discussed, the first term of Eq. (67) represents the effect of the time acceleration of the surrounding liquid motion on the bubble; the second term represents spatial changes of the velocity field, which can be relevant to convergent and divergent flows, as well as in rotating flows. When we first consider the convergent (divergent) flow shown in Fig. 11(c), the velocity component U_x increases (decreases) in the flow direction denoted by $\mathbf{e}_x$, and a term of the form $U_x \partial U_x/\partial x$ expresses the acceleration (deceleration) of the fluid particles. It results in an inertial force transmitted to the bubble along the $\mathbf{e}_x$ direction of the form $\mathbf{F}_I \cdot \mathbf{e}_x = \rho \vartheta_b (1+C_M) U_x \partial U_x/\partial x$. Another example where the spatial contribution $\mathbf{U} \cdot \boldsymbol{\nabla} \mathbf{U}$ in $\mathbf{F}_I$ is of great importance is the vortex bubble capture mechanism. Consider the image in Fig. 11(d), where the solid body rotation $\mathbf{U} = \omega r \mathbf{e}_\theta$ is expressed in cylindrical coordinates (r, θ, z). The contribution $\mathbf{U} \cdot \boldsymbol{\nabla} \mathbf{U} = -r\omega^2 \mathbf{e}_r$ induces a centripetal force $\mathbf{F}_I = -r\rho \vartheta_b (1+C_M) \omega^2 \mathbf{e}_r$, resulting in bubble trapping by the vortex structures (van Nierop *et al.*, 2007; Rastello, Marié, and Lance, 2011).

When the flow cannot be considered uniform at the bubble scale, Eq. (66) needs to be corrected by the Faxén correction that accounts for the curvature of the surrounding flow $(\boldsymbol{\nabla}^2 U)_{\mathbf{x}_b}$ at the bubble location (Gatignol, 1983; Homann and Bec, 2010).

The additional term involving the bubble acceleration in Eq. (67) (the last term on the right-hand side) has an important impact on the bubble motion. To clarify its contribution, we come back to the bubble trajectory given by Eq. (1), where the term $\int_{S_b} \mathbf{T} \cdot \mathbf{n}_b dS$ has been split into two parts in order to combine the last term of Eq. (67) with the bubble acceleration

$$(\rho_b + C_M \rho) \vartheta_b \frac{d\mathbf{u}_b}{dt} = (\rho_b - \rho) \vartheta_b \mathbf{g} + \sum \text{other forces from the fluid}. \quad (68)$$

Equation (68) shows that the bubble acceleration involves its own mass but also has an additional mass corresponding to the liquid volume $(C_M \vartheta_b)$. The corresponding contribution is called the added mass force, which is associated with the added mass coefficient C_M. For bubbles this term is much larger than the bubble's own mass ($\rho_b \ll C_M \rho$). It is, therefore, crucial for it to be considered when describing the bubble dynamics. Similarly, the bubble weight in Eq. (68) is small compared to the Archimedes force since $\rho_b \ll \rho$.

B. Shear-induced lift force

Here, the *lift effect* refers to the force experienced by a bubble in a direction perpendicular to the relative motion of the fluid with respect to the moving bubble $\mathbf{U} - \mathbf{u}_b$. Observed lift effects can result from different causes. For airplanes the lift force that supports the airplane weight is generated by the flow circulation induced by the wing shape. The spinning lift, or Magnus effect, is induced by the rotation of the object, which is relevant in sports. Bubbles can also experience lift effects when rising in a quiescent fluid due to their wake structure when their shape is ellipsoidal, as shown in Fig. 7. Bubbles can also experience a lift effect, even when spherical, if they traverse a nonuniform flow. In such a situation, the lift force results from a nonaxisymmetric distribution of both the pressure and the normal viscous stress on the bubble interface. This force is responsible for the migration of bubbles in vertical pipes and determines the radial distribution of the gas volume fraction (Colin, Fabre, and Kamp, 2012). As later outlined, for bubbles this lift effect depends on the Reynolds number and the bubble shape. For our discussion we consider only unbounded linear shear flows. For details regarding wall-bounded linear shear flow effects, see Shi *et al.* (2020) and references therein.

The lift force has mostly been characterized by considering a steady linear shear flow, as shown in Fig. 12(a). The experiments from Tomiyama *et al.* (2002) provide a clear idea of the lift force effect. Bubbles of different sizes were injected into a linear shear flow generated by a belt moving at a constant speed, as illustrated in Fig. 12(b). The flow velocity field is $\mathbf{U} = (U_o + \alpha y') \mathbf{e}_{x'}$ in the frame of reference moving with the bubble. Two bubble sizes are shown here, $d_b = 2.84$ and 5.54 mm, corresponding to a nearly spherical and an ellipsoidal bubble, respectively. As shown in Fig. 12(c), both bubbles deviate in the horizontal direction when rising, thereby revealing a lift effect. However, the two bubbles migrate in opposite directions.

The induced lift force is usually expressed in the form (Žun, 1980; Auton, 1987)

$$\mathbf{F}_L = C_L \rho \vartheta_b (\mathbf{U} - \mathbf{u}_b) \times \boldsymbol{\Omega}, \quad (69)$$

where C_L is the lift coefficient and $\boldsymbol{\Omega} = \boldsymbol{\nabla} \times \mathbf{U}$ is the vorticity field at the bubble location. Based on Eq. (69), C_L is positive (negative) for the spherical (ellipsoidal) bubble shown in Fig. 12(c) [Fig. 12(d)]. The lift coefficient for a spherical and clean bubble is reported as a function of the bubble Reynolds number for different shear rates $\mathrm{Sr} = \alpha d_b / U_o$ in Fig. 12(f). The lift coefficient is positive for all Reynolds numbers and shear rates, so spherical bubbles are always expected to migrate following the case reported in Fig. 12(c). A constant value of

$$C_L = 0.5$$

was derived by Auton (1987), who considered a weak inviscid linear shear flow applicable for $\mathrm{Re} \gg 1$ and $\mathrm{Sr} \ll 1$. The trend shown in Fig. 12(f) for $\mathrm{Re} > 100$, where $C_L \approx 0.5$ confirms that the term $\rho \vartheta_b (\mathbf{U} - \mathbf{u}_b) \times \boldsymbol{\Omega}$ is relevant for describing lift effects at large Reynolds numbers. For the case depicted in

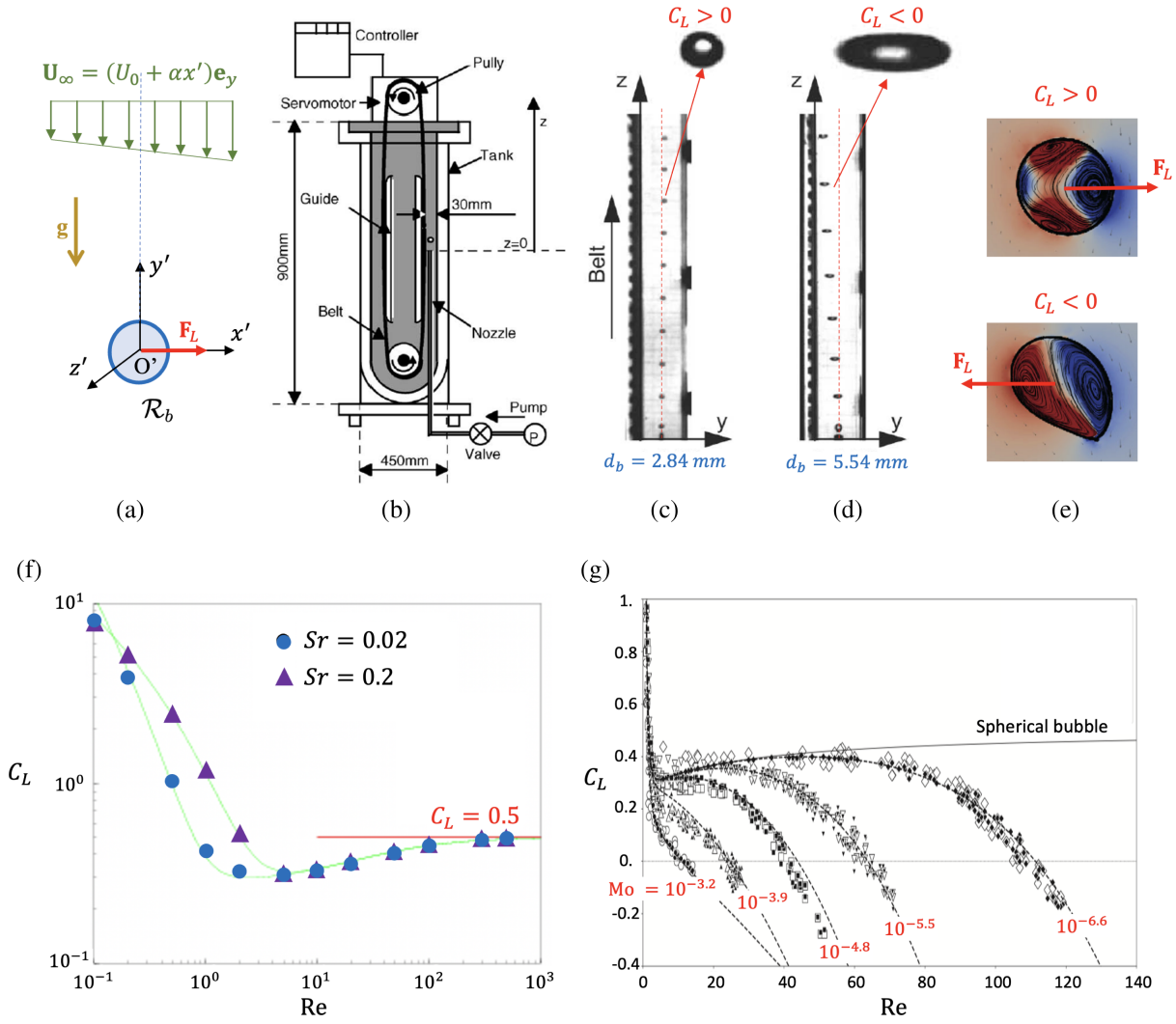

FIG. 12. Rising bubble in a vertical linear shear flow showing horizontal migration. (a) Problem statement in the frame of reference $\mathcal{R}_b$ moving with the bubble corresponding to the experimental setup shown in (b). (b) Experimental apparatus using a belt to generate the vertical linear shear flow in a glycerol-water solution with Mo $= 10^{-5.3}$ (Tomiyama *et al.*, 2002). (c) Bubble experiencing a positive lift force ($d_b = 2.84$ mm). (d) Bubble experiencing a negative lift force ($d_b = 5.54$ mm). (e) Numerical simulation at a low Reynolds number (Ga $= 18$) for a small deformation (top image, Bo $= 0.4$) and significant deformation (bottom image, Bo $= 20$). (f) Evolution of the lift coefficient of a fixed spherical bubble in a linear shear flow obtained from a numerical simulation (Legendre and Magnaudet, 1998). (g) Lift coefficient of a deformable bubble rising in a linear shear flow in a setup similar to that shown in (b) (Hayashi, Legendre, and Tomiyama, 2020).

Fig. 12(a), $\mathbf{\Omega} = -\alpha\mathbf{e}_{z'}$. Under such conditions, the lift force is $\mathbf{F}_L = (\pi/12)\rho d_b^3 U_o \alpha \mathbf{e}_{y'}$.

For Re $\ll 1$ the lift force experienced by a bubble was calculated by Legendre and Magnaudet (1997), who extended the work of Saffman (1965) and McLaughlin (1991), both of whom considered a solid sphere. The lift force follows a different behavior from the large Re case showing that $\mathbf{F}_L = (1/\pi)\sqrt{\rho\mu\alpha}d^2 U_o J(\epsilon)\mathbf{e}_{y'}$, which corresponds to a lift coefficient

$$C_L = \frac{6}{\pi^2}\sqrt{\mathrm{Re}\,\mathrm{Sr}}J(\epsilon), \tag{70}$$

where $\epsilon = \sqrt{\mathrm{Sr}/\mathrm{Re}}$ and $J(\epsilon)$ is a function numerically calculated by McLaughlin (1991) that can accurately be approximated by $J(\epsilon) = 2.255/(1 + 0.2/\epsilon^2)^{3/2}$ (Legendre and Magnaudet, 1998). Equation (70) is valid for Re $\ll 1$ and $\sqrt{\mathrm{Re}\,\mathrm{Sr}} \ll 1$.

Expressions for the lift coefficient that we use in the forthcoming description of bubble motion in nonuniform flow were given by Legendre and Magnaudet (1998) for spherical clean bubbles and by Hayashi, Legendre, and Tomiyama (2020) and Hayashi *et al.* (2021) for deformed bubbles. Numerical simulations considering a stagnant-cap model for the contamination of spherical bubbles report a monotonic decrease of the bubble lift coefficient with the increase of the contamination (Takagi, Ogasawara, and Matsumoto, 2008; Takagi and Matsumoto, 2011). Experiments of ellipsoidal bubbles rising in water in a shear flow (generated at the side of a bubble column) with different amounts of

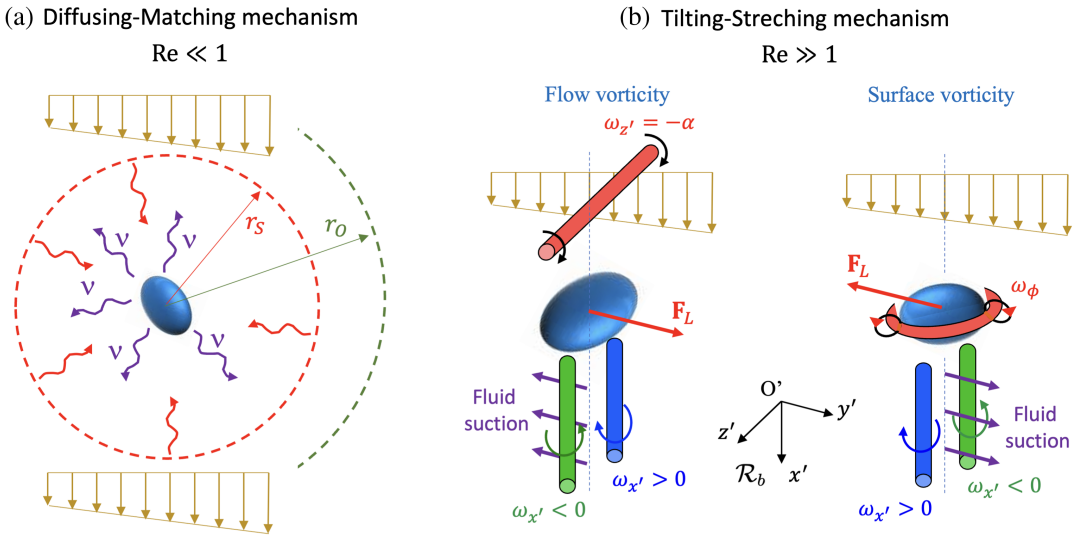

FIG. 13. Illustration of lift force mechanisms resulting in positive or negative lift effect depending on the interaction of the interfacial vorticity with the shear flow. (a) Diffusing-matching mechanism (or Saffman mechanism) showing the Oseen radius $r_O = O(d_b/\mathrm{Re})$ and the Saffman radius $r_S = d_b/\sqrt{\mathrm{Re}\,\mathrm{Sr}}$ for $\epsilon = \sqrt{\mathrm{Sr}/\mathrm{Re}} > 1$. (b) The tilting-stretching mechanism (Adoua, Legendre, and Magnaudet, 2009) applied to the vorticity field of the flow $\omega_{z'} = -\alpha$ (the Lightill L mechanism) resulting in a positive lift contribution (left sketch) and applied to the vorticity ω_ϕ generated at the bubble surface (the surface S mechanism), resulting in a negative lift contribution (right sketch).

1-pentanol and Triton X-100 solutions confirm a strong dependency of the lift coefficient with surface contamination (Hessenkemper *et al.*, 2021). However, the experiments also reveal that the lift coefficient can be increased in some particular conditions of surfactant concentration and bubble deformation. In the same setup but with saline aqueous solutions of NaCl, the lift coefficient dependency on the bubble Reynolds number is found to be only weakly affected by the salt concentration (Hessenkemper, Ziegenhein, and Lucas, 2020). This indicates that the combined effect of surfactants, electrolytes, and deformation requires further careful analysis for the particular case of the lift force.

The induced vorticity mechanisms play a key role in the production of lift; they are discussed later in regard to the vorticity field $\boldsymbol{\omega} = \boldsymbol{\nabla} \times \mathbf{u}$.

1. Lift effect at large Reynolds numbers: The tilting-stretching mechanism

The process of tilting and stretching of the incident vorticity around a sphere was described by Lighthill (1956), and Auton (1987) calculated the corresponding lift force in an inviscid weak linear shear flow. These calculations have been confirmed by numerical simulation (Legendre and Magnaudet, 1998; Adoua, Legendre, and Magnaudet, 2009; Hidman *et al.*, 2022). For the case depicted in Fig. 12(a), the incident flow vorticity component $\omega_{z'} = -\alpha$ is tilted and stretched when it passes the bubble, resulting in a streamwise vorticity field $\omega_{x'}$ characterized by two intense vorticity tubes rotating in opposite directions in the bubble wake. This induces suction of the fluid between the two tubes in the negative y' direction, inducing a reaction on the bubble in the positive y' direction, as illustrated in Fig. 13(b).

However, the production of vorticity at the bubble surface at large Reynolds numbers reduces the effect of the previously described inviscid tilting-stretching mechanism. As first explained by Adoua, Legendre, and Magnaudet (2009), the vorticity produced at the bubble surface is mainly azimuthal, ω_ϕ, and is also tilted in the wake by the velocity gradient, as depicted in Fig. 13(b). This process results in the production of two tubes of streamwise vorticity field $\omega_{x'}$, which induce suction (between the two tubes) in the positive y' direction and a reaction on the bubble in the negative y' direction.

For spherical and clean bubbles, the surface vorticity contribution is not strong enough to counterbalance the tilting-stretching mechanism of the incident flow vorticity component $\omega_{z'} = -\alpha$; therefore, the lift coefficient remains positive for all Reynolds numbers. Thanks to numerical simulations (Legendre and Magnaudet, 1998), the lift force has been obtained for a viscous case with relatively large Reynolds numbers (typically $\mathrm{Re} > 50$). In this case the correction to the inviscid value is $C_L = 0.5\text{–}6.5\mathrm{Re}^{-1}$ confirming a decrease of the lift effect as previously discussed. The lift decrease is proportional to Re^{-1}, which follows the viscous drag evolution at such Reynolds numbers, $C_D \propto \mathrm{Re}^{-1}$, related to the vorticity produced at the bubble surface, as discussed in Sec. III.B.4.

However, a lift reversal is observed in Fig. 12(d) for large bubbles (Tomiyama *et al.*, 2002), as well as for surfactant-covered bubbles (Fukuta, Takagi, and Matsumoto, 2008). Indeed, as discussed in Sec. III.D with Eq. (61), the interfacial vorticity ω_I is increased when the bubble surface is contaminated and/or deformed, and its contribution can become dominant, causing the induced lift to change direction. For a rising bubble with a rear surfactant cap, the gradient of surfactant concentration $\boldsymbol{\nabla}_I \Gamma_I$ is at maximum and positive at the cap angle, generating a significant increase in ω_I. As the bubble size increases, the bubble deforms, and the minimum for the local bubble radius of curvature R_c is located at the bubble

equator, generating a maximum for the production of ω_I. Such a change in the lift direction, as bubbles become more deformed, has been confirmed experimentally for air bubbles in different fluids, including water (Hayashi, Legendre, and Tomiyama, 2020; Hayashi *et al.*, 2021), as shown in Fig. 12(g), as well as when using direct numerical simulations (Adoua, Legendre, and Magnaudet, 2009; Hidman *et al.*, 2022).

2. Lift effect at small Reynolds numbers: The diffusing-matching mechanism

We now consider the lift mechanism at small Reynolds numbers while still considering the linear shear flow $\mathbf{U} = (U_o + \alpha y')\mathbf{e}_{x'}$. In this regime the mechanisms involved in generating the lift force are different. First, the Stokes solution around a solid sphere or a spherical bubble is not valid far from the object (as $r \to \infty$, where r is the distance from the bubble center) and needs to be matched with an outer solution where inertial effects have the same order of magnitude as the viscous terms. In the outer region, the moving object is seen as a source term of momentum (a point force) whose magnitude is described at first order by the drag force. Second, the Stokes solution for the linear shear flow around a solid sphere, a spherical droplet, or a spherical bubble produces zero lift force (Legendre and Magnaudet, 1997). It follows that the lift force originates from small but nonzero inertial effects and results from the matching of the inner solution managed by the Stokes equations with the outer solution, where inertial effects have to be considered (Saffman, 1965). The inertial term of the Navier-Stokes equation from the base flow U_o becomes comparable to the viscous term at the Oseen distance, $r = r_O = O(d_b/\mathrm{Re})$, while the shear flow term balances the viscous term at the Saffman distance $r = r_S = d_b/\sqrt{\mathrm{Re}\,\mathrm{Sr}}$; see Fig. 13(a). The ratio of the two gives the previously introduced parameter ϵ. The solution for the lift force was derived while considering that the shear term must first be balanced, resulting in the condition $\sqrt{\mathrm{Re}\,\mathrm{Sr}} \ll 1$ for the validity of Eq. (70).

The matching process of the inner solution with the outer solution requires the inner solution to be corrected with a velocity field that satisfies the Stokes equation. Thus, the lift force results from how the bubble point force is impacting the flow outside the Saffman distance. For a spherical bubble, the vorticity distribution at the bubble surface is at first order axisymetric and the point force representing the bubble in the outer region is aligned with the flow direction. However, its matching with the external flow differs because the inertial term is not axisymmetric, and the resulting feedback to the inner solution generates a positive lift force, as shown in Fig. 12. Hidman *et al.* (2022) recently reported numerical simulations of lift reversal at low bubble Reynolds numbers. In this case the bubble is deformed in a nonaxisymmetric manner (see Fig. 12), which leads to significant differences in vorticity production on the bubble surface and disrupts the fore-aft symmetry of the flow. This results in a bubble point force that is not aligned with the flow direction, thus impacting the matching of the inner solution with the outer solution and the feedback to the bubble. Consequently, depending on the bubble's deformation and orientation in the shear flow, a lift reversal may be observed.

V. BUBBLE-BUBBLE AND BUBBLE-WALL INTERACTIONS

Different types of bubble interactions can be considered. The objective here is to focus on the mechanisms that govern bubble-bubble interactions in two situations: "long-range" interactions where the interactions result from hydrodynamic mechanisms and short-range interactions where the interactions are controlled by interface deformation and lubrication.

Bubble pair interactions have been extensively investigated via careful experiments (Duineveld, 1995; Sanada, Watanabe, and Fukano, 2005; Sanada *et al.*, 2009; Kong *et al.*, 2019; Kusuno and Sanada, 2021), as well as through the use of direct numerical simulations with fixed bubbles (Legendre, Magnaudet, and Mougin, 2003; Hallez and Legendre, 2011) and free-to-move bubbles (Zhang, Hi, and Magnaudet, 2021; Zhang, Hi, and Magnaudet, 2022). These studies revealed different scenarios for interaction and the stability of bubble pairs. The pair interaction problem has many interesting aspects: in-line interactions can be stable or unstable, side-by-side bubble pairs can attract or repel, and free-to-move pairs exhibit the so-called drafting-kissing-tumbling interaction, etc. The pair interaction mechanisms are frequently used to discuss when clustering is expected to occur in bubbly flows (Zenit, Koch, and Sangani, 2001; Figueroa-Espinoza *et al.*, 2018; Ma *et al.*, 2023).

A. Side-by-side interactions

We start by considering the side-by-side interaction case, which corresponds to a bubble rising in the vicinity of another bubble of the same size and at the same speed. The separation distance between the two bubbles is L. This situation can also be used to understand bubble interactions with a wall by considering $L/2$ as the distance between the bubble and the wall, with the bubble interacting with its mirror image, which is located at the distance L. As later shown, the long-range interaction results in a change in the rising velocity in a sideways attractive or repulsive effect, as well as a possible bubble deformation (not discussed here). The interaction is different for small and large bubble Reynolds numbers. This can be anticipated by considering how a bubble displaces the fluid around it, as shown in Fig. 14.

We first consider the interaction at high bubble Reynolds numbers. As discussed, the potential flow is a good approximation for the flow around a bubble at Reynolds numbers larger than 100. As depicted in Fig. 14, the flow displacement far from the bubble is directed in the downward direction with a magnitude $-u_b R^3/(2r^3)$. At a distance $r = L$, the fluid perturbation seen with the second bubble would be $u' = -u_b R^3/(2L^3)$. Therefore, the liquid velocity in the reference frame of the second bubble is increased to $u_b[1 + R^3/(2L^3)]$, resulting in an increase in the drag force to $-12\pi\mu R u_b[1 + R^3/(2L^3)]$. Therefore, the additional drag force correction decays as L^{-3}. In the radial direction, the potential flow prediction induces a velocity gradient along the r direction that results in $-3u_b R^3/(2r^4)$. In regard to the definition of the induced shear lift [Eq. (69)], the second

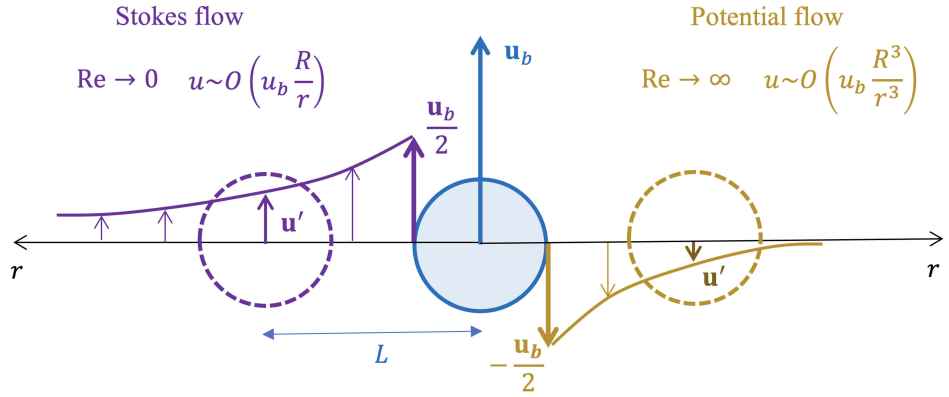

FIG. 14. Fluid displaced by a rising spherical bubble and the corresponding disturbance decay with distance r from the bubble: Stokes flow (left side) and potential flow (right side) for small and large Reynolds numbers, respectively. The flow disturbance u' is felt by the second bubble (dashed line) located at the distance $r = L$.

bubble experiences an attractive force of the form $F_a \sim \rho u_b^2 R^6/L^4$. The potential flow analytical solution of van Wijngaarden (1976) and direct numerical simulations from Legendre, Magnaudet, and Mougin (2003) both confirmed the previous discussion summarized as

$$F_D \approx -12\pi\mu R u_b\left(1-\frac{2.211}{\sqrt{\mathrm{Re}}}\right)\left[1+\frac{R^3}{L^3}\right],$$
$$F_a \approx 3\pi\rho u_b^2\frac{R^6}{L^4}\left[1+\frac{R^3}{L^3}\right]. \quad (71)$$

We now consider the limit of small Reynolds numbers where the development of the flow around the bubble is extended farther away from the bubble due to the diffusion process. The Stokes approximation remains valid up to the Oseen distance r_O. Beyond this region noninertial effects become comparable to viscous ones, and corrections must be considered. Depending on the value of L/r_O, different types of interaction will be observed, as the second bubble will be in either the inner (Stokes) or the outer (Oseen) region of the disturbance produced by the first bubble.

When two bubbles are within the Stokes region, if we consider the Stokes flow evolution as depicted in Fig. 14, the velocity disturbance induced by a bubble is now $u' = u_b R/(2L)$. The second bubble then experiences a reduction in its relative velocity with the surrounding fluid as $u_b[1-R/(2L)]$, and its drag force is reduced to $-4\pi\mu u_b[1-R/(2L)]$. The correction shows decay in L^{-1} that has a longer-range effect than that observed at high Reynolds numbers. The Stokes flow also induces a velocity gradient along the separation direction between bubbles like $u_b R/(2r^2)$ but with the opposite sign of the high Reynolds case. Hence, in this case the bubbles experience a repulsive interaction. The analytical solution for $\mathrm{Re}L/r \ll 1$ (Legendre, Magnaudet, and Mougin, 2003) confirms this scaling discussion with a corrected drag force and a repulsive force F_r of the form

$$F_D \approx -4\pi\mu R u_b\left[1-\frac{R}{2L}\right], \qquad F_r \approx \frac{1}{2}\pi\rho R^2 u_b^2. \quad (72)$$

The wall interaction shows similar trends for both small and large Reynolds numbers. In the case of a wall, the flow displacement caused by the bubble motion illustrated in Fig. 14 needs to be corrected by the nonslip condition at the wall. Near the wall some significant modifications in the force evolution, as well as in bubble deformation, are observed (Magnaudet, Takagi, and Legendre, 2003; Figueroa-Espinoza, Legendre, and Zenit, 2008; Takemura, Magnaudet, and Dimitrakopoulos, 2009). The interaction of bubbles in close contact with a wall is discussed in Sec. V.C.

B. In-line interactions

We now consider the configuration of a bubble preceding a second bubble. According to the potential solution, the in-line configuration is unstable (Harper, 1970; Hallez and Legendre, 2011). However, the study of the in-line bubble configuration reveals that either stable bubble chains or highly dispersed rising bubbles can be observed, depending on several factors, as shown in Fig. 15. The explanation for these two opposing behaviors lies in a subtle coupling between bubble deformation and surface contamination, both of which affect the wake-induced lift effect (Atasi *et al.*, 2023).

A bubble rising in the wake of another bubble experiences a reduction of its relative velocity, and therefore a reduction of its drag. It is also subject to a lift effect induced by the velocity gradient inside the wake (Hallez and Legendre, 2011), as depicted in Fig. 15(c). If $\mathbf{u}_w$ is the velocity profile in the wake of the leading bubble, the velocity experienced by the second bubble (i.e., the liquid velocity in its moving frame of reference) is then $\mathbf{u}_w - \mathbf{u}_b$. As a first approximation [see Batchelor (1967) and the appendix of Hallez and Legendre (2011), where the wake of a single bubble is detailed], the bubble wake magnitude decays as $u_w \sim u_b R/r$ such that the vorticity field experienced by the second bubble at $r = L$ is $\omega_w = \nabla \times u_w \sim u_w/R \sim u_b/L$. This effect is thus decreasing as L^{-1}, where L is the distance between the two bubble centers.

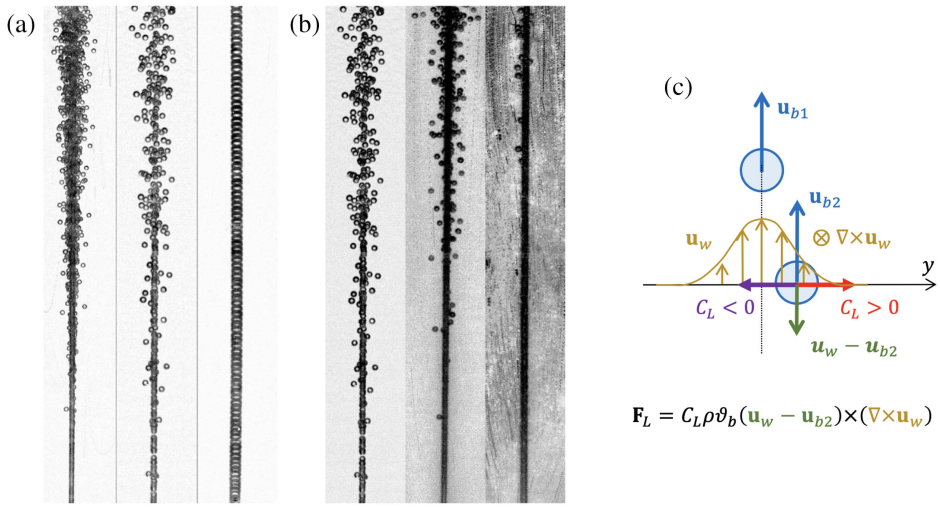

FIG. 15. (a),(b) Experiments showing the effects of bubble size and surface contamination on the stability of bubble chains. From Atasi *et al.*, 2023. (a) The bubble size increases from left to right. For a liquid without surfactants, La = 0; Ga = (1200, 1920, 8400); and Bo = (0.18, 0.25, 0.66). Values are given for the left, center, and right panels, respectively. (b) The bubble sizes are approximately the same, but the amount of surfactant increases from left to right. La = (0, 0.1, 0.5), Ga = (1920, 1200, 1800), and Bo = (0.24, 0.21, 0.32), with values given for the left, center, and right panels, respectively. (c) The wake-induced lift effect. In the wake of the first bubble, the second bubble experiences a lift force, as described in Sec. IV.B. Depending on the sign of the lift coefficient, the in-line motion is unstable ($C_L > 0$ for a spherical clean bubble) or stable ($C_L < 0$ for an ellipsoidal and/or contaminated bubble).

From Eq. (69) the lift force experienced by the second bubble in the direction perpendicular to its ascent is then

$$\mathbf{F}_L \approx C_L\rho\frac{4\pi}{3}\frac{R^3u_b^2}{L}\left(1-\frac{R}{L}\right)\mathbf{e}_y. \tag{73}$$

A negative value for the lift coefficient ($C_L < 0$; i.e., for deformed and/or contaminated bubbles), as discussed in Sec. IV.B, results in a force that retains the second bubble in the wake of the first one and in the formation of a stable bubble line, as reported in Fig. 15(a). A positive value for the lift coefficient ($C_L > 0$; i.e., for moderate bubble deformation and reduced interface contamination) induces bubble migration from the wake resulting in the formation of a cone of bubbles, as observed in Fig. 15(b). If w_b is the bubble's transverse migration velocity, the balance between the lift force [Eq. (73)] and the viscous drag $\sim\mu Rw_b$ reveals that the observed cone angle $\alpha \approx w_b/u_b$ varies linearly with the bubble detachment frequency $f = u_b/L$, as well as with the lift coefficient C_L,

$$\alpha \sim fC_L\frac{R^2\mu}{\rho}. \tag{74}$$

When C_L is reduced by increasing bubble contamination or bubble deformation, the dispersion decreases (i.e., α is decreased) as shown in Figs. 15(a) and 15(b). The validity of Eq. (74) has been confirmed by experiments involving different bubble sizes and levels of surface contamination (Atasi *et al.*, 2023).

C. Bubble dynamics in contact with a wall

We now consider the interaction of a bubble rising at its terminal velocity as it collides with an inclined wall, as illustrated in Fig. 16. This problem has recently received attention due do its importance in understanding the bubble-induced reduction of wall friction (Tanaka *et al.*, 2021) and for surface cleaning (Hooshanginejad *et al.*, 2023). Depending on the wall inclination, from $\alpha = 0^\circ$ (horizontal wall) to 90° (vertical wall) different behaviors are observed, ranging from sliding to bouncing motion (Barbosa, Legendre, and Zenit, 2016).

1. Criteria transition from sliding to bouncing regimes

The criterion between bouncing and sliding is obtained by considering the force balance for the motion normal to the wall and along the wall. We first consider the force balance in the normal direction. The sliding motion, which is shown in Fig. 16(a), is observed when buoyancy is sufficient to keep the bubble in contact with the wall. The bouncing motion, which is depicted in Fig. 16(b), occurs when the bubble can depart from the wall due to an inertial lift-type force that results from the interaction of the bubble wake with the wall; see the wake structure in Fig. 8. The induced force normal to the wall, which is denoted as $F_{w\perp}$, depends on the strength of the circulation of the vortex filaments in the wake and can be scaled as $F_{w\perp} \sim \rho d_b^2u_{bw}^2$ (de Vries, Biesheuvel, and van Wijngaarden, 2002), where u_{bw} is the bubble velocity along the wall. The force can be compared to the buoyancy acting normal to the wall, $\rho d^3g\cos\alpha$, to establish a condition for the bubble's departure from the wall,

$$\rho d_b^2u_{bw}^2 \geq \rho d_b^3g\cos\alpha. \tag{75}$$

Now we consider the motion parallel to the wall. For spherical bubbles, as shown in Fig. 16(c), the balance

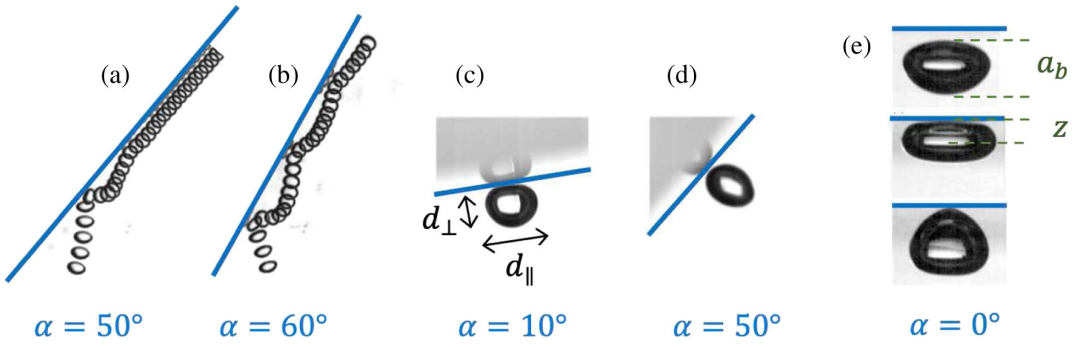

FIG. 16. Bubble interacting with a wall. A $d_b = 1.6$ mm bubble in a water-glycerin mixture is shown (a) sliding after collision and (b) bouncing repeatedly against the wall. The shape of a $d_b = 2.2$ mm air bubble in silicon oil while sliding under an inclined wall forming a lubrication film between the bubble and the wall is displayed for (c) $\alpha = 10°$ and (d) $\alpha = 50°$. (e) A $d_b = 2.62$ mm bubble rising in a water-glycerin mixture bouncing under a horizontal wall. The three instances shown are, from top to bottom, the shape at terminal velocity (before sensing the presence of the wall), the maximum deformation during impact, and the maximum rebound velocity.

parallel to the wall is obtained by the component of buoyancy along the wall $\rho d_b^3 g \sin\alpha$ and the bubble viscous drag $\sim \mu d_b u_{bw}$,

$$\mu d_b u_{bw} \sim \rho d_b^3 g \sin\alpha. \tag{76}$$

Taking the ratio of these two conditions, Eqs. (75) and (76), yields a simple criterion based on the bubble sliding Reynolds number $\mathrm{Re}_w = \rho d_b u_w/\mu$ and the wall inclination as $\mathrm{Re}_w \geq \cot\alpha$. A comparison with data from the literature (Barbosa, Legendre, and Zenit, 2016) reveals that the effective transition can be fitted to

$$\mathrm{Re}_w = \mathrm{Re}_0 + 310\cot\alpha, \tag{77}$$

where $\mathrm{Re}_0 \approx 80$ is the transition observed for a vertical wall [$\alpha = 90^\circ$ (de Vries, Biesheuvel, and van Wijngaarden, 2002; Takemura and Magnaudet, 2003)].

When bubbles are sufficiently deformed, as depicted in Fig. 16(d), the viscous drag force is replaced by an inertial drag force of the form $\rho d_b^2 u_{bw}^2$, for which the motion parallel to the wall now satisfies

$$\rho d_b^3 g \sin\alpha \sim \rho d_b^2 u_{bw}^2. \tag{78}$$

When combined with Eq. (75), the condition becomes $\cot\alpha \sim$ const, resulting in a fixed angle for the transition that is independent of the bubble sliding Reynolds number. In regard to the experiments of Barbosa, Legendre, and Zenit (2016), the criteria is given by $\cot\alpha \approx 1$. The transition between viscous and inertial motion is observed at a threshold sliding Weber number given by $\mathrm{We}_w = \rho d_b u_w^2/\sigma \approx 1.2$, which is based on the bubble-wall velocity. The transition between the sliding and bouncing regimes for a bubble rising under a wall can be summarized as follows:

$$\mathrm{We}_w \leq 1.2, \quad \mathrm{Re}_w = \mathrm{Re}_0 + 310\cot\alpha, \quad \mathrm{We}_w \geq 1.2, \quad \cot\alpha \approx 1. \tag{79}$$

2. Bubble deformation when sliding under a plane wall

When sliding under a wall, the bubble deformation changes depending on the wall inclination, as observed in Figs. 16(c) and 16(d). For small inclination angles, as shown in Fig. 16(c), buoyancy pushes the bubble against the wall and controls the bubble deformation. In this condition the bubble deformation is determined by balancing the potential energy used for deformation with the gain in surface energy (Madavan, Deutsch, and Merkle, 1985; Barbosa, Legendre, and Zenit, 2019), resulting in deformation controlled by Bo. For large inclination angle, as shown in Fig. 16(d), the bubble is flattened along the sliding direction due to inertial effects generated by its motion, resulting in a deformation controlled by the bubble sliding Weber number We_w, similar to what is observed for rising bubbles (Moore, 1965); see Sec. III.C.1. Both of these modes of deformation contribute to the overall bubble deformation and can be combined to express the bubble-wall aspect ratio $\chi_w = d_\parallel/d_\perp$, where $d_\parallel$ and $d_\perp$, as depicted in Fig. 16(c), represent the bubble's length parallel and normal to the wall, respectively (Barbosa, Legendre, and Zenit, 2019),

$$\chi_w = \frac{1 - \beta_1 \mathrm{We}_w}{(1 + \beta_1 \mathrm{We}_w/2)(1 - \beta_2 \mathrm{Bo}\,\cos\alpha)}, \tag{80}$$

with $\beta_1 = 3/32$ and $\beta_2 = 0.1$.

3. Bubble bouncing under a horizontal wall

The process of bubble deformation during bouncing under an horizontal wall is shown in Fig. 16(e). The kinetic energy of a bubble moving at its terminal velocity u_b (contained in its fluid added mass) is transformed into surface energy when the bubble is compressed against the wall. Then this surface energy is restored into kinetic energy in the direction opposite to the wall. A restitution coefficient can be defined as

$$\epsilon = \frac{u_r}{u_b}, \tag{81}$$

where u_r is the maximum velocity at restitution. The evolution of the bubble shape during the bouncing process can be described using a mass-spring model; see also Sec. III.C.4, which considers a similar dynamical system for modeling bubble deformation and breakup in a turbulent environment. It is derived considering the motion of the bubble center $z = a_b/2 - \zeta$, where a_b is the vertical axis of the bubble before the impact (its radius when spherical) and $\zeta(t)$ is the vertical deformation during the rebound. The inertia (added mass) involved in the motion of the bubble's center of mass $\sim\rho d_b^3\ddot{z}$ varies due to two main effects: (1) the damping force induced by the liquid drained between the bubble and the wall $-\mu d_b\dot{z}$ and (2) the restoring force to sphericity $\sim\sigma\zeta$ due to bubble deformation. The bubble deformation ζ can be described via the following second-order equation (Zenit and Legendre, 2009):

$$\frac{d^2\zeta}{dt^2} + K_1\frac{\mu}{\rho d_b^2}\frac{d\zeta}{dt} + K_2\frac{\sigma}{\rho d_b^3}\zeta = 0, \tag{82}$$

where K_1 depends mostly on the bubble surface mobility and K_2 on the initial bubble shape. Equation (82) reveals that this problem has two characteristic times: (1) the viscous relaxation time $\tau = \rho d_b^2/\mu$ that controls the damping effect and (2) the period of the oscillation $T = \sqrt{\rho d_b^3/\sigma}$ that controls the rebound duration. The velocity at the end of the semiperiod $t = T/2$, which corresponds to the departure of the bubble from the wall, can be expressed as a function of the velocity at impact. This allows the restitution coefficient to be determined as (Zenit and Legendre, 2009)

$$\epsilon = \frac{u_r}{u_b} \approx \exp(-K\mathrm{Oh}), \tag{83}$$

where $K \sim K_1/\sqrt{K_2}$ is a constant that can be determined from experiments and Oh is the Ohnesorge number defined in Eq. (23). The restitution coefficient is independent of the bubble impact velocity due to the linear dependence of the forces on the velocity, which appears during the rebound. Experiments of Zenit and Legendre (2009) indicate that $K \approx 30$. The restitution coefficient behaves differently from that of solid spheres, where the restitution coefficient is described using the Stokes number $\mathrm{St} = (\rho + C_M\rho_p)u_s d_b/\mu$, thus being dependent on the impact velocity u_s (Joseph *et al.*, 2001; Legendre *et al.*, 2006). Note that the Ohnesorge number can be expressed as a function of the Stokes number as $\mathrm{Oh} = \sqrt{\mathrm{Ca}/\mathrm{St}}$. The main difference between the bubble and the solid sphere results from the significant deformability of the bubble surface during the interaction with the wall that in turn increases the contact time with the wall (Legendre *et al.*, 2006).

VI. BUBBLES IN COMPLEX FLUIDS

When the fluid that surrounds a bubble is not Newtonian, all of its dynamic properties can change. A fluid is considered Newtonian if the relationship between the stress tensor $\boldsymbol{\Sigma}$ and the strain-rate tensor $\mathbf{S}$ is linear,

$$\boldsymbol{\Sigma} = 2\mu\mathbf{S}, \tag{84}$$

where μ is the shear viscosity, which has a constant value. In any other case, the fluid is considered non-Newtonian. Non-Newtonian fluids can generally be divided into two broad categories: fluids with variable viscosity and fluids with an elastic stress component. In this section we first describe models for classical non-Newtonian rheologies and then discuss their impact on bubble dynamics.

A. An introduction to non-Newtonian liquids

The viscosity of a fluid can vary under different conditions. Neglecting the effect of temperature, the fluid viscosity can be shear dependent. Fluids whose viscosity decreases as the shear rate increases are called shear thinning (or pseudoplastic), while fluid that becomes more viscous with increasing shear rate is called shear thickening (or dilatant). A simple model that captures this behavior is the so-called power-law fluid (also called the Ostwald–de Waele model). Using Eq. (84) as a reference, the effective viscosity can be defined as

$$\mu_{\mathrm{eff}} = \kappa(\sqrt{\mathbf{S}:\mathbf{S}})^{n-1}, \tag{85}$$

where n and κ are the power index and the consistency. For $n < 1$ the effective fluid viscosity decreases as $\mathbf{S}$ increases. When $n = 1$, the Newtonian rheology is recovered. Thus, the shear-dependent behavior is characterized by the values of n and κ, which can be determined experimentally.

Shear-thinning fluids are the most common fluids found in both industrial and natural environments. While a precise physical model to explain the reason behind a shear-thinning (or shear-thickening) behavior does not exist, it can be argued that the reduction of viscosity results from microstructural changes of the fluid that facilitate flow as shear is increased. For instance, in polymers and polymer solutions, the shear-thinning behavior results from the disentanglement of polymeric strands during flow (Cross, 1979).

Note that the behavior predicted by the power-law model [Eq. (85)] is often valid only at an intermediate range of shear rates. For both low and high shear rates, the viscosity often recovers a constant value. To capture this nonmonotonic change of viscosity with shear rate, models with several more parameters are often used. Consider, for instance, the Carreau fluid model (Carreau, 1972).

The viscosity of fluids can change over time. Fluids that exhibit a decrease in viscosity with time at constant temperature are called thixotropic. For antithixotropic behavior (also called rheopectic behavior), an increase of viscosity with time can also be observed.

1. Bubble shape for shear-dependent viscosity fluids

The bubble shape, as discussed, is the result of the balance of surface tension forces and other fluid forces. In the case of bubbles moving in complex fluids, we can expect these properties to affect the bubble shape. There have been numerous studies that have documented the bubble shape

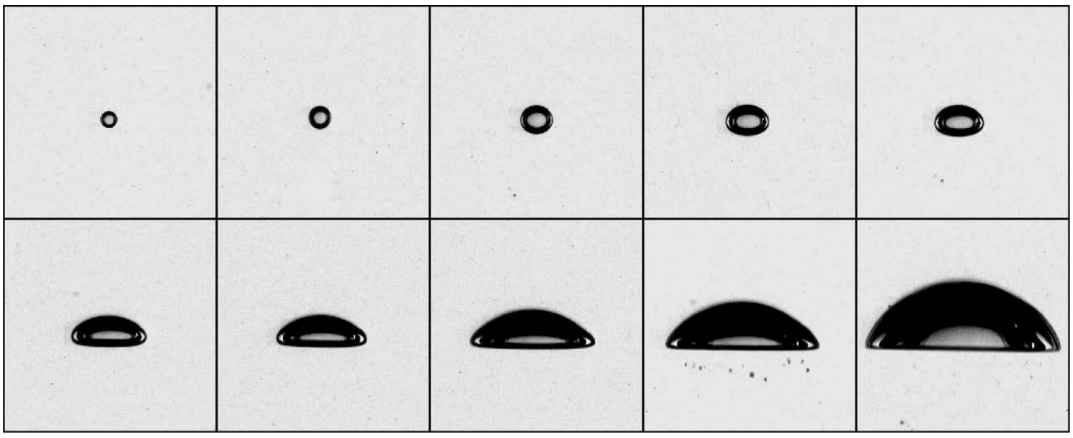

FIG. 17. Shape of bubbles in a shear-thinning fluid. The volume ranges from 2.65 to 22 mm^3 for the smallest to the largest bubbles shown, corresponding to bubble diameters ranging from 1.7 to 3.5 mm. The fluid is a mixture of ethylene glycol and Carbopol for which $\kappa = 0.19$ Pa $s^{0.8}$ and $n = 0.8$. Re $\sim O(1)$ and Mo $\sim O(10^{-2})$. Original data.

in non-Newtonian liquids (Chhabra, 2006), but the results are sparse and generally lack a fundamental understanding of the underlying physical mechanisms. In most cases the experiments are conducted for fluids that exhibit shear-thinning and viscoelastic effects simultaneously, which makes the physical interpretation more difficult. Figure 17 shows how the bubble shape evolves as the diameter increases for a fluid that is inelastic but shear thinning (Zenit and Feng, 2018). The bubble shape evolves from spherical to ellipsoidal to spherical cap, which resembles what is observed in viscous Newtonian fluid, as shown in Fig. 7. Note that a proper comparison would need to consider the value of the Morton number, as discussed in Sec. III.C. However, since the fluid is shear thinning, as bubble size increases the effective viscosity decreases. Therefore, even for the same liquid, the Morton number is no longer constant, making direct comparisons challenging. Nevertheless, the images indicate that for this moderate value of the power index n, the bubble deformation is qualitatively similar to that observed in a Newtonian liquid, in accordance with the numerical results of Zhang, Yang, and Mao (2010). A general map that shows the shapes of bubbles in shear-dependent liquids, similar to the classical one of Clift, Grace, and Weber (1978), does not exist.

In contrast, even if the bubble shape is not significantly altered by shear-thinning viscosity, the bubble terminal velocity does change with values of the power index and consistency, n and κ, respectively. Vélez-Cordero *et al.* (2011) showed that for moderate values of Re, the drag coefficient of bubbles decreases with the power index n. Hence, bubbles in such shear-thinning fluids would have a larger terminal speed u_∞, in accordance with several other studies (Chhabra, 2006). This increase is expected since the bubble motion creates a low-viscosity region around it. Hence, the viscous dissipation around the bubble is smaller.

2. Bubble shape for viscoelastic fluids

The typical case for which the stress in the fluid is not purely viscous is an intermediate state between an elastic solid and a viscous fluid. In such a case, the stress in the fluid results from both deformation and deformation rate. The simplest model of viscoelasticity is the linear viscoelastic model, for which these two effects are linearly superposed,

$$\boldsymbol{\Sigma} + \lambda_1 \frac{\partial \boldsymbol{\Sigma}}{\partial t} = \mu \left(\mathbf{S} + \lambda_2 \frac{\partial \mathbf{S}}{\partial t} \right), \tag{86}$$

where λ_1 and λ_2 are the elastic relaxation and retardation times, respectively. This model is the so-called Jeffrey model. Although it captures some features of viscoelasticity, its applicability is limited. The relative importance of elastic effects in a flow is often given by the dimensionless relaxation time:

$$\mathrm{Wi} = \frac{\lambda_1 u_b}{d_b}. \tag{87}$$

The Weissenberg number (Wi) measures whether the elastic relaxation time is larger that the flow time. Hence, a Newtonian fluid will have $\mathrm{Wi} = 0$, while a purely elastic solid would have $\mathrm{Wi} \to \infty$. Linear viscoelastic models are often valid only when $\mathrm{Wi} \to 0$.

In particular, the main issue with these linear viscoelastic models is that they are not independent of the frame of reference. This lack of frame independence arises from the nonobjectivity of total derivatives for tensorial quantitites. To address this issue, one can propose total derivatives that are objectively defined in the frame of reference of fluid particles. These convective derivatives are used to ensure the objectivity of nonlinear viscoelastic models. By replacing the time derivatives in Jeffrey's model [Eq. (86)] with the upper-convective derivative (Oldroyd, 1950), we arrive at

$$\boldsymbol{\Sigma} + \lambda_1 \overset{\triangledown}{\boldsymbol{\Sigma}} = \mu (\mathbf{S} + \lambda_2 \overset{\triangledown}{\mathbf{S}}), \tag{88}$$

where the upper-convected time derivative is defined as

$$\overset{\triangledown}{\mathbf{A}} = \frac{\partial \mathbf{A}}{\partial t} + (\mathbf{u} \cdot \boldsymbol{\nabla})\mathbf{A} - (\mathbf{G})^T \cdot \mathbf{A} - \mathbf{A} \cdot \mathbf{G}. \tag{89}$$

In Eq. (89) $\mathbf{A}$ is a tensor, $\mathbf{u}$ is the velocity field, and $\mathbf{G} = \nabla\mathbf{u}$ is the velocity gradient tensor. There are other objective derivative operators (such as the lower-convected and corotational derivatives) that are valid and that can also be used (Bird, Armstrong, and Hassager, 1987).

One of the consequences of this type of rheological constitutive equation is that the normal stress differences in the fluid can be other than zero,

$$N_1 = \sigma_{xx} - \sigma_{yy}, \tag{90}$$

$$N_2 = \sigma_{yy} - \sigma_{zz}. \tag{91}$$

Both N_1 and N_2 are generally functions of the amount of shear in the flow but, most importantly, are equal to zero in Newtonian fluids (Bird, Armstrong, and Hassager, 1987). The normal stress differences are responsible for many of the unusual experimental observations in viscoelastic flows such as the Weissenberg effect (Lodge, Schieber, and Bird, 1988), the die swell effect (Tanner, 1970), the vortex rotation reversal (Palacios-Morales *et al.*, 2015), and the bubble velocity discontinuity (Zenit and Feng, 2018) discussed later.

The effect of these elastic normal stress differences can be readily observed in flows dominated by shear. In the flow around bubbles, there are parts of the flow, such as the wake, that are dominated by shear. Consequently, we can expect to observe the manifestation of elastic effects in the flow around bubbles in such liquids. Figure 18 shows the shape of bubbles in a viscoelastic liquid. Note that the shape of bubbles in such liquids deviates significantly from what is observed in a Newtonian one; see Fig. 7. In general, in these fluids the bubble shape is more elongated in the flow direction owing to the appearance of normal stresses due to high shear in the bubble equatorial region. As bubbles reach a critical size, the rear side develops a teardrop shape that, as later explained, is related to the bubble velocity discontinuity phenomenon. The tip of the bubble can become sharp and elongated (Soto *et al.*, 2006). As the bubble size increases, inertial effects that make the bubble adopt an ellipsoidal shape that retains the pointy tip become important. Again, many studies have addressed the effect of liquid rheology on the bubble shape (Chhabra, 2006), but a fundamental understanding of the process is still lacking. A bubble shape map for viscoelastic fluids akin to Clift's map for Newtonian liquids (Clift, Grace, and Weber, 1978) does not yet exist. Such a map would have to include a third axis to account for changes of shape resulting from different values of Wi.

B. Bubble velocity discontinuity and negative wake

As in the case of bubbles moving in Newtonian liquids, as the bubble size increases, the terminal speed increases as long as the deformation is not significant. Figure 19 shows the terminal velocity for an air bubble rising in different viscoelastic shear-thinning fluids. For bubble sizes smaller than a certain size, the bubble velocity increases monotonically with bubble diameter but at a rate larger than d_b^2, as observed in Newtonian fluids, depending on the fluid. This different trend is an indication of the nonlinear nature of the drag force. Recall that the d_b^2 dependency of the bubble speed was determined from the balance between a linear drag and buoyancy; hence, a deviation from such a trend indicates that F_D is no longer linear with d_b and/or u_b. Note also that, as discussed, the bubble shape becomes more elongated in the motion direction. Soto-Castruita (2008) found that the drag coefficient can be reduced by up to 40% only from the change of shape due to elastic effects. The different trend of u_∞ with d_b for small bubble sizes already gives an indication of the different behavior observed in viscoelastic fluids, but a detailed physical explanation is still lacking.

However, the most noteworthy feature in the data shown in Fig. 19 is the appearance of discontinuity of the bubble velocity. At a certain critical bubble diameter d_b^{crit}, the bubble terminal velocity increases sharply. For instance, for the data shown in Fig. 19 with the blue squares, the critical bubble diameter is $d_b^{\mathrm{crit}} \approx 2.94$ mm. The terminal velocity jumps from 23.8 to 83.7 mm/s, with a slight increase in diameter.

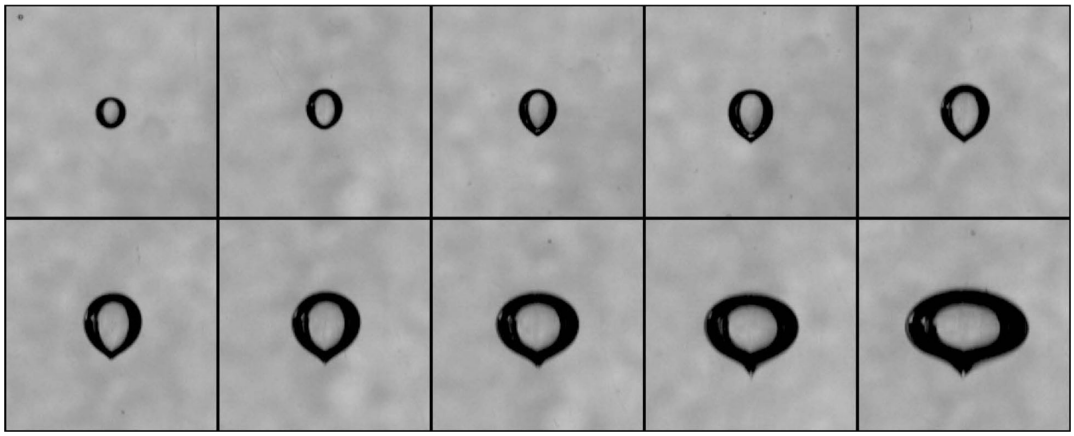

FIG. 18. The shape of bubbles in a viscoelastic fluid. The volume ranges from 12 to 440 mm^3, corresponding to bubble diameters ranging from 2.8 to 9.5 mm for the smallest to the largest bubble shown. The critical bubble size in this sequence corresponding to the velocity discontinuity, as shown in Fig. 19, is between the third and fourth images on the top row. The fluid is a mixture of water and polyacrylamide for which $\kappa = 1.92\ \mathrm{Pa\,s}^{0.12}$, $n = 0.12$, $\lambda_1 = 12$ s, $\mathrm{Re} \sim \mathrm{O}(1)$, $\mathrm{Mo} \sim \mathrm{O}(10)$, and $\mathrm{Wi} \sim \mathrm{O}(10)$. Adapted from Ravisankar, 2021.

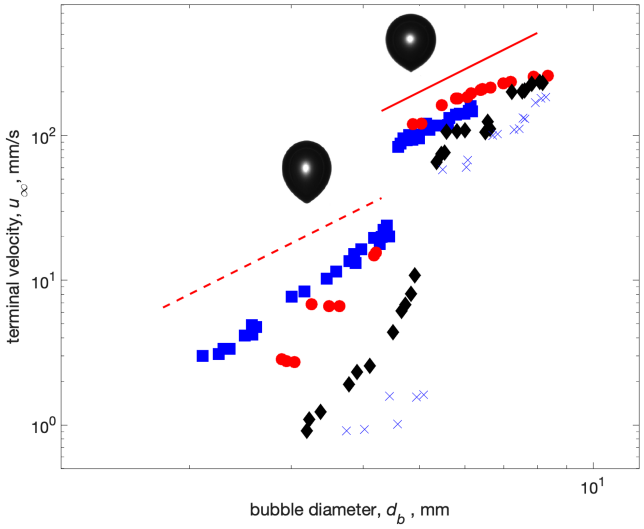

FIG. 19. Bubble terminal velocity in different viscoelastic fluids as a function of the bubble diameter. Shown are the experimental data of Pilz and Brenn (2007): blue squares, Re ~ 10, Wi ~ 10, and $d_b^{\text{crit}} = 4.49$ mm; bubble images $d_b = 4.43$ mm (lower left) and $d_b = 4.61$ mm (upper right). The fluid is an aqueous solution of 0.8 wt % polyacrylamide Praestol 2500, which is viscoelastic ($\lambda_1 = 0.21$ s) and shear thinning ($n \approx 0.5$). Also shown are the experimental data of Ravisankar *et al.* (2022): black dots, Re ~ 1, Wi ~ 20, and $d_b^{\text{crit}} = 4.54$ mm; black diamonds, Re ~ 0.5, Wi ~ 10, and $d_b^{\text{crit}} = 5.10$ mm; and blue multiplication signs, Re ~ 0.2, Wi ~ 10, and $d_b^{\text{crit}} = 5.29$ mm. These fluids are aqueous solutions of polyacrylamide Separan AP30, with concentrations of 0.15, 0.20, and 0.25 wt %, with relaxation times in the range $5 < \lambda_1 < 39$ s and power indices in the range $0.08 < n < 0.21$ (viscoelastic and shear thinning). The lines show $u_\infty \sim d_b^2$.

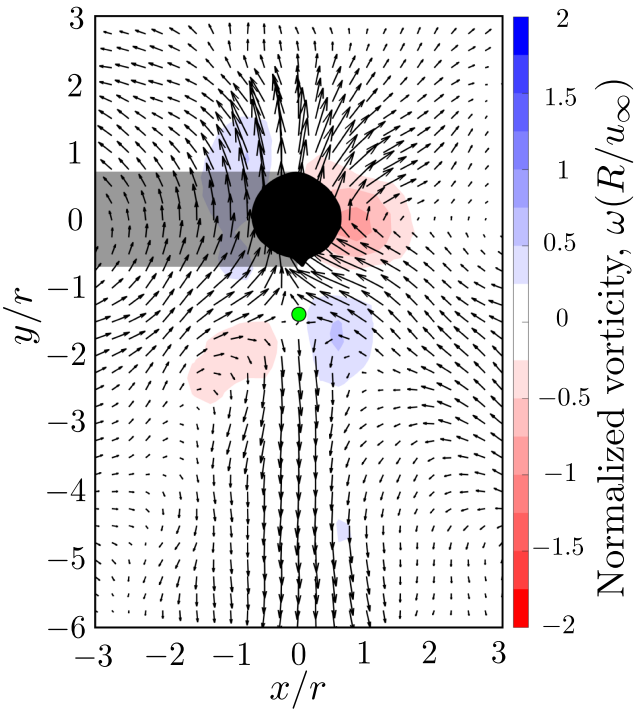

FIG. 20. Velocity field behind a bubble rising in a viscoelastic, shear-thinning fluid at Wi ~ 5 in the laboratory reference frame $\mathcal{R}$. Colors represent vorticity, and the green dot shows the location of the stagnation point between the forward-moving fluid and the reversed flow in the negative wake. From Ravisankar *et al.*, 2022.

This phenomena, discovered by Astarita and Apuzzo (1965), remained unexplained for years until recent studies offered insights (Fraggedakis *et al.*, 2016; Bothe *et al.*, 2022). The increase in bubble size leads to a change in bubble shape that has less viscous drag, which causes a slight increase in velocity. This triggers the shear-thinning nature of the fluid, which further boosts the bubble velocity, which in turn induces further changes in the shape. These two effects, combined with the reduction of the accumulation of surfactants for faster bubbles, leads to a significant increase in velocity (Zenit and Feng, 2018). The data in Fig. 19 show that this phenomenon is observed for moderate values of Re and for Wi of order 1. For bubbles beyond the critical size, the bubble velocity shows a dependence closer to d_b^2, suggesting that at larger diameters and higher speeds, viscoelastic effects become less significant. Despite these observations, a clear physical explanation of how elasticity influences bubble terminal velocity remains elusive.

An important feature of the motion of bubbles in viscoelastic media is the appearance of a negative wake. In viscoelastic fluids stress accumulates and relaxes over time, rather than instantly as in Newtonian fluids. When a bubble traverses the liquid, it causes flow and continuous deformation that induce fluid stress. Unlike Newtonian fluids, where the fluid relaxes immediately once the bubble passes, the memory effect of the viscoelastic fluid causes the stress to remain present for a certain time, proportional to the elastic relaxation time λ_1. This phenomenon is illustrated in Fig. 20, which shows the velocity field around a bubble rising in a viscoelastic fluid. In contrast to a Newtonian fluid, where the fluid follows the bubble, viscoelastic fluids exhibit flow reversal at a certain distance behind the bubble. In other words, the fluid returns to the configuration that it had before the passage of the bubble. This so-called negative wake was first reported by Hassager (1979) but has been studied by many since then (Zenit and Feng, 2018). This flow reversal can be observed in the wake behind particles, drops, or bubbles in viscolastic liquids. However, owing to the small bubble mass, changes in the fluid stress have a significant impact on the bubble terminal velocity u_∞. Herrera-Velarde *et al.* (2003) argued that the negative wake contributed to the appearance of the bubble velocity discontinuity because they appeared simultaneously.

C. Hydrodynamic interactions among bubbles in complex fluids

Given the complexity introduced by the non-Newtonian properties of the liquid on the motion and shape of bubbles, it is not surprising to find that the interactions among bubbles are significantly affected. Although in many practical applications the motion of bubbles in non-Newtonian liquids is prevalent, a general understanding of bubble clustering and induced mixing is not currently available. Some of the issues

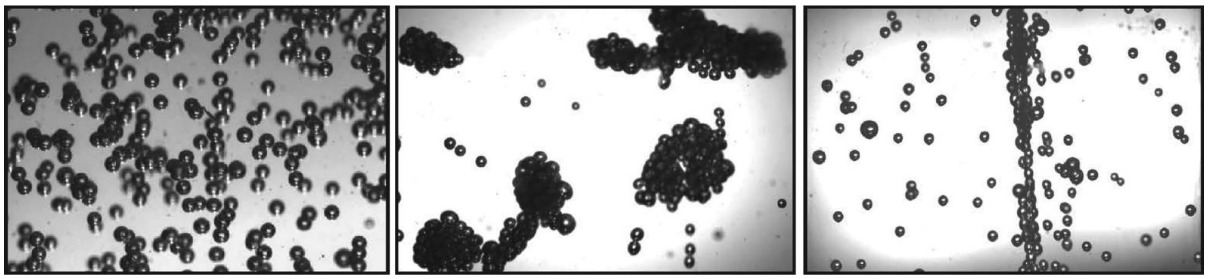

FIG. 21. Clusters in non-Newtonian bubbly flows. Left image: Newtonian liquid. Center image: shear-thinning liquid. Right image: viscoelastic liquid. The three images are for the same gas volume fraction $\alpha_G = 0.05$. Adapted from Zenit and Feng, 2018.

in understanding bubble-bubble pair hydrodynamic interactions in non-Newtonian liquids were addressed by Vélez-Cordero *et al.* (2011), Vélez-Cordero and Zenit (2011), Vélez-Cordero, Sámano, and Zenit (2012), and Ravisankar *et al.* (2022), but a mature level of understanding has not been reached.

In general, shear-thinning and viscoelastic effects result in interaction forces that promote the clustering and agglomeration of bubbles, as shown in Fig. 21. The low-viscosity region around a bubble in shear-thinning fluids can serve to capture neighboring bubbles. The elastic stresses in the equatorial region of bubbles, where shear dominates, can attract bubbles to form clusters. Clustering leads to coalescence, which in turn leads to the formation of large bubbles that produce regime changes (Zenit and Feng, 2018) and results in velocities and mixing of different magnitudes than those expected for dispersed bubbly liquids (Risso, 2018).

VII. EQUATION OF BUBBLE MOTION, VISCOUS RELAXATION TIME, STOKES NUMBER, AND HISTORY FORCE

A. Equation of bubble motion

Following the work of Gatignol (1983), Maxey and Riley (1983), Thomas *et al.* (1983), and Auton, Hunt, and Prud'Homme (1988), we now rewrite Eq. (1) as a complete equation of motion for a spherical bubble moving at the velocity $\mathbf{u}_b = d\mathbf{x}_b/dt$ in a Newtonian liquid with a velocity $\mathbf{U}(\mathbf{x}, t)$,

$$C_M \rho \vartheta_b \frac{d\mathbf{u}_b}{dt} = -\rho \vartheta_b \mathbf{g} \qquad \text{(buoyancy)}, \tag{92}$$

$$+2\pi\mu d_b \mathcal{K}(\mathrm{Re})(\mathbf{U}-\mathbf{u}_b) \qquad \text{(drag)}, \tag{93}$$

$$+\rho\vartheta_b(1+C_M)\left(\frac{\partial \mathbf{U}}{\partial t}+\mathbf{U}\cdot\boldsymbol{\nabla}\mathbf{U}\right)_{\mathbf{x}_b} \qquad \text{(inertial and added mass)}, \tag{94}$$

$$+\ C_L\rho\vartheta_b(\mathbf{U}-\mathbf{u}_b)\times\Omega \qquad \text{(lift)}. \tag{95}$$

This force decomposition extends the expression derived by Auton, Hunt, and Prud'Homme (1988) for the case of a rigid sphere in an unsteady inviscid rotational flow. Its validity has been confirmed by numerical studies such as those discussed by Magnaudet and Eames (2000).

We can analyze each of the contributions to Eq. (95). The bubble acceleration of the added mass (on the left-hand side) is balanced by the forces (on the right-hand side from top to bottom): the buoyancy force $\mathbf{F}_B$ reduced to the Archimedes force, the drag force $\mathbf{F}_D$, the generalized inertia force due to the time and space acceleration of the fluid, and finally the lift force $\mathbf{F}_L$. Not included in Eq. (95), because they are negligible in most cases, are the bubble's own acceleration, its weight, and the history force $\mathbf{F}_H$ (discussed later). Equation (95) is usually rewritten by dividing all of the terms by $C_M\rho\vartheta_b$ to express the bubble acceleration $\mathbf{a}_b$ as

$$\mathbf{a}_b = \frac{d\mathbf{u}_b}{dt} = \frac{1}{\tau_b}(\mathbf{U}-\mathbf{u}_b)+\gamma\left(\frac{\partial \mathbf{U}}{\partial t}+\mathbf{U}\cdot\boldsymbol{\nabla}\mathbf{U}\right)_{\mathbf{x}_b}+\gamma'(\mathbf{U}-\mathbf{u}_b)\times\Omega+\gamma''\mathbf{g}, \tag{96}$$

where we have introduced the characteristic, relaxation, or response time of the bubble

$$\tau_b = \frac{C_M d_b^2}{12\nu\mathcal{K}(\mathrm{Re})}, \tag{97}$$

as well as the ratios $\gamma = (1+C_M)/C_M$, $\gamma' = C_L/C_M$, and $\gamma'' = -1/C_M$ that correspond to the mass accelerated by the fluid, the mass involved in the lift effect, and the mass accelerated by gravity, respectively, compared to the mass accelerated by the bubble motion. For spherical bubbles $\gamma = 3$, $\gamma' \approx 1$ for $\mathrm{Re} \gg 1$ and $\gamma'' = -2$. Note that these coefficients differ from those considered for heavy particles of density ρ_p, $\gamma = \rho(1+C_M)/(\rho_p + C_M\rho)$, $\gamma' = \rho C_L/(\rho_p + C_M\rho)$, and $\gamma'' = (\rho_p - \rho)/(\rho_p + C_M\rho)$, resulting in different behaviors.

Equations (92) and (93)–(94) and (95) [or Eq. (96) with the appropriate expressions for the drag Re correction $\mathcal{K}(\mathrm{Re})$, the added mass coefficient C_M, and the lift coefficient $C_L(\mathrm{Re}, \mathrm{Sr})$ are commonly used to investigate turbulent dispersed bubbly flows (Mazzitelli, Lohse, and Toschi, 2003a; Sugiyama, Calzavarini, and Lohse, 2008; Chouippe *et al.*, 2014; Mathai *et al.*, 2016; Muniz and Sommerfeld, 2020; Ruth *et al.*, 2021). Numerical studies based on Lagrangian tracking of bubbles are based on the point-force assumption (point bubble) that formally requires $d_b \ll \eta$, where η is the Kolmogorov length scale. When this condition is not satisfied, Eqs. (92) and (93)–(94) and (95) need to include Faxén terms both in the

drag force [Eq. (93)] and in the inertia-added mass force [Eq. (95)], as discussed by Homann and Bec (2010).

B. Viscous relaxation time and Stokes number

Consider a spherical bubble placed at the bottom of a tank filled with a fluid at rest ($\mathbf{U} = 0$) with no initial velocity. As discussed, the bubble reaches its terminal velocity u_∞ when the buoyancy force is balanced by the drag force. We now consider the transient evolution of the bubble motion before reaching the terminal velocity. When we consider $\mathbf{U} = 0$ in Eq. (96), group all of the terms in $\mathbf{u}_b$ on the left-hand side, and take $C_M = 1/2$, the equation can be simplified as

$$\frac{d\mathbf{u}_b}{dt} + \frac{\mathbf{u}_b}{\tau_b} = -2\mathbf{g}, \tag{98}$$

where we see that the viscous relaxation time $\tau_b = d_b^2/24\nu\mathcal{K}(\mathrm{Re})$ determines the transient evolution of the velocity. Note that the initial acceleration of the bubble is twice that of gravity. Equation (98) can be readily solved when τ_b is constant, which is the case when $\mathrm{Re} \to 0$ ($\mathcal{K} = 1$) and when $\mathrm{Re} \to \infty$ ($\mathcal{K} = 3$). In such cases, the evolution of the velocity is

$$\mathbf{u}_b = \mathbf{U}_\infty \left[1 - \exp\left(-\frac{t}{\tau_b}\right)\right], \tag{99}$$

with $\mathbf{U}_\infty = -2\tau_b\mathbf{g} = -d_b^2\mathbf{g}/12\nu\mathcal{K}(\mathrm{Re})$. The evolution of $\mathbf{u}_b$ with time is shown in Fig. 22(a). The bubble reaches its terminal velocity (95%) at about $t = 3\tau_b$.

The bubble relaxation time is $\tau_b = 4 \times 10^{-4}$ s for a bubble with a diameter $d_b = 0.1$ mm in water ($u_\infty \approx 0.01$ m/s and $\mathrm{Re} \approx 1$). For a bubble 10 times larger, $d_b = 1$ mm that is also in water ($u_\infty \approx 0.27$ m/s and $\mathrm{Re} \approx 270$), the relaxation time increases to $\tau_b = 1.4 \times 10^{-2}$ s. As a consequence, the transient phase of the bubble motion can be neglected in most situations compared to the bubble resident time in the system. For example, for a tank with a height $h = 1$ m, the resident time $T \approx h/u_\infty$ would be 100 and 3 s, respectively, for the two previously considered bubble sizes.

In a situation where the liquid is moving at a uniform velocity $\mathbf{U}$, the equation of motion is

$$\frac{d\mathbf{u}_b}{dt} + \frac{\mathbf{u}_b}{\tau_b} = -2\mathbf{g} + \frac{\mathbf{U}}{\tau_b}. \tag{100}$$

The bubble system is now subject to external forcing from two contributions: the gravity $\mathbf{g}$ and the liquid velocity $\mathbf{U}$, with the same relaxation time τ_b. The final bubble velocity is then $\mathbf{u}_b = \mathbf{U}_\infty + \mathbf{U}$, and the transient phase is described by $[1 - \exp(-t/\tau_b)]$. The bubble relaxation time τ_b provides a characteristic time for which a bubble can respond to any external forcing or change in its environment (gravity and liquid motion). It is thus used to describe how bubbles react to various flow situations. Figures 22(b) and 22(c) illustrate two possible situations. In Fig. 22(b), the bubble is rising in a vertical upward flow such that $U \gg u_\infty$. The flow is moving around a horizontal plate. In Fig. 22(c) the bubble interacts with a vortex as it rises. In both cases two possible situations can be observed: the bubble follows the flow streamlines [as it moves around the plate in (b) or gets trapped by the vortex in (c)] or is not influenced by the flow [it impacts the wall in (b) and crosses the vortex in (c)]. The answer can be determined by comparing the bubble relaxation time to the characteristic time of the flow τ_f in each situation. In both cases the characteristic flow time can be $\tau_f \approx H/U$. A dimensionless number, the Stokes number, can thus be defined as

$$\mathrm{St}_b = \frac{\tau_b}{\tau_f}. \tag{101}$$

When $\mathrm{St}_b \ll 1$, the bubble is fast to adapt to any fluid modification and is able to follow the flow like a tracer,

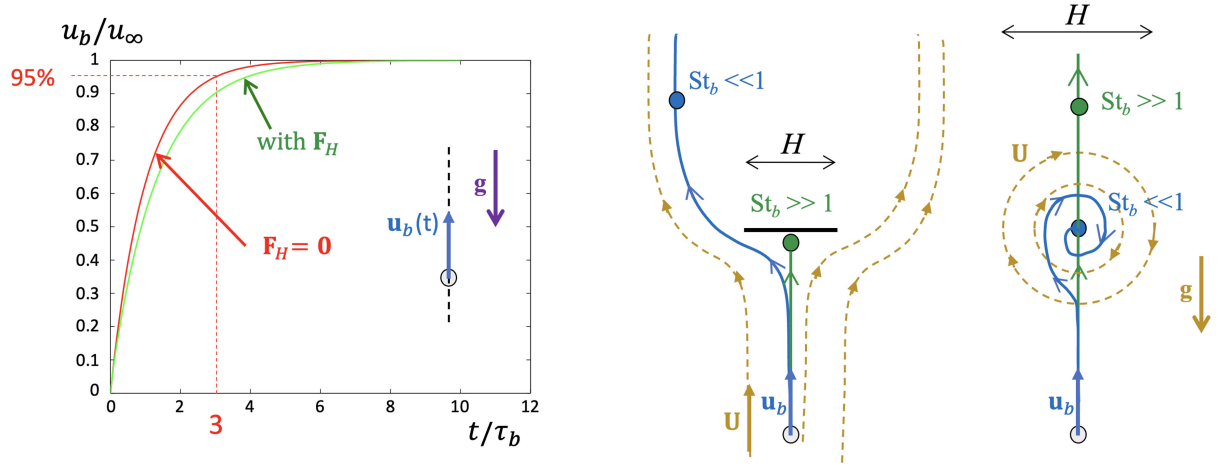

FIG. 22. (a) Bubble velocity evolution when released from rest. The green line shows the effect of the history force when integrated into Eq. (98). (b) Bubble trajectory when varying the Stokes number St_b during transport by a vertical flow. (c) Like (b) but for a bubble interacting with a vortex structure.

while when $\mathrm{St}_b \gg 1$ the bubble is slow to react and follows its original trajectory, thus impacting the wall in Fig. 22(b) or moving across the vortex in Fig. 22(c). The Stokes number is used, for instance, to describe how bubbles are influenced by turbulence, as detailed in Sec. VIII.

C. History force

Figure 22(a) shows the bubble rising velocity with and without considering the history force $\mathbf{F}_H$ in Eqs. (92) and (93)–(94) and (95) [and in Eq. (98)]. The history force $\mathbf{F}_H$ corrects the steady drag force, that is, when the viscous effects do not have enough time to establish the flow field around the bubble when compared to the timescale of the flow. The history force can be calculated under Stokes flow conditions ($\mathrm{Re} \ll 1$) as (Gorodtsov, 1975; Yang and Leal, 1991)

$$\mathbf{F}_H = 8\pi\mu R \int_0^t \exp\left[9\frac{t-t'}{t_\nu}\right] \mathrm{erfc}\left[3\sqrt{\frac{t-t'}{t_\nu}}\right] \left(\frac{d\mathbf{U}}{dt'} - \frac{d\mathbf{u}_b}{dt'}\right) dt', \tag{102}$$

where $t_\nu = R^2/\nu$ is the characteristic diffusion time of momentum in the liquid. The kernel $K(t-t')$ for a spherical bubble evolves as $K(t-t') \approx \exp[9(t-t')/t_\nu] \times \mathrm{erfc}[3\sqrt{(t-t')/t_\nu}]$, resulting in a finite contribution to the total force at short times, in contrast to the Basset-Boussinesq kernel for a solid sphere that diverges as $\sqrt{t_\nu/(t-t')}$, resulting in less important history effects for spherical bubbles when compared to solid spheres. In general, $\mathbf{F}_H$ can be neglected for the case of a bubble when compared to the steady drag force (Magnaudet, Rivero, and Fabre, 1995). The contribution of the history force is expected to be at maximum at small Reynolds numbers. As shown in Fig. 22(a), when integrated to the equation of motion for a rising bubble, the history force does not have a noticeable effect on the transient motion. However, in flows oscillating at high frequency, the history force should be added in the trajectory equation. Some experiments have evidenced the role of the history force. For example, the history force has been shown to contribute to the slow migration of bubbles rising in a vortex (Candelier, Angilella, and Souhar, 2005). For oscillating, collapsing, or growing bubbles in motion, the history force can be important. The correction induced by the volume variation was derived by Magnaudet and Legendre (1998), and the importance of the history force in this condition was reported in experiments on microbubbles propelled by acoustic radiation force (Garbin *et al.*, 2009) and in experiments on sonoluminescing bubbles trapped in standing sound waves (Toegel, Luther, and Lohse, 2006).

VIII. BUBBLE DYNAMICS IN TURBULENCE

A bubble moving through a turbulent flow interacts with vortices (or eddies) of various length, time, velocity, and acceleration scales, resulting in significant bubble deformation and chaotic trajectories, as illustrated in Fig. 23. There are several length scales relevant to the interaction of a bubble with turbulence: η is the dissipative Kolmogorov length scale, λ is the intermediate Taylor microscale, and L_i is the integral length scale of the flow. The Kolmogorov length scale and timescale are determined by $\eta = (\nu^3/\varepsilon)^{1/4}$ and $\tau_\eta = (\nu/\varepsilon)^{1/2}$, respectively, where ε is the energy dissipation rate. In the following discussion, ℓ represents a characteristic size of a turbulent eddy. In general, in the inertial subrange we have $\eta \ll \ell \ll \lambda$. We also introduce the fluctuating velocity intensity u', which is the root-mean-square value of the free stream velocity. Using u', we can define the ratio $\beta = u'/u_\infty$ that compares u' with the bubble rising velocity u_∞ without turbulence.

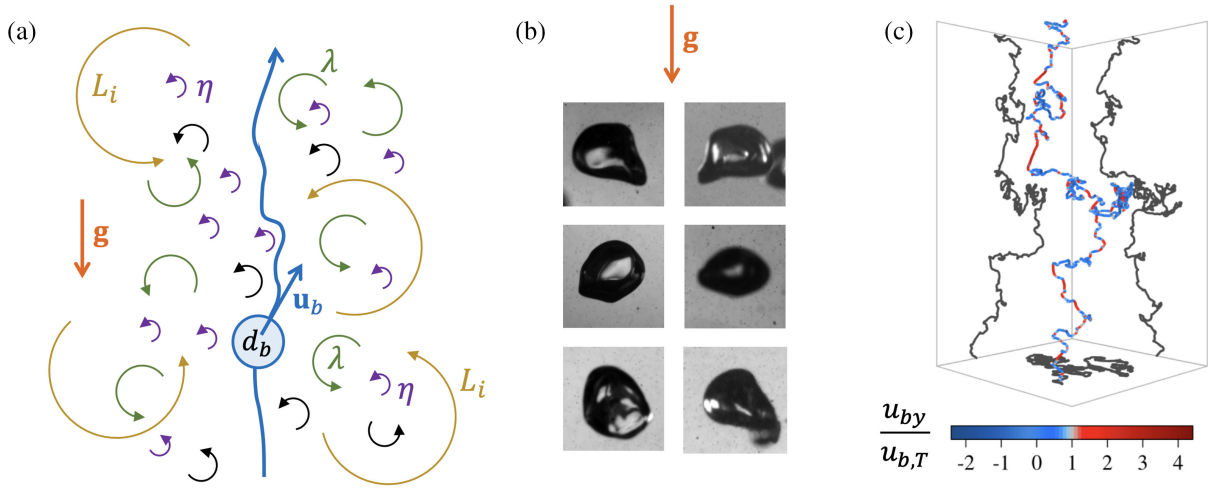

FIG. 23. A bubble rising in a turbulent field. (a) The turbulent field consists of eddies of various length scales. Adapted from Mathai, Lohse, and Sun, 2020. The bubble's size d_b is in the inertial subrange ($\eta < d_b < L_i$, where η is the Kolomogorov length scale and L_i is the integral length scale). λ is the Taylor microscale. (b) Large bubble ($d_b = 3.2$ mm) shape on six views during its rise in an intense homogeneous and isotropic turbulence $u' = 0.25$ m/s, $L_i = 3.2$ cm, and $\eta = 38$ μm. Courtesy of R. Ni. (c) Trajectory of a bubble, obtained by direct numerical simulation, rising in a homogeneous isotropic turbulence for $\beta = 0.9$, $\eta/d_b = 0.098$, $\lambda/d_b = 1.0$, and $L_i/d_b = 2.1$. The color code indicates the instantaneous bubble vertical velocity u_{by} normalized by the terminal velocity of the same bubble u_∞ in a quiescent liquid (Loisy and Naso, 2017).

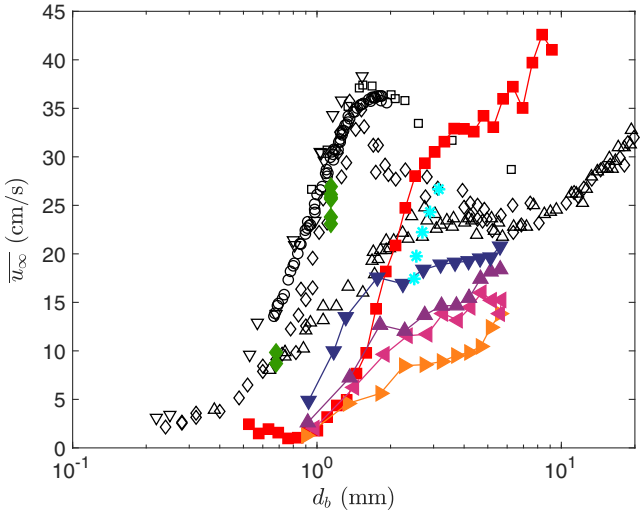

FIG. 24. Mean terminal velocity $\overline{u_\infty}$ of air bubbles rising in water for different levels of turbulence u' as a function of their equivalent diameter d_b. The empty black markers show the experiments conducted in a quiescent water that are shown in Fig. 4 ($u' = 0$, no turbulence). The filled and color markers show experimental data from the literature. Clean bubbles: green diamonds, 0.03 m/s $< u' \leq$ 0.06 m/s. From Poorte and Biesheuvel, 2002. Contaminated bubbles: cyan asterisks. From Prakash *et al.*, 2012. Red squares, $u' = 0.25$ m/s. From Salibindla *et al.*, 2020. Filled down triangles, 0.02 m/s $< u' \leq$ 0.05 m/s. Filled up triangles, 0.05 m/s $< u' \leq$ 0.10 m/s. Filled left triangles, 0.10 m/s $< u' \leq$ 0.15 m/s. Filled right triangles, 0.15 m/s $< u' \leq$ 0.20 m/s. From Ruth *et al.*, 2021.

The evolution of the mean rising velocity $\overline{u_\infty}$ of an air bubble in water is reported in Fig. 24 as a function of its diameter d_b for different levels of turbulence u'. We can compare these speeds with the free bubble rising velocity in a quiescent fluid; see Fig. 4. The turbulence has a significant impact on the bubble mean rising velocity, revealing a strong interaction with the turbulence. The trends also seem to differ for various experimental investigations. For bubbles with a clean interface and u' ranging from 0.03 to 0.06 m/s, Poorte and Biesheuvel (2002) reported a decrease of the bubble mean rise velocity up to 35% compared with the quiescent conditions. For u' ranging from 0.02 to 0.2 m/s, Ruth *et al.* (2021) reported a significant decrease in the mean rising velocity with turbulence and $\overline{u_\infty}$ is always found to be smaller than the rise in quiescent water. This trend was also reported by Salibindla *et al.* (2020) for bubbles smaller than $d_b = 2$ mm, whereas for larger diameters they observed that bubbles actually rise faster than in quiescent water. Most of the experiments report a strong effect for small bubbles, typically less than 1 mm. Such bubbles appear to be slowed down significantly in the turbulence, with their rising velocity reduced by more than 1 order of magnitude.

We first describe the different mechanisms frequently used to explain bubble behavior when rising in turbulence. This discussion is limited to the case where the turbulence is not strong enough to cause bubble rupture, as discussed in Sec. III.C.4. Depending on the dominant mechanisms, different behavior can be observed as resulting in bubble capture, reduction, or increase of the rising velocity. We then discuss the main results concerning small and large bubbles relative to the smallest turbulent scale η. We focus on the mean bubble rise velocity $\overline{u_\infty}$. Information on bubble velocity and acceleration fluctuations was provided by Loisy and Naso (2017) and Zhang (2019). The probability density function (PDF) of horizontal velocity fluctuations has been reported to be Gaussian, while for the vertical fluctuations the distribution shows small departure from Gaussianity (Poorte and Biesheuvel, 2002; Prakash *et al.*, 2012). The PDFs of bubble acceleration are highly non-Gaussian and exhibit large tails. See Mathai, Lohse, and Sun (2020) for a recent review on bubbly and buoyant particle-laden turbulent flows.

A. Main mechanisms of interaction with turbulence

Two mechanisms are often considered to explain how the bubble motion is affected by the turbulence. These mechanisms are illustrated in Fig. 25: bubbles can be trapped inside vortices (Wang and Maxey, 1993) or drifted toward downflow regions due to lift force effects (Spelt and Biesheuvel, 1997).

We first consider a bubble rising through a steady vortex of size ℓ in the vertical (x, y) plane with a constant angular velocity ω_ℓ, as shown in Fig. 25(a). Cylindrical coordinates $(\mathbf{e_r}, \mathbf{e}_\theta, \mathbf{e_z})$, with its origin at the vortex center O_ℓ, are used for convenience to express the forces. The velocity field is given by $\mathbf{U} = \omega_\ell r \mathbf{e}_\theta$ and the vorticity field is $\mathbf{\Omega} = 2\omega_\ell \mathbf{e}_z$. According to Eqs. (92) and (93)–(94) and (95), during its interaction with the vortex the bubble, moving at velocity $\mathbf{u}_b = u_{br}\mathbf{e}_r + u_{b\theta}\mathbf{e}_\theta$, is subject to the drag force $F_D = 2\pi\mu d_b \mathcal{K}(\mathrm{Re})[-u_{br}\mathbf{e}_r + (\omega_\ell r - u_{b\theta})\mathbf{e}_\theta]$, the inertia force $F_I = -\rho\vartheta_b(1 + C_M)\omega_\ell^2 r\mathbf{e}_r$, the lift force $F_L = 2\rho\vartheta_b C_L \omega_\ell[(\omega_\ell r - u_{b\theta})\mathbf{e}_r + u_{br}\mathbf{e}_\theta]$, and the buoyancy force $\mathbf{g} = -g\mathbf{e}_y$. When we consider an equilibrium position (r_e, θ_e) at which $(u_{br} = u_{b\theta} = 0)$, the force balance results in

$$\sin\theta_e = [1 + C_M - 2C_L]\frac{\omega_\ell^2 r_e}{g}, \quad \cos\theta_e = -\frac{\omega_\ell r_e}{u_\infty}. \tag{103}$$

Equation (103) indicates that $\cos\theta_e$ is always negative; thus, the equilibrium position is located in the left half of the vortex depicted in Fig. 25(a), where the vertical component of the fluid velocity is negative. The sign of $\sin\theta_e$ depends on the sign of $1 + C_M - 2C_L$. Typically, for a spherical bubble at Re > 100, $C_L \approx C_M = 0.5$, so $1 + C_M - 2C_L \approx 0.5$ is positive and, therefore, the stable position is then in the top left quadrant.

Equation (103) indicates that (i) a bubble can be trapped in a vortex and (ii) once trapped, the bubble can experience a downward fluid velocity component, thus reducing its vertical rise. As shown in Fig. (25), both the inertia-added mass force and the lift effect are of importance. The inertia term is the driving force toward the center of the vortex. Note that in the absence of gravity and lift effects, bubbles are systematically trapped at the vortex center corresponding to a stable position at $r_e = 0$.

In general, an equilibrium radius r_e can be found for any situation, but in practice bubbles are interacting with a vortex

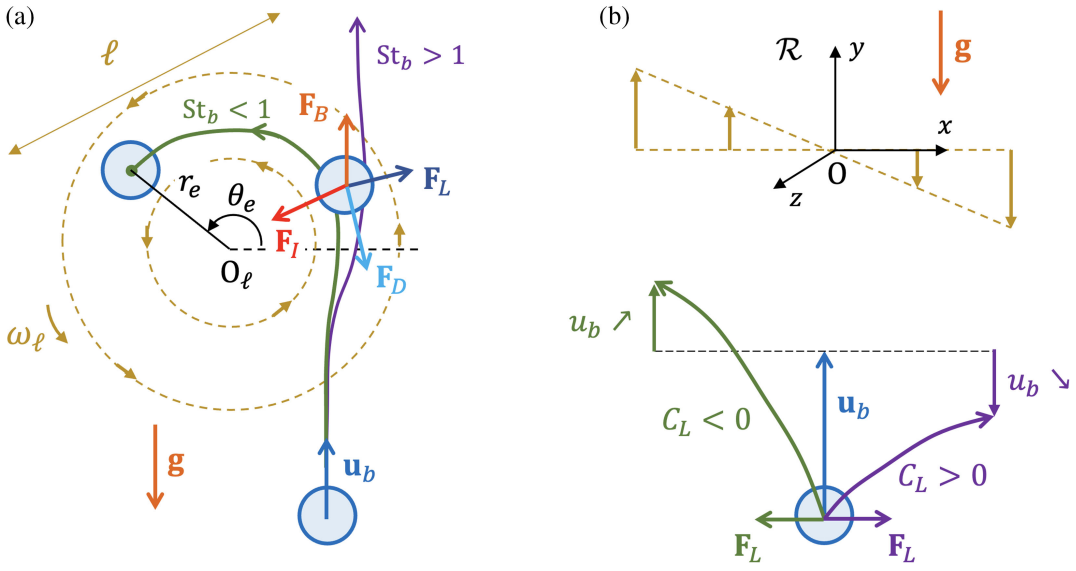

FIG. 25. Bubble interaction with turbulence. (a) Bubble interaction in a vortex: a schematic representation of a turbulence eddy. Adapted from Mathai, Lohse, and Sun, 2020. (b) Bubble rising through a velocity gradient. Adapted from Spelt and Biesheuvel, 1997.

of finite size ℓ. Their time of interaction with the vortex should be larger than both the vortex lifetime and the bubble relaxation time τ_b to make the capture possible. This provides the conditions for the vortex to capture a bubble of a certain size: $[1 + C_M - 2C_L]\omega_\ell^2 \ell/g \leq 1$ and $\omega_\ell \ell/u_\infty \leq 1$. A lifetime condition ($\tau_\ell \geq \tau_b$) can be estimated using the eddy turnover time $\tau_\ell = 1/\omega_\ell$. For eddies of characteristic size ℓ in the inertial subrange, $\omega_\ell \approx (\varepsilon/\ell^2)^{1/3}$. From these conditions, we can define a Stokes number $\mathrm{St}_\ell = \tau_b \omega_\ell$ and a Froude number $\mathrm{Fr}_\ell = \omega_\ell^2 \ell/2g$ with the following conditions for the capture of the bubble, or at least a significant interaction between the bubble and the turbulence eddy of size ℓ,

$$\mathrm{Fr}_\ell \leq \mathrm{St}_\ell \leq 1. \tag{104}$$

The second mechanism explaining the bubble motion in turbulence is related to the bubble drift when they rise through a velocity gradient, as illustrated in Fig. 25(b). Spelt and Biesheuvel (1997) introduced this idea to explain the reduction of bubble rise and the important role of the lift force in bubble interactions with turbulence. This argument was recently reused by Salibindla *et al.* (2020) to explain bubble rise velocity increase when the deformation is enough to induce lift reversal. In the scenario depicted in Fig. 25(b), consider a bubble rising at its terminal velocity $\mathbf{u}_b = u_\infty \mathbf{e}_y$ through a vertical shear flow $\mathbf{U} = -\omega x \mathbf{e}_y$. The bubble experiences a horizontal lift force $F_L = \rho \vartheta_b C_L \omega u_\infty \mathbf{e}_x$ imposed by the vorticity field $\mathbf{\Omega} = -\omega \mathbf{e}_z$. For $C_L > 0$ the bubble drifts toward the downward velocities, thus reducing its vertical rise, while when $C_L < 0$ the bubble is pushed toward the upward velocities, thus increasing its rising speed.

B. Small bubbles in turbulence

To begin, we consider small bubbles compared to the turbulent eddies, i.e., when bubble size is smaller than the Kolmogorov scale of turbulence ($d_b < \eta$). This case has received significant attention in the literature (Mathai, Lohse, and Sun, 2020). In such a situation, bubbles interact with all the scales of the flow and Eqs. (92) and (93)–(94) and (95) are usually normalized using the Kolmogorov units of length η and time τ_η. When we consider $\mathbf{g} = -g\mathbf{e}_y$, Eqs. (92) and (93)–(94) and (95) can be written as

$$\begin{aligned}\mathbf{a}_b^* &= \frac{d\mathbf{u}_b^*}{dt^*} \\ &= \frac{1}{\mathrm{St}_\eta}(\mathbf{U}^* - \mathbf{u}_b^*) + \gamma\left(\frac{\partial \mathbf{U}^*}{\partial t^*} + \mathbf{U}^* \cdot \boldsymbol{\nabla}^* \mathbf{U}^*\right)_{\mathbf{x}_b^*} \\ &\quad + \gamma'(\mathbf{U}^* - \mathbf{u}_b^*) \times \mathbf{\Omega}^* + \frac{1}{\mathrm{Fr}_\eta}\mathbf{e}_y,\end{aligned} \tag{105}$$

where asterisks denote the new dimensionless quantities. The parameters $\gamma = (1 + C_M)/C_M$ and $\gamma' = C_L/C_M$ were introduced in Eq. (96). The Stokes number is defined here as $\mathrm{St}_\eta = \tau_b/\tau_\eta = d_b^2/24\nu\tau_\eta \mathcal{K}(\mathrm{Re})$, which compares the bubble relaxation time τ_b [Eq. (97)] to the Kolmogorov time τ_η. The Stokes number defined in this manner can be used to consider Reynolds number effects because it includes the drag factor $\mathcal{K}(\mathrm{Re})$. Similarly, it can also account for bubble surface contamination (Zhang, Legendre, and Zamansky, 2021) using Eq. (31) for clean spherical bubbles or Eq. (63) for contaminated bubbles. The Froude number $\mathrm{Fr}_\eta = a_\eta/(2g)$ compares the fluid acceleration at the Kolmogorov scale $a_\eta = \eta/\tau_\eta^2$ to the Archimedean acceleration. Note that by replacing η with ℓ, we recover the Stokes number St_ℓ and the Froude number Fr_ℓ introduced in Sec. VIII.A; see Eq. (104).

From Eq. (105) it becomes clear that bubbles follow the fluid trajectories ($\mathbf{u}_b \approx \mathbf{U}$) in the limit when $\mathrm{St}_\eta \to 0$. For a nonzero Stokes number, bubbles depart from fluid streamlines and distribute nonhomogeneously due to their inertia (induced by their added mass), as illustrated in Fig. 26(a).

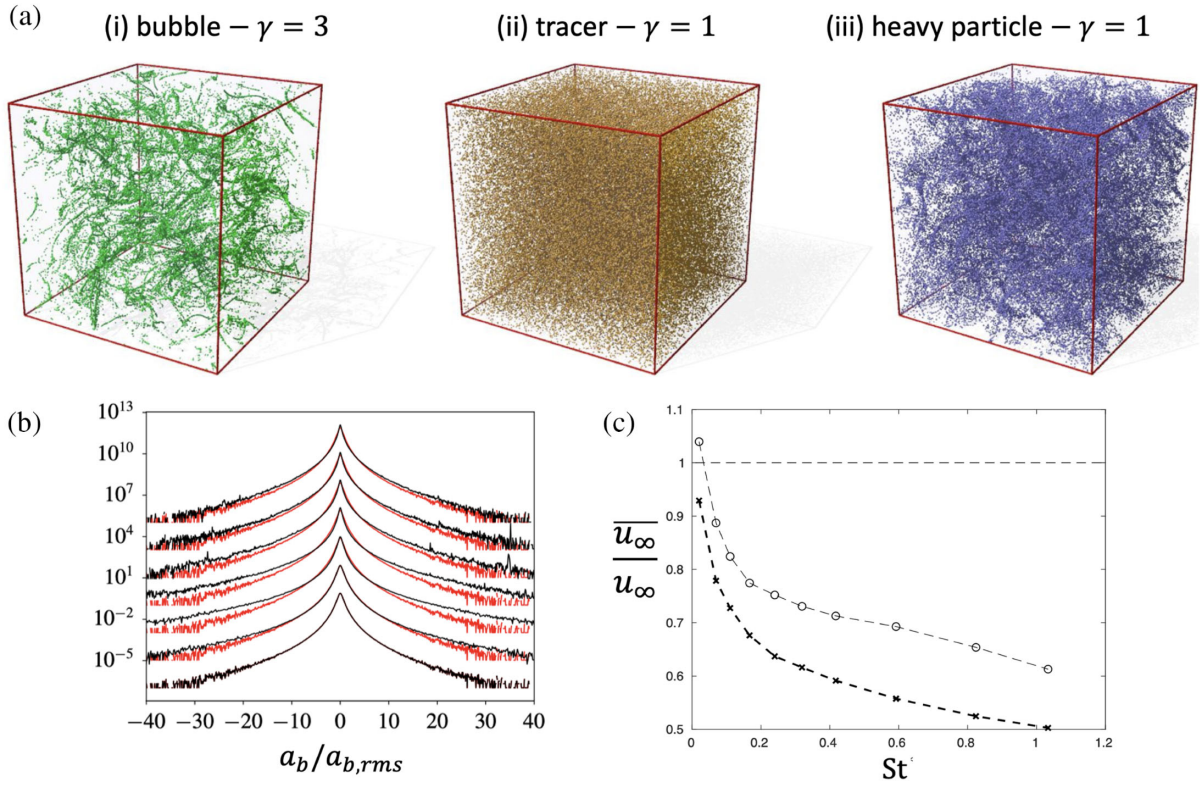

FIG. 26. Interaction of small bubbles with turbulence. (a) Snapshots of particle distributions in a turbulent flow field at $\mathrm{St} = 0.6$ for (i) $\gamma = 3$ (bubbles), (ii) $\gamma = 1$ (tracers), and (iii) $\gamma = 0$ (heavy particles). From Lohse, 2018. (b) The PDF of the bubble acceleration normalized by its root-mean-square values in black for $\mathrm{St} = 0.02$, 0.074, 0.20, 0.45, 1.01, 1.55, and 2.07 (shifted upward two decades from each other for clarity) and comparison with the PDF of the acceleration of fluid tracers in red in a homogeneous and isotropic turbulence at $\mathrm{Re}_\lambda = 100$. From Zhang, Legendre, and Zamansky, 2019. (c) The average values of the rising velocity normalized by the terminal velocity with predictions from Eq. (105) without lift force (the open circles) and with lift force (the multiplication signs). From Zhang, 2019.

Bubbles preferentially concentrate in regions of high vorticity and interact with vortices, as previously discussed. Even for low Stokes numbers, bubbles experience the effect of turbulence more intensely (Zhang, Legendre, and Zamansky, 2019). This behavior is much different from the case of heavy solid particles [$\gamma = 3\rho/(\rho + 2\rho_p) < 1$, with ρ_p the density of the particle] that are expelled from rotating regions due to their inertia (Toschi and Bodenschatz, 2009), as shown in Fig. 26(a).

In addition, from Eq. (105) we can conclude that the effect of gravity is negligible on the bubble motion as long as $\mathrm{St}_\eta/\mathrm{Fr}_\eta \ll 1$. Owing to the combined effect of inertia and buoyancy, the bubble acceleration variance $\overline{a_b^2}$ deviates from the fluid acceleration variance $\overline{a_f^2}$ as (Mathai *et al.*, 2016; Mathai, Lohse, and Sun, 2020)

$$\frac{\overline{a_b^2}}{\overline{a_f^2}} - 1 \sim \left(\frac{\mathrm{St}_\eta}{\mathrm{Fr}_\eta}\right)^2. \tag{106}$$

Thus, increasing both St_η (inertia) and $1/\mathrm{Fr}_\eta$ (buoyancy), bubbles spend less time in turbulent eddies and can rise vertically through the turbulent flow. The PDF of the bubble acceleration is shown in Fig. 26(b) for the limit $\mathrm{St}_\eta/\mathrm{Fr}_\eta \to 0$. The stretched tails in the non-Gaussian PDF indicate the occurrence of intense acceleration events that are typical of bubble behavior in turbulence. The main difference with fluid tracer acceleration is observed for intermediate Stokes numbers ($\mathrm{St}_\eta \approx 0.5$).

The role of the lift force [the second to last term on the right-hand side of Eq. (105)] has been identified as reducing the rising velocity of bubbles in turbulence (Mazzitelli, Lohse, and Toschi, 2003b). This is illustrated in Fig. 26(c), where $\overline{u_\infty}/u_\infty$ is reported as a function of St_η: the terminal velocity is significantly reduced when one considers the lift force in Eq. (105) (Zhang, 2019). Two mechanisms are usually invoked as discussed in Sec. VIII.A. First, the lift force acts to counteract the inertia with the added mass effect [the first term on the left-hand side of Eq. (105)] that drives inertial bubbles to the cores of the vortices. Second, the lift force causes the bubbles to preferentially drift toward downflow regions (with C_L positive for small spherical bubbles). The resulting reduction of the bubble rising velocity for $\beta = u'/u_\infty \ll 1$ is expressed as (Spelt and Biesheuvel, 1997; Poorte and Biesheuvel, 2002)

$$\frac{\overline{u_\infty}}{u_\infty} - 1 \sim \beta^2. \tag{107}$$

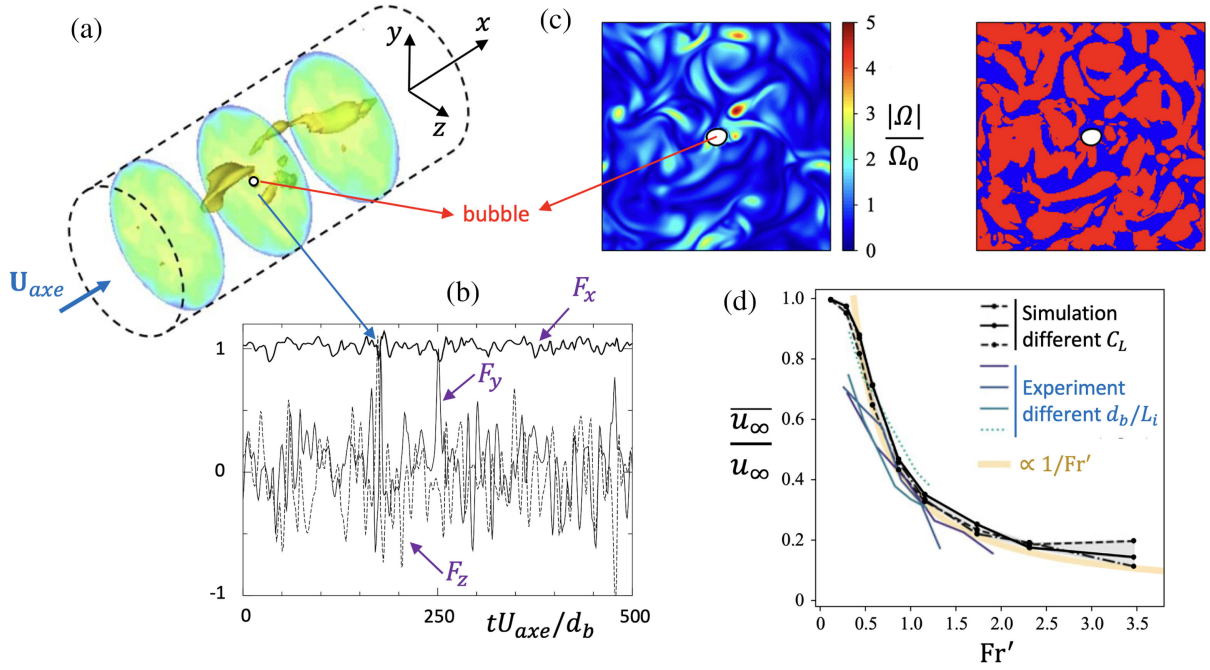

FIG. 27. Interaction of large bubbles with turbulence. (a) A spherical bubble fixed in the center of a turbulent pipe flow. The bubble Reynolds number based on the bubble diameter and the centerline velocity U_{axe} in the pipe is $\mathrm{Re} = 500$, and the turbulent pipe Reynolds number based on the pipe diameter and bulk velocity is $\mathrm{Re}_{\mathrm{pipe}} = 6000$. Turbulent eddies visualized by the isovorticity contour are responsible for the peak in the transverse force seen in (b), which shows the time evolution of the instantaneous force components normalized by the drag force on the bubble in the corresponding laminar flow (Merle, Legendre, and Magnaudet, 2005). (c) Bubble rising in a turbulent flow. From Loisy and Naso, 2017. Left panel: normalized vorticity magnitude Ω. Right panel: strain-dominated (blue) and vorticity-dominated (red) regions. (d) Evolution of the normalized rising velocity of a bubble in a turbulent field $\overline{u_\infty}/u_\infty$ as a function of the turbulent Froude number $\mathrm{Fr}' = u'/\sqrt{gd_b}$. Adapted from Ruth *et al.*, 2021.

C. Large bubbles in turbulence

The motion of bubbles with size d_b in the inertial subrange ($\eta < d_b < L_i$) has received less attention than point bubbles both in experiments (Salibindla *et al.*, 2020; Ruth *et al.*, 2021) and in direct numerical simulations where the bubble surface and all turbulence scales are resolved (Merle, Legendre, and Magnaudet, 2005; Loisy and Naso, 2017). The predictions from Eq. (105) are expected to hold for turbulent flows as long as the bubble size is much smaller than the Kolmogorov length scale. However, it is often used to describe bubble motion for $d_b > \eta$. This can be justified by considering numerical simulations conducted for spherical bubbles at large Reynolds numbers $\mathrm{Re} \gg 1$ and bubble sizes that are larger than the Kolmogorov scale but smaller than the integral length scale. Indeed, the simulations by Merle, Legendre, and Magnaudet (2005), which considered $\eta/d_b = 0.12$, $\lambda/d_b = 1.35$, and $L_i/d_b = 3.1$ for a fixed bubble in a turbulent flow ($\mathrm{Re} = 500$), showed that Eq. (105) is still able to reproduce the instantaneous force experienced by the bubble, particularly the lift force, whose magnitude can be significantly increased when the bubble is interacting with eddies of a similar size, as illustrated in Figs. 27(a) and 27(b). This supports the idea that bubbles with size in the inertial subrange ($\eta \ll d_b \ll L_i$) interact more intensely with eddies of size d_b.

Based on this argument, we determine that a relevant turbulent velocity scale for bubble dynamics is the eddy velocity scale at the bubble's size: $u_d = u_\varepsilon \sim (\varepsilon d_b)^{1/3}$ (Salibindla *et al.*, 2020). The evolution of the mean rising bubble velocity in turbulence $\overline{u_\infty}$ reported in Fig. 24 shows different behaviors, especially for large bubbles. Salibindla *et al.* (2020) reported bubble rising at a speed larger than the terminal velocity in a quiescent fluid and provided an explanation based on the lift-induced mechanism illustrated in Fig. 25. A high turbulence level is considered ($u' = 0.25$ m/s and $\beta = \mathrm{O}(1)$) and bubbles interact more intensely with eddies of the size $\ell \approx d_b$, resulting in more frequent and intense induced lift effect events, as illustrated in Fig. 27. The bubble deformation is large enough to induce lift reversal, resulting in more frequent situations where the bubble drifts toward upward velocities, as illustrated in Fig. 25(b).

Ruth *et al.* (2021) found that for u' ranging from 0.02 to 0.2 m/s, the mean rising speed $\overline{u_\infty}$ decreases as u' increases. They provided an explanation based on the mean behavior of the nonlinear drag force since they considered contaminated bubbles. This behavior differs from that of clean bubbles that, at first order, experience a linear viscous drag force. We now consider a drag force of the form $\mathbf{F}_D \propto \|\mathbf{U} - \mathbf{u}_b\|^\psi (\mathbf{U} - \mathbf{u}_b)$, where the parameter ψ can take different values, depending on the Reynolds number and the bubble surface contamination: $\psi = 0$ for a clean spherical bubble or a contaminated bubble for $\mathrm{Re} < 1$, $\psi = 0.687$ for a contaminated spherical bubble for $1 \ll \mathrm{Re} < 800$, and $\psi = 1$ for inertial drag force ($C_D = \mathrm{const}$). Considering only a balance between the drag and the buoyancy $\mathbf{F}_B$ to simplify the discussion, we have $\mathbf{F}_B + \overline{\mathbf{F}_D} \approx 0$ and $\mathbf{F}_B + \mathbf{F}_D \approx 0$ with and without

turbulence, respectively. Since $\mathbf{F}_B$ is constant for a given bubble size, we have $\overline{\mathbf{F}_D} \approx \mathbf{F}_D$. It is therefore possible to directly compare $\overline{u_\infty}$ and u_∞.

We now introduce the Reynolds decomposition for both the bubble and fluid velocities, considering for simplicity that the mean flow satisfies $\overline{\mathbf{U}} = 0$ and the mean bubble velocity is along the vertical direction $\mathbf{e}_y$ ($\overline{u_{bx}} = \overline{u_{bz}} = 0$) to express the relative velocity between the fluid and the bubble as

$$\mathbf{U} - \mathbf{u}_b = -\overline{u_\infty}\mathbf{e}_y + \mathbf{u}' - \mathbf{u}'_b. \tag{108}$$

For a linear drag force ($\psi = 0$), the magnitude of the drag force varies, with the bubble rising velocity as $\overline{F_D} \propto \overline{u_\infty}$ and $F_D \propto u_\infty$, which results in $\overline{u_\infty} \approx u_\infty$. Considering the other forces, such as the inertia and lift forces and a linear drag [$\mathbf{F}_D = 6\pi\mu d_b(\mathbf{U} - \mathbf{u}_b)$], Spelt and Biesheuvel (1997) calculated the expression of $\overline{u_\infty}$, leading to Eq. (107), which shows a decrease of the rising velocity with respect to the rise in a quiescent fluid attributed to the induced lift drift toward downward velocities, as discussed in Sec. VIII.A and illustrated in Fig. 25.

For a nonlinear relation between drag and velocity ($\psi > 0$), the mean drag will be impacted by the rms of the velocity fluctuations $\overline{|\mathbf{u}' - \mathbf{u}'_b|^2}$. If one assumes that $\psi = 1$ for simplicity, the magnitudes of drag force are then $\overline{F_D} \propto \overline{u_\infty}^2 + \overline{|\mathbf{u}' - \mathbf{u}'_b|^2}$ and $F_D \propto {u_\infty}^2$, so the relationship between the rising velocities is now $u_\infty^2 \approx \overline{u_\infty}^2 + \overline{|\mathbf{u}' - \mathbf{u}'_b|^2}$. This indicates a decrease in the rising velocity $\overline{u_\infty}$ when compared to u_∞. Based on this argument, Ruth *et al.* (2021) derived relations for $\overline{u_\infty}$ for both small and large turbulence fluctuations. In the limit of large fluctuations ($\beta \gg 1$), they found that

$$\frac{\overline{u_\infty}}{u_\infty} \sim \frac{1}{\mathrm{Fr}'}, \tag{109}$$

where $\mathrm{Fr}' = u'/\sqrt{gd_b}$ is a Froude number defined by considering the turbulence fluctuation u' and the bubble diameter. They also proposed a numerical approach based on Lagrangian tracking of point bubbles in homogeneous and isotropic turbulence by solving Eqs. (92) and (93)–(94) and (95) by imposing $\mathcal{K}(\mathrm{Re}) = C_D\mathrm{Re}/48$ and $C_D = 1$ for the unsteady drag force. Their experiments and simulations confirm the evolution of $\overline{u_\infty}/u_\infty$, with Fr' given by Eq. (109), as shown in Fig. 27(d). Their simulations, however, did not show an effect of the lift force (values of $C_L = -0.25$, 1, and 0.25 were considered) on the decrease of the rising velocity. This contradicts the conclusions of other studies for large bubbles rising in high levels of turbulence (Loisy and Naso, 2017; Salibindla *et al.*, 2020).

To summarize, a comprehensive understanding of the dynamics of large bubbles in intense turbulence remains elusive. A detailed outline of the open questions and future research directions is offered in Sec. IX.

IX. CONCLUDING REMARKS ON OPEN QUESTIONS

In this review we have discussed several key aspects of bubble motion. In any application or natural phenomenon where bubbles are present, some of which were highlighted in the Introduction, it is crucial to understand how and where they move, their speedsand shapes, and how they will interact with walls, other bubbles, or fluids with different rheologies. This task can be accomplished if we understand the physical mechanisms that influence the motion of bubbles.

By addressing the seemingly simple question as to the terminal speed of an air bubble in water, we have built the foundation of the information conveyed in this review: drag forces balance buoyancy to determine the terminal speed; viscous, inertial, and gravitational forces balance surface tension to determine the bubble shape; bubble shape influences drag; surfactants affect both drag and shape; nonuniform flows affect the bubble speed and trajectory; and walls and other bubbles affect the bubble speed, as well as fluids with different rheologies. All of these additional forces affect the bubble motion, but a good understanding and modeling of them allows us to propose a dynamic equation that is currently used to provide predictive solutions. In addition, while composing this narrative, we have identified the physical mechanisms involved and the relevant dimensionless parameters that influence the bubble dynamics; identifying such effects and numbers, their meaning and relevance, is important for reading and understanding the literature on the subject.

All of the previously listed factors that affect the bubble motion involve complexities and subtleties. Even at the bubble scale, the motion is affected by the details of the flow, deformation, and possible contamination. In most applications all of these effects appear simultaneously, making it difficult to interpret observations because each effect could not be easily disentangled from the others and because coupling among effects can arise. The challenge in conducting research in this area is to find relatively simple systems with which an idea can be methodically tested while keeping the number of parameters that affect the bubble motion small.

This review provides a solid foundation for understanding bubble dynamics. It surveys the classical results from the literature while incorporating explanations of physical phenomena based on recent investigations. We feel that the subject of bubble dynamics has reached a good level of maturity. We believe that many of the challenges in bubble-based applications and natural phenomena can be addressed by considering some of the physical descriptions discussed in this review. We note, however, that most of the current understanding is still limited to relatively simple flow configurations and, most importantly, to Newtonian liquids. Writing this review has helped us to identify relevant areas that need attention: bubble dynamics in turbulent flows, the effect of non-Newtonian liquids, and the effect of surface contamination in the presence of electrolytes. Many modern applications, especially those for biological flows, will imply bubbles moving in turbulent fluids with a non-Newtonian nature and/or salt-rich environments for which the understanding of bubble dynamics is in its infancy.

For bubbles moving in turbulent flows, we conclude that understanding how large bubbles (larger than the Kolmogorov scale but smaller than the integral scale) respond to intense turbulent fields remains an open question. In particular, future works will have to clarify the interaction mechanism between

turbulence and bubble deformation and contamination. A full picture of their respective impact of these factors, in particular, on the bubble rising velocity, is needed. Under what conditions can one expect the mean bubble rise velocity $\overline{u_\infty}$ in turbulence to be larger than the bubble rise velocity in a stagnant fluid u_∞? Addressing this question will require the coupled effects of bubble deformation and surface contamination to be considered. As discussed, contaminants influence bubble deformation and deformation affects surfactant coverage. This mutual influence can alter the interfacial vorticity, potentially modifying how the bubble is driven by drag and lift forces within the turbulent field. This effect, and its response to turbulence, could be significant in understanding aggregation and dispersion in bubbly flows.

The understanding of bubble dynamics in non-Newtonian fluids is much less mature than that currently available for Newtonian fluids. Although there are numerous experiments reported in the literature, many of which are not recent, our current understanding remains fragmented and needs further consolidation through focused research. With computational tools now highly advanced, it is time to combine numerical and experimental investigations to clarify key aspects of bubble dynamics. To begin, it would be highly desirable to obtain a version of the Clift-Grace-Weber diagram [see Fig. 4(b) (Clift, Grace, and Weber, 1978)] for the case of non-Newtonian fluids. Accomplishing this task would require experiments or simulations that gradually vary the elasticity of the fluid while keeping the viscosity constant. This approach would isolate the effects of elasticity, enabling a precise assessment of its influence on bubble shape and terminal velocity. Then the effects of shear-dependent viscosity could be investigated as an additional complexity to the problem. A path similar to that followed for Newtonian fluids should be followed to gain an understanding of the nature of hydrodynamic interactions in non-Newtonian fluids. Zenit and Feng (2018) summarized the main issues in this area. There are recent investigations that aim to understand single bubble behavior (Fraggedakis *et al.*, 2016; Bothe *et al.*, 2022) and pair interactions (Ravisankar *et al.*, 2022; Kordalis *et al.*, 2023) in non-Newtonian fluids that could serve as guides for future research in the area. The importance of the effect of contaminants on the motion of bubbles in non-Newtonian media has been long recognized (Astarita and Apuzzo, 1965), but a clear picture of the physical understanding is lacking. To our knowledge, studies of bubbles in turbulent fields in non-Newtonian fields do not exist. This area has relevance in the context of bioreactors and drag reduction.

Finally, we have recognized that the effect of electrolytes in several aspects of gas bubble dynamics remains either poorly understood or unresolved. Electrolytes are substances, soluble in water, that can have natural positive or negative electrical charges. These charges can have a significant effect in the production of hydrogen via electrolysis: the bubble nucleation, coalescence, and detachment from an electrode surface, as shown in Fig. 1(c), impact the generated bubble swarm. Since hydrogen is our best option to replace fossil fuels, it is extremely important to study how bubble dynamics can help improve the efficiency to produce hydrogen in a green and sustainable way using this method (Angulo *et al.*, 2020). All additives to air-water systems, such as surfactants, alcohols, and other substances including electrolytes, are usually classified as contaminants. The effects of contaminants were discussed in this review, but certainly not extensively. When used in small quantities, electrolytes inhibit bubble coalescence (Lessard and Zieminski, 1971; Zenit, Koch, and Sangani, 2001; Orvalho, Ruzicka, and Drahos, 2009; Orvalho, Stanovsky, and Ruzicka, 2021) due to short-range repulsion forces induced by the electrical charges. However, a clear understanding of the effect of electrolytes at large concentrations, such as those as encountered in electrolyzers, is still needed. Recent experiments of air bubbles in low-concentration electrolyte solutions (Quinn *et al.*, 2014; Hessenkemper, Ziegenhein, and Lucas, 2020) reported that the relationship between rise velocity and bubble size is not significantly affected by the presence of electrolytes, regardless of the solute type. However, they found that electrolyte can have a significant effect on how surfactant molecules move and accumulate on the bubble surface, possibly leading to changes in shape, drag, and interactions. For the specific case of hydrogen bubbles, Mandalahalli *et al.* (2023) found that the rise characteristics (velocity and shape) at different concentrations of a mixture electrolytes can be explained by their effect on the liquid properties (density, viscosity, and surface tension). Owing to the limited amount of information, it is not yet possible to determine whether these findings can be applied generally to other gas-liquid combinations. Other complexities that need to be addressed for the case of hydrogen bubbles is their potential for reactivity, which makes them susceptible to react to contaminants suspended in water; hydrogen is also known to be consumed by bacteria in natural environments (Barz *et al.*, 2010; Lappan *et al.*, 2023). Future investigations will need to account for these additional complexities, which have not been discussed in this review.

With the many challenges in bubble dynamics described here, we remain excited about the discoveries that lie ahead. We hope that this review will serve as a guide and inspiration for future researchers in the field of bubble dynamics to pursue some of these studies in the years to come.

ACKNOWLEDGMENTS

We thank our students and colleagues for many helpful discussions and suggestions during the preparation of this manuscript. We are grateful to M. Ravisankar for conducting some additional experiments to obtain bubble shape images shown in the review.

REFERENCES

Acrivos, A., and T. Taylor, 1962, Phys. Fluids **5**, 387.
Adoua, R., D. Legendre, and J. Magnaudet, 2009, J. Fluid Mech. **628**, 23.
Angulo, A., P. van der Linde, H. Gardeniers, M. Modestino, and D. Fernández Rivas, 2020, Joule **4**, 555.
Aoyama, S., K. Hayashi, S. Hosokawa, D. Lucas, and A. Tomiyama, 2017, Int. J. Multiphase Flow **96**, 113.
Astarita, G., and G. Apuzzo, 1965, AIChE J. **11**, 815.
Atasi, O., D. Legendre, B. Haut, R. Zenit, and B. Scheid, 2020, Langmuir **36**, 7749.

Atasi, O., M. Ravisankar, D. Legendre, and R. Zenit, 2023, Phys. Rev. Fluids **8**, 053601.
Auton, T., 1987, J. Fluid Mech. **183**, 199.
Auton, T., J. C. R. Hunt, and M. Prud'Homme, 1988, J. Fluid Mech. **197**, 241.
Aybers, N., and A. Tapucu, 1969, Wärme- Stoffübertrag **2**, 118.
Barbosa, C., D. Legendre, and R. Zenit, 2016, Phys. Rev. Fluids **1**, 032201.
Barbosa, C., D. Legendre, and R. Zenit, 2019, Phys. Rev. Fluids **4**, 043602.
Barz, M., *et al.*, 2010, PLoS One **5**, e13846.
Batchelor, G. K., 1967, *An Introduction to Fluid Dynamics* (Cambridge University Press, Cambridge, England).
Batchelor, G. K., 1987, J. Fluid Mech. **184**, 399.
Bird, R. B., R. C. Armstrong, and O. Hassager, 1987, *Dynamics of Polymeric Liquids, Vol. 1: Fluid Mechanics* (Wiley, New York).
Blanco, A., and J. Magnaudet, 1995, Phys. Fluids **7**, 1265.
Bonnefis, P., D. Fabre, and J. Magnaudet, 2023, Proc. Natl. Acad. Sci. U.S.A. **120**, e2300897120.
Bothe, D., M. Niethammer, C. Pilz, and G. Brenn, 2022, J. Non-Newtonian Fluid Mech. **302**, 104748.
Brennen, C. E., 2014, *Cavitation and Bubble Dynamics* (Cambridge University Press, Cambridge, England).
Candelier, F., R. Angilella, and M. Souhar, 2005, J. Fluid Mech. **545**, 113.
Cano-Lozano, J. C., C. Martínez-Bazán, J. Magnaudet, and J. Tchoufag, 2016, Phys. Rev. Fluids **1**, 053604.
Cano-Lozano, J. C., J. Tchoufag, J. Magnaudet, and C. Martínez-Bazán, 2016, Phys. Fluids **28**, 014102.
Carreau, P. J., 1972, Trans. Soc. Rheol. **16**, 99.
Ceccio, S. L., 2010, Annu. Rev. Fluid Mech. **42**, 183.
Chandran, P., S. Bakshi, and D. Chatterjee, 2015, Chem. Eng. Sci. **138**, 99.
Chhabra, R. P., 2006, *Bubbles, Drops, and Particles in Non-Newtonian Fluids* (CRC Press, Boca Raton).
Chouippe, A., E. Climent, D. Legendre, and C. Gabillet, 2014, Phys. Fluids **26**, 043304.
Clayton, B. R., and B. S. Massey, 1967, J. Sci. Instrum. **44**, 2.
Clift, R., J. R. Grace, and M. E. Weber, 1978, *Bubbles, Drops and Particules* (Academic Press, New York).
Colin, C., J. Fabre, and A. Kamp, 2012, J. Fluid Mech. **711**, 469.
Cross, M. M., 1979, Rheol. Acta **18**, 609.
Cuenot, B., J. Magnaudet, and B. Spennato, 1997, J. Fluid Mech. **339**, 25.
Dandy, D., and L. Leal, 1986, Phys. Fluids **29**, 1360.
Davenport, J., R. N. Hughes, M. Shorten, and P. S. Larsen, 2011, Mar. Ecol. Prog. Ser. **430**, 171.
Davies, R. M., and G. I. Taylor, 1950, Proc. R. Soc. A **200**, 375.
Demir-Yilmaz, I., M. S. Ftouhi, S. Balayssac, P. Guiraud, C. Coudret, and C. Formosa-Dague, 2023, Chem. Eng. J. **452**, 139349.
de Vries, A. W. G., A. Biesheuvel, and L. van Wijngaarden, 2002, Int. J. Multiphase Flow **28**, 1823.
Duhar, G., and C. Colin, 2006, Phys. Fluids **18**, 077101.
Duineveld, P. C., 1995, J. Fluid Mech. **292**, 325.
Epstein, P. S., and M. S. Plesset, 1950, J. Chem. Phys. **18**, 1505.
Federle, M. E., A. Das, V. Mathai, and R. Zenit, 2024, Int. J. Multiphase Flow **171**, 104682.
Figueroa-Espinoza, B., D. Legendre, and R. Zenit, 2008, J. Fluid Mech. **616**, 419.
Figueroa-Espinoza, B., B. Mena, A. Aguilar-Corona, and R. Zenit, 2018, Int. J. Multiphase Flow **106**, 138.
Fraggedakis, D., M. Pavlidis, Y. Dimakopoulos, and J. Tsamopoulos, 2016, J. Fluid Mech. **789**, 310.
Fritz, W., 1935, Phys. Z. **36**, 379.
Fukuta, M., S. Takagi, and Y. Matsumoto, 2008, Phys. Fluids **20**, 040704.
Garbin, V., B. Dollet, M. Overvelde, D. Cojoc, E. Di Fabrizio, L. van Wijngaarden, A. Prosperetti, N. de Jong, L. Lohse, and M. Versluis, 2009, Phys. Fluids **21**, 092003.
García-Magariño, A., P. Lopez-Gavilan, S. Sor, and F. Terroba, 2023, J. Mar. Sci. Eng. **11**, 1315.
Gatignol, R., 1983, J. Mec. Theor. Appl. **1**, 143, http://pascal-francis.inist.fr/vibad/index.php?action=getRecordDetail&idt=PASCAL83X0344635.
Giribabu, K., and P. Ghosh, 2007, Chem. Eng. Sci. **62**, 3057.
Gorodtsov, V., 1975, J. Appl. Mech. Tech. Phys. **16**, 865.
Guthrie, R. I. L., and A. V. Bradshaw, 1969, Chem. Eng. Sci. **24**, 913.
Haberman, W. L., and R. K. Morton, 1956, Trans. Am. Soc. Civ. Eng. **121**, 227.
Hadamard, J. S., 1911, C. R. Acad. Sci. Paris Ser. IV **152**, 1735.
Hallez, Y., and D. Legendre, 2011, J. Fluid Mech. **673**, 406.
Harper, J. F., 1970, J. Fluid Mech. **41**, 751.
Hartunian, R. A., and W. R. Sears, 1957, J. Fluid Mech. **3**, 27.
Hassager, O., 1979, Nature (London) **279**, 402.
Hayashi, K., H. Hessenkemper, D. Lucas, D. Legendre, and A. Tomiyama, 2021, Int. J. Multiphase Flow **142**, 103653.
Hayashi, K., D. Legendre, and A. Tomiyama, 2020, Int. J. Multiphase Flow **129**, 103350.
Henzler, H. J., and D. J. Kauling, 1993, Bioprocess Eng. **9**, 61.
Herrera-Velarde, J. R., R. Zenit, D. Chehata, and B. Mena, 2003, J. Non-Newtonian Fluid Mech. **111**, 199.
Hessenkemper, H., T. Ziegenhein, and D. Lucas, 2020, Chem. Eng. J. **386**, 121589.
Hessenkemper, H., T. Ziegenhein, D. Lucas, and A. Tomiyama, 2021, Int. J. Multiphase Flow **145**, 103833.
Hidman, N., H. Ström, S. Sasic, and G. Sardina, 2022, J. Fluid Mech. **952**, A34.
Hinze, J., 1955, AIChE J. **1**, 289.
Homann, H., and J. Bec, 2010, J. Fluid Mech. **651**, 81.
Hooshanginejad, A., T. Sheppard, P. Xu, J. Manyalla, J. Jaicks, E. Esmaili, and S. Jung, 2023, Phys. Rev. Fluids **8**, 043602.
Huang, Z., D. Legendre, and P. Guiraud, 2011, Chem. Eng. Sci. **66**, 982.
Joseph, D. D., 2003, J. Fluid Mech. **488**, 213.
Joseph, G. G., R. Zenit, M. L. Hunt, and A. M. Rosenwinkel, 2001, J. Fluid Mech. **433**, 329.
Kantarci, N., F. Borak, and O. Ulgen, 2005, Process Biochem. **40**, 2263.
Kawabuchi, M., C. Kawakita, S. Mizokami, S. Higasa, Y. Kodan, and S. Takano, 2011, Tech. Rev. Mitsubishi Heavy Ind. **48**, 53, http://www.rexresearch.com/mals/e481053.pdf.
Kong, G., H. Mirsandi, K. A. Buist, E. Peters, M. Baltussen, and J. Kuipers, 2019, Exp. Fluids **60**, 1.
Kordalis, A., D. Pema, S. Androulakis, Y. Dimakopoulos, and J. Tsamopoulos, 2023, Phys. Rev. Fluids **8**, 083301.
Kulkarni, A. A., and J. B. Joshi, 2005, Ind. Eng. Chem. Res. **44**, 5873.
Kusuno, H., and T. Sanada, 2021, Int. J. Multiphase Flow **139**, 103639.
Lalanne, B., O. Masbernat, and F. Risso, 2019, AIChE J. **65**, 347.
Lappan, R., *et al.*, 2023, Nat. Microbiol. **8**, 581.
Lebon, M., J. Sebilleau, and C. Colin, 2018, Phys. Rev. Fluids **3**, 073602.
Lecher, A. L., P.-C. Chuang, M. Singleton, and A. Paytan, 2017, J. Geophys. Res. Biogeosci. **122**, 753.
Legendre, D., 2007, Phys. Fluids **19**, 018102.

Legendre, D., 2022, Phys. Rev. Fluids **7**, 093601.
Legendre, D., and J. Magnaudet, 1997, Phys. Fluids **9**, 3572.
Legendre, D., and J. Magnaudet, 1998, J. Fluid Mech. **368**, 81.
Legendre, D., J. Magnaudet, and G. Mougin, 2003, J. Fluid Mech. **497**, 133.
Legendre, D., R. Zenit, C. Daniel, and P. Guiraud, 2006, Chem. Eng. Sci. **61**, 3543.
Legendre, D., R. Zenit, and J. R. Velez-Cordero, 2012, Phys. Fluids **24**, 043303.
Legendre, D., and R. Zevenhoven, 2017, Chem. Eng. Sci. **158**, 552.
Leifer, I., and R. K. Patro, 2002, Cont. Shelf Res. **22**, 2409.
Lessard, R. R., and S. A. Zieminski, 1971, Ind. Eng. Chem. Fundam. **10**, 260.
Levich, V. G., 1962, *Physicochemical Hydrodynamics* (Prentice-Hall, Englewood Cliffs, NJ).
Li, W., and N. R. Gupta, 2019, Ind. Eng. Chem. Res. **58**, 7640.
Lighthill, J., 1956, J. Fluid Mech. **1**, 31.
Lodge, A. S., J. D. Schieber, and R. B. Bird, 1988, J. Chem. Phys. **88**, 4001.
Lohse, D., 2018, Phys. Rev. Fluids **3**, 110504.
Loisy, A., and A. Naso, 2017, Phys. Rev. Fluids **2**, 014606.
Lunde, K., 1997, in *Proceedings of the ASME Fluids Engineering Division Summer Meeting, Vancouver, British Columbia, 1997* (American Society of Mechanical Engineers, New York), p. 3530.
Ma, T., H. Hessenkemper, D. Lucas, and A. D. Bragg, 2023, J. Fluid Mech. **973**, A15.
Madavan, N., S. Deutsch, and C. Merkle, 1985, J. Fluid Mech. **156**, 237.
Magnaudet, J., and I. Eames, 2000, Annu. Rev. Fluid Mech. **32**, 659.
Magnaudet, J., and D. Legendre, 1998, Phys. Fluids **10**, 550.
Magnaudet, J., M. Rivero, and J. Fabre, 1995, J. Fluid Mech. **284**, 97.
Magnaudet, J., S. Takagi, and D. Legendre, 2003, J. Fluid Mech. **476**, 115.
Mandalahalli, M. M., J. Lif, R. F. Mudde, and L. M. Portela, 2023, Chem. Eng. Sci. **270**, 118276.
Mathai, V., E. Calzavarini, J. Brons, C. Sun, and D. Lohse, 2016, Phys. Rev. Lett. **117**, 024501.
Mathai, V., D. Lohse, and C. Sun, 2020, Annu. Rev. Condens. Matter Phys. **11**, 529.
Maxey, M. R., and J. J. Riley, 1983, Phys. Fluids **26**, 883.
Maxworthy, T., C. Gnann, M. Kurten, and F. Durst, 1996, J. Fluid Mech. **321**, 421.
Mazzitelli, I. M., D. Lohse, and F. Toschi, 2003a, Phys. Fluids **15**, 5.
Mazzitelli, I. M., D. Lohse, and F. Toschi, 2003b, J. Fluid Mech. **488**, 283.
McLaughlin, J. B., 1991, J. Fluid Mech. **224**, 261.
Mei, R., and R. J. Adrian, 1992, J. Fluid Mech. **237**, 133.
Mei, R., and J. F. Klausner, 1992, Phys. Fluids A **4**, 63.
Merle, A., D. Legendre, and J. Magnaudet, 2005, J. Fluid Mech. **532**, 53.
Moore, D. W., 1963, J. Fluid Mech. **16**, 161.
Moore, D. W., 1965, J. Fluid Mech. **23**, 749.
Moreno Soto, A., O. R. Enríquez, A. Prosperetti, D. Lohse, and D. van der Meer, 2019, J. Fluid Mech. **871**, 332.
Mougin, G., and J. Magnaudet, 2001, Phys. Rev. Lett. **88**, 014502.
Mougin, G., and J. Magnaudet, 2006, J. Fluid Mech. **567**, 185.
Mougin, G., and J. Magnaudet, 2007, J. Fluid Mech. **572**, 311.
Muniz, M., and M. Sommerfeld, 2020, Int. J. Multiphase Flow **128**, 103256.
Murai, Y., 2014, Exp. Fluids **55**, 1773.
Ni, R., 2024, Annu. Rev. Fluid Mech. **56**, 319.
Oguz, H. N., and A. Prosperetti, 1993, J. Fluid Mech. **257**, 111.
Oldroyd, J. G., 1950, Proc. R. Soc. A **200**, 523.
Olgac, U., and M. Muradoglu, 2013, Int. J. Multiphase Flow **48**, 58.
Orvalho, S., M. C. Ruzicka, and J. Drahos, 2009, Ind. Eng. Chem. Res. **48**, 8237.
Orvalho, S., P. Stanovsky, and M. C. Ruzicka, 2021, Chem. Eng. J. **406**, 125926.
Palacios-Morales, C., C. Barbosa, F. Solorio, and R. Zenit, 2015, Phys. Fluids **27**, 051703.
Pang, M., and Z. Zhang, 2018, Ocean Eng. **162**, 80.
Pesci, C., A. Weiner, H. Marschall, and D. Bothe, 2018, J. Fluid Mech. **856**, 709.
Pilz, C., and G. Brenn, 2007, J. Non-Newtonian Fluid Mech. **145**, 124.
Poorte, R. E. G., and A. Biesheuvel, 2002, J. Fluid Mech. **461**, 127.
Prakash, V., Y. Tagawa, E. Calzavarini, J. Mercado, F. Toschi, D. Lohse, and C. Sun, 2012, New J. Phys. **14**, 105017.
Prosperetti, A., 2004, Phys. Fluids **16**, 1852.
Prosperetti, A., 2017, Annu. Rev. Fluid Mech. **49**, 221.
Quinn, J., M. Maldonado, C. Gomez, and J. Finch, 2014, Miner. Eng. **55**, 5.
Rage, G., O. Atasi, M. M. Wilhelmus, J. F. Hernández-Sánchez, B. Haut, B. Scheid, D. Legendre, and R. Zenit, 2020, Sci. Rep. **10**, 11014.
Rastello, M., J.-L. Marié, and M. Lance, 2011, J. Fluid Mech. **682**, 434.
Ravelet, F., C. Colin, and F. Risso, 2011, Phys. Fluids **23**, 103301.
Ravisankar, M., 2021, master's thesis (Brown University).
Ravisankar, M., A. Garcidueñas Correa, Y. Su, and R. Zenit, 2022, J. Non-Newtonian Fluid Mech. **309**, 104912.
Risso, F., 2000, Multiphase Sci. Technol. **12**, 1.
Risso, F., 2018, Annu. Rev. Fluid Mech. **50**, 25.
Risso, F., and J. Fabre, 1998, J. Fluid Mech. **372**, 323.
Riviére, A., K. Abahri, and S. Perrard, 2024, arXiv:2407.16545.
Riviére, A., and S. Perrard, 2024, arXiv:2403.08684.
Roberts, J., 1981, *The Codex Hammer of Leonardo da Vinci* (Giunti Barbera, Florence).
Ruth, D., A. K. Aiyer, A. Riviére, S. Perrard, and L. Deike, 2022, J. Fluid Mech. **951**, A32.
Ruth, D., M. Mostert, S. Perrard, and L. Deike, 2019, Proc. Natl. Acad. Sci. U.S.A. **116**, 25412.
Ruth, D. J., M. Vernet, S. Perrard, and L. Deike, 2021, J. Fluid Mech. **924**, A2.
Rybczynski, W., 1911, Bull. Int. Acad. Sci. Cracovie **40**, 1735.
Saffman, P. G., 1956, J. Fluid Mech. **1**, 249.
Saffman, P. G., 1965, J. Fluid Mech. **22**, 385.
Salibindla, A., A. Masuk, S. Tan, and R. Ni, 2020, J. Fluid Mech. **894**, A20.
Sanada, T., A. Sato, M. Shirota, and M. Watanabe, 2009, Chem. Eng. Sci. **64**, 2659.
Sanada, T., M. Watanabe, and T. Fukano, 2005, Chem. Eng. Sci. **60**, 5372.
Saththasivam, J., K. Loganathan, and S. Sarp, 2016, Chemosphere **144**, 671.
Schiller, L., and A. Z. Naumann, 1933, VDI Z. **77**, 318.
Schlüter, M., S. Herres-Pawlis, U. Nieken, U. Tuttlies, and D. Bothe, 2021, Annu. Rev. Chem. Biomol. Eng. **12**, 625.
Sevik, M., and S. H. Park, 1973, J. Fluids Eng. **95**, 53.
Shi, P., R. Rzehak, D. Lucas, and J. Magnaudet, 2020, Phys. Rev. Fluids **5**, 073601.
Simmons, J. A., J. E. Sprittles, and Y. D. Shikhmurzaev, 2015, Eur. J. Mech. B **53**, 24.
Smith, C., D. Sabatino, T. Praisner, and C. Seal, 2012, in *Flow Visualization: Techniques and Examples*, edited by A. J. Smits (World Scientific, Singapore), pp. 3–21.

Song, W., C. Wang, L. Wei, L. Lu, and H. Xu, 2018, Mod. Phys. Lett. B **32**, 1850206.
Soto, E., C. Goujon, R. Zenit, and O. Manero, 2006, Phys. Fluids **18**, 121510.
Soto-Castruita, E., 2008, Ph.D. thesis (Universidad Nacional Autonama de Mexico).
Spelt, P. D. M., and A. Biesheuvel, 1997, J. Fluid Mech. **336**, 221.
Stokes, G. G., 1851, Trans. Cambridge Philos. Soc. **9**, 8.
Stone, H. A., 1990, Phys. Fluids A **2**, 111.
Sugiyama, K., E. Calzavarini, and D. Lohse, 2008, J. Fluid Mech. **608**, 21.
Tagawa, Y., S. Takagi, and Y. Matsumoto, 2014, J. Fluid Mech. **738**, 124.
Takagi, S., and Y. Matsumoto, 2011, Annu. Rev. Fluid Mech. **43**, 615.
Takagi, S., T. Ogasawara, M. Fukuta, and Y. Matsumoto, 2009, Fluid Dyn. Res. **41**, 065003.
Takagi, S., T. Ogasawara, and Y. Matsumoto, 2008, Phil. Trans. R. Soc. A **366**, 2117.
Takemura, F., and J. Magnaudet, 2003, J. Fluid Mech. **495**, 235.
Takemura, F., J. Magnaudet, and P. Dimitrakopoulos, 2009, J. Fluid Mech. **634**, 463.
Tanaka, T., Y. Oishi, H. J. Park, Y. Tasaka, Y. Murai, and C. Kawakita, 2021, Ocean Eng. **239**, 109909.
Tanner, R. I., 1970, J. Polym. Sci., Part A **8**, 2067.
Taylor, T., and A. Acrivos, 1964, J. Fluid Mech. **18**, 466.
Tchoufag, J., J. Magnaudet, and D. Fabre, 2013, Phys. Fluids **25**, 054108.
Tchoufag, J., J. Magnaudet, and D. Fabre, 2014, J. Fluid Mech. **751**, R4.
Teixidó, N., M. C. Gambi, V. Parravacini, K. Kroeker, F. Micheli, S. Villéger, and E. Ballesteros, 2018, Nat. Commun. **9**, 5149.
Thomas, N., T. Auton, K. Sene, and J. Hunt, 1983, in *Proceedings of the International Conference on Physical Modelling of Multi-Phase Flow, Coventry, England, 1983* (BHRA Fluid Engineering, Cranfield), pp. 169–184.
Toegel, R., S. Luther, and D. Lohse, 2006, Phys. Rev. Lett. **96**, 114301.
Tomiyama, A., H. Tamai, I. Žun, and S. Hosokawa, 2002, Chem. Eng. Sci. **57**, 1849.
Toschi, F., and E. Bodenschatz, 2009, Annu. Rev. Fluid Mech. **41**, 375.
Tripathi, M. K., K. C. Sahu, and R. Govindarajan, 2015, Nat. Commun. **6**, 6268.
van Nierop, E. A., S. Luther, J. J. Bluemink, J. Magnaudet, A. Prosperetti, and D. Lohse, 2007, J. Fluid Mech. **571**, 439.
van Wijngaarden, L., 1976, J. Fluid Mech. **77**, 27.
Vejrazka, J., M. Zednikova, and P. Stanovsky, 2018, AIChE J. **64**, 740.
Vélez-Cordero, J. R., D. Sámano, P. Yue, J. J. Feng, and R. Zenit, 2011, J. Non-Newtonian Fluid Mech. **166**, 118.
Vélez-Cordero, J. R., D. Sámano, and R. Zenit, 2012, J. Non-Newtonian Fluid Mech. **175–176**, 1.
Vélez-Cordero, J. R., and R. Zenit, 2011, J. Non-Newtonian Fluid Mech. **166**, 32.
Veron, F., 2015, Annu. Rev. Fluid Mech. **47**, 507.
Verschoof, R. A., R. C. van der Veen, C. Sun, and D. Lohse, 2016, Phys. Rev. Lett. **117**, 104502.
Wang, B., S. A. Socolofsky, J. A. Breier, and J. S. Seewald, 2016, J. Geophys. Res. Oceans **121**, 2203.
Wang, L., and M. Maxey, 1993, Appl. Sci. Res. **51**, 291.
Xu, J., M. Maxey, and G. Karniadakis, 2002, J. Fluid Mech. **468**, 271.
Yang, S.-M., and L. G. Leal, 1991, Phys. Fluids **3**, 1822.
Zenit, R., and J. J. Feng, 2018, Annu. Rev. Fluid Mech. **50**, 505.
Zenit, R., D. L. Koch, and A. S. Sangani, 2001, J. Fluid Mech. **429**, 307.
Zenit, R., and D. Legendre, 2009, Phys. Fluids **21**, 083306.
Zenit, R., and J. Magnaudet, 2009, Int. J. Multiphase Flow **35**, 195.
Zenit, R., and J. Rodríguez-Rodríguez, 2018, Phys. Today **71**, No. 11, 44.
Zhang, J., M. Hi, and J. Magnaudet, 2021, J. Fluid Mech. **920**, A16.
Zhang, J., M. Hi, and J. Magnaudet, 2022, J. Fluid Mech. **943**, A10.
Zhang, L., Z.-S. Yang, and C. Mao, 2010, J. Non-Newtonian Fluid Mech. **165**, 555.
Zhang, Y., J. B. McLaughlin, and J. A. Finch, 2001, Chem. Eng. Sci. **56**, 6605.
Zhang, Z., 2019, Ph.D. thesis [Toulouse INP (National Polytechnic Institute of Toulouse)].
Zhang, Z., D. Legendre, and R. Zamansky, 2019, J. Fluid Mech. **879**, 554.
Zhang, Z., D. Legendre, and R. Zamansky, 2021, J. Fluid Mech. **921**, A4.
Žun, I., 1980, Int. J. Multiphase Flow **6**, 583.